ALMA MATER STUDIORUM – UNIVERSITA' DI BOLOGNA
Department of Civil, Chemical, Environmental, and Materials Engineering
Two-Year Master's Degree in Civil Engineering – Structural Curriculum – LM23
Final dissertation in Structural Safety

Towards a design approach for Wire-and-Arc Additively Manufactured stainless-steel elements

Student:
Silvia Furlanis

Supervisor:
Prof. Dr. Tomaso Trombetti
Co-supervisors:
Eng. Dr. Vittoria Laghi
Prof. Dr. Milan Veljkovic

Academic Year 2020/2021

To my parents,

my tireless cheerleaders
ever since day one

Abstract

Additive Manufacturing has become more and more relevant in the recent years in the construction industry, while still being at its initial stage. In particular, Wire-and-Arc Additively Manufactured (WAAM) stainless-steel elements have yet to be properly analyzed from a structural response point-of-view, though many experimental campaigns and studies are being carried out to this day.

This study is focused on the analysis of the results of tests conducted on WAAM-produced 308LSi stainless-steel specimens, in order to characterize the mechanical and geometrical properties of the printed material and calibrate design values by means of Annex D of Eurocode 0, which outlines procedures to carry out the safety analysis of the resistance function, hence the definition of partial safety factors, aiming at a semi-probabilistic design approach.

Moreover, by means of available Digital Twins of produced and tested specimens, different approaches are followed for the understanding of the influence of geometrical irregularities on the behavior of the material, in terms of stress-strain relationship. Regarding this, a series of calibrations are performed in order to quantify said influence, with a particular focus on the elastic behavior.

Acknowledgments

Firstly, I would like to thank my supervisor, prof. Tomaso Trombetti, for giving me the opportunity to undertake this project and to collaborate in person with the University of Delft for a few months, which helped me greatly towards the successful completion of my work.
I would like to also thank my co-supervisor in Bologna, Eng. Dr. Vittoria Laghi, who has truly been a constant support, guidance and motivation throughout the entire project; and my supervisor in Delft, Prof. Dr. Milan Veljkovic, who helped me broaden my knowledge and my views, and allowed me to meet and work with some of his brilliant associates.

A very special thank you goes to my family, who have always been an endless source of love, support and inspiration throughout everything I have ever done and accomplished. You have trust in me and in what I can do, even when I feel lost; you push me, when I think I cannot possibly get where I want; you comfort me, when I need it the most. And for this and a lot more, I am so thankful for you and I could not have asked for anyone better to have by my side.
To my friends, who have been there for me and supported me all the way to this great achievement: I treasure and am grateful for you, and I cannot wait to share more milestones in my life with you.

And, in the wise words of Snoop Dogg: “Last but not least, I want to thank me. I want to thank me for believing in me. I want to thank me for doing all this hard work. I want to thank me for having no days off. I want to thank me for never quitting”.

Contents

List of Figures

List of Tables

1. Introduction

1.1 Text organization

Chapter 1 concerns a general overview on the text (section 1.1) and the objectives of the project (section 1.2).

The text is then divided into two parts: Part A, concerning the statistical analysis of experimental data and the calibration of design values by means of the procedures described in Annex D of Eurocode 0; and Part B, in which the constitutive behavior of the material is analyzed more in depth, in order to evaluate the dependency on the intrinsic roughness and irregularities of the WAAM-produced material.

In Part A, Chapter 2 regards the development of 3D printing technologies over the past years, especially in relation to the construction industry (section 2.1), an overview of the main processes that are employed (section 2.2), and a rundown of advantages and disadvantages of this technology (section 2.3).

Chapter 3 covers in detail Wire-and-Arc Additive Manufacturing, which is the technique adopted for the production of the specimens whose results are analyzed later on, and specifically highlights the peculiarities and issues that this kind of material carries, and how these might affect designing (section 3.2).

Eurocode 0 [1], and in particular Annex D (section 4.3), is dealt with in Chapter 4, presenting an overview on the general methodology followed by the code (section 4.1), as well as how design resistance is approached and evaluated (section 4.2).

Chapter 5 deals with the statistical analysis of the provided experimental data, whose characteristics are described in section 5.1, in terms of mechanical (section 5.2) and geometrical (section 5.3) properties.

Chapter 6 is the crux of Part A: it delves into the determination of both characteristic and design resistance functions, at yielding (section 6.4) as well as at the ultimate state (section 6.5). Finally, this allows for the calibration of the partial safety factors provided by the Code [2].

All findings and observations regarding part A are then collected and summarized in Chapter 7.

Part B is focused on calibrations of available stress-strain models, in order to decouple the mechanical behavior from the geometrical features.

Chapter 8 provides an overview on Finite Element Analysis: in particular, section 8.1 highlights the steps that comprise the so-called Finite Element Method; while section 8.2 underlines advantages and limitations of this approach.

Chapter 9 regards a first calibration of the stress-strain models of two rough specimens (one longitudinal and one transversal), for which Digital Twins are provided: section 9.1 offers a general overview on the specimens themselves, as well as on the approach followed for said calibration. Section 9.2 defines the general approaches followed for the determination of stress-strain models. Longitudinal specimen 3A is then thoroughly analyzed in section 9.3, while section 9.4 focuses on transversal specimen 4D.

In Chapter 10, the stress-strain model obtained from milled specimens, hence not influenced by the geometry, is applied to the Digital Twin: section 10.2 analyzes the mechanical properties of longitudinal milled specimens applied to specimen 3A's geometry; similarly, in section 10.3 the averaged mechanical behavior of transversal machined specimens is applied specimen 4D's Digital Twin.

Following the opposite approach, Chapter 11 analyses a Digital Input Model, hence characterized by a regular (effective) geometry, for which the mechanical behavior is that of the rough specimen. Section 11.2 delves into the properties of specimen 3A, while section 11.3 focuses on specimen 4D.

Finally, all results of part B are reported and discussed in Chapter 12; while Chapter 13 offers an overview on the entire study.

1.2 Objectives

The main objective of this study is to define some initial guidelines for the design of 3D-printed stainless-steel structural elements, on two different levels of detail: the first regards the determination of characteristic values and safety factors, the second the analysis and calibration of stress-strain curves for the development of Finite Element Models.

The focus of Part A is precisely on the application of the procedures delineated in Annex D of Eurocode 0, starting from the evaluation of the mechanical and geometrical properties of 3D-printed stainless-steel, through the acquisition and assessment of experimental testing previously performed on WAAM-produced specimens. Said tests have been conducted at the University of Bologna by the research group composed by Prof. Tomaso Trombetti, Eng. Dr. Vittoria Laghi and P.E. Michele Palermo.

Part B is centered around the analysis and calibration of stress-strain models, aiming at a more accurate understanding of the material and its behavior.
This approach allows to understand in depth what is the influence that the geometrical imperfections, which are proper of the WAAM-produced material, have on its mechanical behavior, especially within the elastic phase.

PART A: DEFINITION OF A DESIGN PROCEDURE TO PREDICT THE STRUCTURAL BEHAVIOR OF WAAM-PRODUCED STAINLESS-STEEL ELEMENTS

2. Additive Manufacturing (AM)

2.1 Background on Additive Manufacturing

3D printing, or, more accurately, Additive Manufacturing (AM), has been extensively studied and used over the past few decades, especially for the production of plastics. Regarding metals, this technology has been used especially in automotive, aerospace and naval engineering applications, with the production of parts, turbines and propellers (Figure 2.1).

Within the construction industry, this technology has been introduced just over the past few years and it is still at its initial stage, while steadily developing, nonetheless. As reported in [3], Additive Manufacturing processes in construction are related to the production of concrete, polymer and metal structures.

With regards to metals, and in particular steel, the focus has mainly been on modest-scale components, such as façade nodes (Figure 2.2) and connections, since this technology allows for an optimization of geometries, as described in [4]; although, very recently, the first full-scale 3D printed stainless-steel bridge was produced, tested and installed in Amsterdam, and has been open to the public starting July 2021 (Figure 2.3). This was achievable through Wire-and-Arc Additive Manufacturing (WAAM), discussed more in detail in section 3, which allows for the production of large-scale elements, differently from Powder-Based Fusion (PBF) technologies, which had been employed so far for the production of small-scale connections, as it provides a higher level of precision.

WAAM is more suitable for the construction industry, as it produces elements at a faster rate than powder-based techniques. Faster rates of production obviously lead to less precise outcomes; and while this would not be feasible in other application fields, such as the previously cited automotive and aerospace industries, it can be allowed in construction.

This will undoubtedly lead to a microstructure characterized by geometrical imperfections [5], which, in return, will have an impact on mechanical properties, dependent also on the anisotropic nature of the so-produced material [6]: these limitations and peculiarities need to be addressed in order to approach the design of structural elements produced using such materials and by means of such techniques, with the definition of new guidelines, based on the existing ones expressed in the relative Eurocodes.

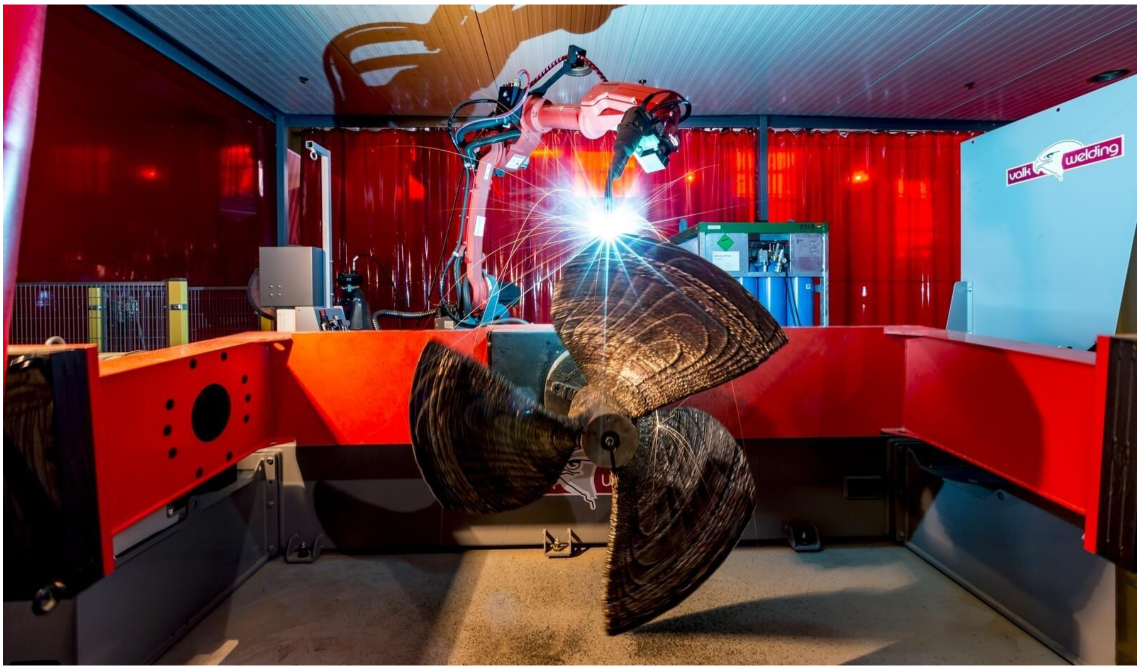

Figure 2.1 – First class-approved 3D-printed ship propeller, 2017 [7]

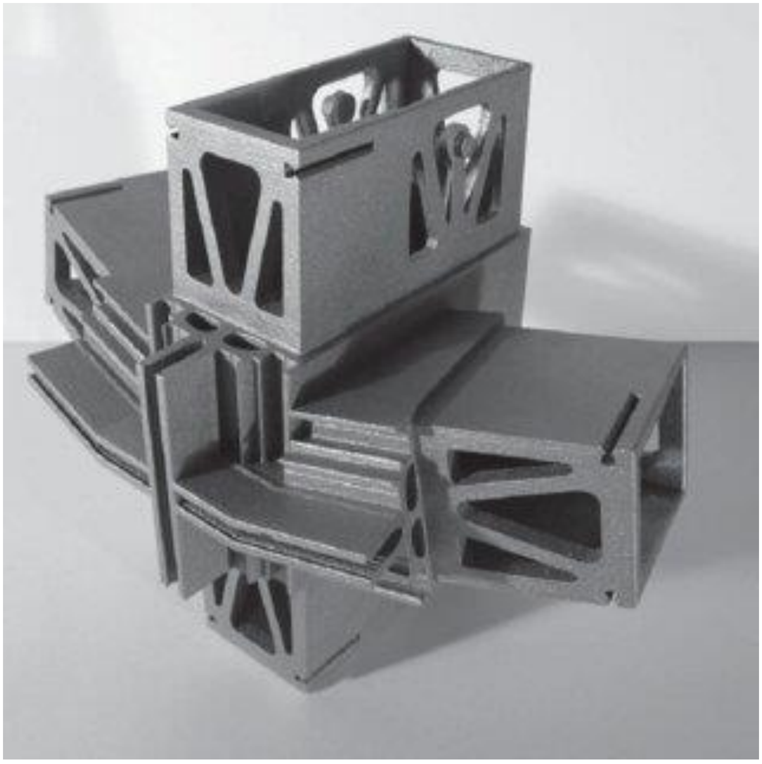

Figure 2.2 – Full-size aluminum prototype Nematox façade node, 2012 [8]

Figure 2.3 – First 3D-printed stainless-steel bridge, 2021 [9]

2.2 Overview of Additive Manufacturing techniques for metals

3D printing technologies for metals can be divided into four main groups, according to the process used for their production: liquid-based, solid-based, wire-based and powder-based (Figure 2.4). The most widely used processes are powder-based and wire-based (schematized in Table.2.1): the first can be divided into power-fed and power-bed.

In power-fed processes, the material is deposited by means of a nozzle, and the energy source can either be plasma or laser; the most relevant processes based on the latter are Laser Metal Deposition (LMD), Direct Metal Deposition (DMD) and Laser Engineered Net Shaping (LENS). In powder-bed processes, the material is stacked on the bed and is melted in order to obtain the desired shape, and this can be done either with electrons (Electron Beam Melting – EBM) or laser (Direct Metal Laser Sintering – DMLS, Selective Laser Sintering – SLS, and Selective Laser Melting – SLM) as the source of energy.
These processes give more precise outcomes but require extended periods of time and are quite expensive, since they require that the metal is previously transformed into powder, which is not even entirely employed, due to the process itself.

In wire-based processes, metal wires are employed as they are, and each layer is welded on top of the previous one, differently depending on the technique: WAAM (Wire-and-Arc Additive Manufacturing) is a Direct Energy Deposition (DED) process in which the heat source is an electric arc; in WLAM (Wire Laser Additive Manufacturing) and Shaped Metal Deposition (SMD) processes, the wires are melted by means of a laser source; EBFF (Electron Beam Freeform Fabrication) requires electrons as the source of energy.

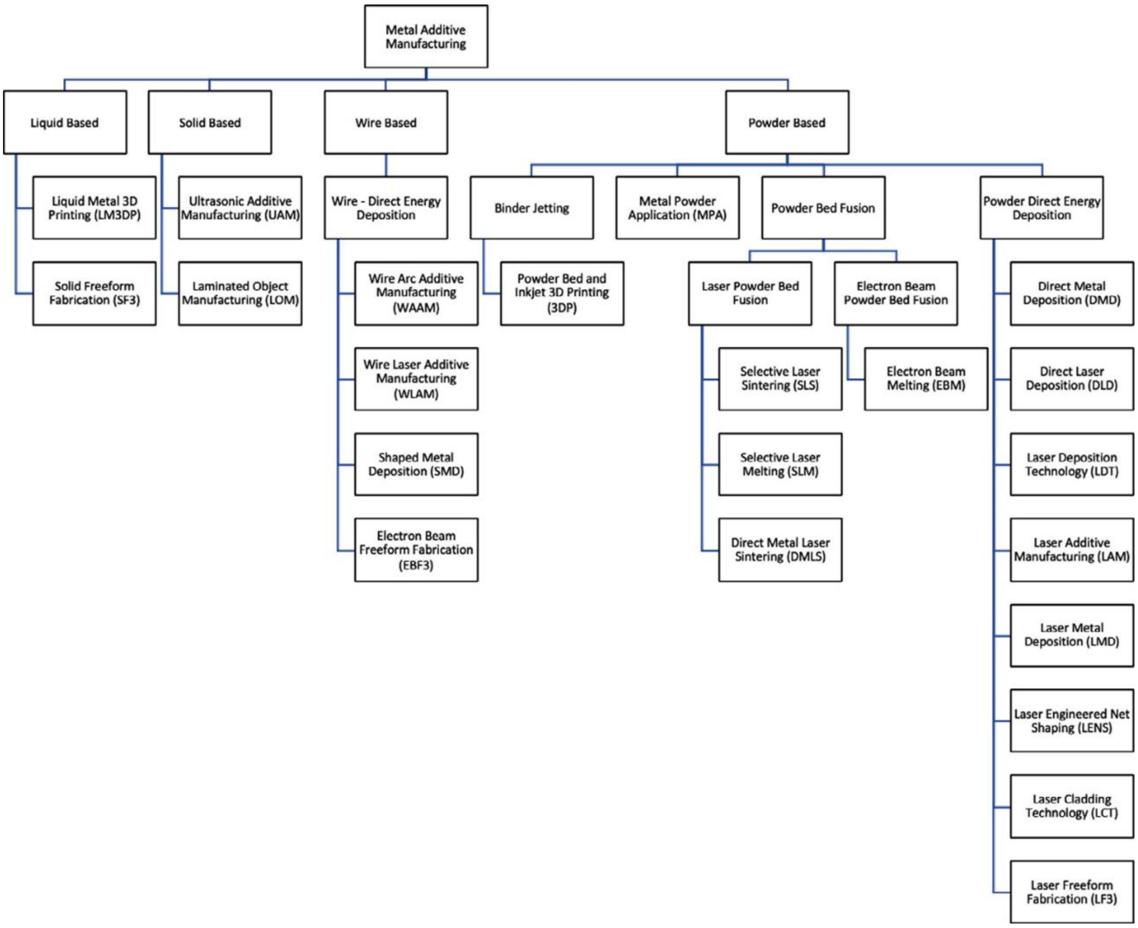

Figure 2.4 – Schematization of AM techniques for metals [10]

material	**type**	**energy source**	**main processes**
powder	bed	laser	DMLS, SLS, SLM
		electrons	EBM
	fed	laser	LMD, DMD, LENS
		plasma	-
wire	-	arc	WAAM
		laser	WLAM, SMD
		electron	EBFF

Table.2.1 – Main AM processes for metals

2.3 Advantages and disadvantages of Additive Manufacturing processes

There are many advantages in the use of 3D printing for steel elements (Table 2.2). The main positive feature is the level of adaptability that these processes carry: this allows for flexibility in the planning and designing of new structures and possible further extensions.

Another advantage is the speed at which elements and components can be produced, and especially installed, allowing for shorter construction times, and hence making buildings and infrastructures feasible sooner than if they were produced using traditional techniques.

Furthermore, 3D printing requires less material, as it allows for the production of the desired shapes and dimensions and does not need post-processing to eliminate excessive material or the use of molds to cast the material beforehand, and allows for the optimization of geometries. This also leads to lighter structures, which means that foundations' dimensions can be decreased, hence less material is needed and consequently costs are lower.

Often, to reduce traditional production costs, it is more convenient to mass produce elements such as connections; but with AM processes, these components can be produced singularly, without increasing such costs extensively, and even requiring much less storage.

Feature	Leading to	Advantage	
		in buildings	in bridges
1. Speed of construction	Quick erection to full height of self supporting skeleton	Can be occupied sooner	Less disruption to public
2. Adaptability	Future extension	Flexible planning for future	Ability to upgrade for heavier loads
3. Low construction depth	Reduced height of structure	Cheaper heating Reduced environmental effect	Cheaper earthworks Slender appearance
4. Long spans	Fewer columns	Flexible occupancy	Cheaper foundations
5. Permanent slab formwork	Falsework eliminated	Finishes start sooner	Less disruption to public
6. Low weight of structure	Fewer piles and size of foundations Typical 50% weight reduction over concrete	Cheaper foundations and site costs	
7. Prefabrication in workshop	Quality control in good conditions avoiding sites affected by weather	More reliable product Fewer specialist site operatives needed	
8. Predictable maintenance costs	Commuted maintenance costs can be calculated. If repainting is made easy by good design, no other maintenance is necessary	Total life cost known Choice of colour	
9. Lightweight units for erection	Erection by smaller cranes	Reduced site costs	
10. Options for site joint locations	Easy to form assemblies from small components taken to remote sites	Flexible construction planning	

Table 2.2 – Advantages of AM production [11]

There are, of course, disadvantages as well: the main one is certainly the fact that production costs, as of right now, are higher for Additively Manufactured components, as they are still niche products, since their development from a design point of view is still at its initial stage and the material is still being studied, hence not largely demanded.
Another downside is the fact that they, in general, require very specific machinery, which is only owned and available in few companies, hence it is not that simple to access such products. But, again, this issue persists as long as AM processes and products are not well-known and therefore more affordable and available on a larger scale.
The main challenge regarding 3D-printed materials regards their anisotropic nature due to the inherent irregular geometry and surface roughness, which must be addressed before these materials can be systematically employed in the construction industry.

3. Wire-and-Arc Additive Manufacturing (WAAM)

3.1 Overview of WAAM

In general, an Additive Manufacturing process requires a heat source, feedstock and a motion system that deposits the material provided [12].
Wire-and-Arc Additive Manufacturing is a Direct Energy Deposition process that combines an electric arc as the heat source and a wire as the feedstock, while motion is provided by either numerical computer-controlled supports or a robotic arm. For this process, off-the-shelf equipment is employed, namely the welding power source, torches and the wire-feeding system. This kind of set up allows for freedom from a dimensional point-of-view, which aligns well with the demands of structural engineering applications, which can be characterized by significant lengths: the MX3D bridge in Amsterdam is the first example of the extent and capabilities of this technology in this field (Figure 2.1).
This process deposits layers that are 1 to 2 mm thick, resulting in a surface roughness of about 0.5 mm for single-track deposit, which is acceptable for medium- to large-scale elements, hence for structural elements.

In WAAM processes, welding can be performed by different means:

- GMAW (Gas Metal Arc Welding)
- GTAW (Gas Tungsten Arc Welding)
- PAW (Plasma Arc Welding)

These processes, as well as other set-up parameters regarding the heat source, the deposition of the material and the feedstock itself (Table 3.1), widely influence the outcome, and therefore they must be explicitly stated: MX3D [9], who produced the tested specimens whose outcomes are analyzed later in this thesis, uses a GMAW process, characterized by a continuous wire electrode which is drawn from a reel by an automatic wire feeder [3]; the wire is fed through the contact tip in the welding torch, while the heat is transferred from the welding arc causing the wire to melt [13]. Motion is provided by industrial multi-axis ABB robots, which could theoretically print form any angle.
There are two feasible printing strategies that can be followed in WAAM: continuous printing and dot-by-dot printing. According to the latter, the material is deposited by successive points; while in continuous printing, as the name suggests, the material is laid in continuous layers.

The provided and later analyzed data have been collected from tests performed on specimens produced using continuous printing strategy, GMAW process and the parameters reported in Table 3.1.

process parameter	**details**	**value**
deposition power	current	100-140 A
	arc voltage	18-21 V
speed	welding speed	15-30 mm/s
	wire-feed rate	4-8 m/min
	deposit rate	0.5-2 kg/h
distance and angle	layer height	0.5-2 mm
	electrode-to-layer angle	90°
wire	wire grade	ER308LSi
	wire diameter	1 mm
shield gas	shield-gas type	98% Ar, 2% CO_2
	shield-gas flow rate	10-20 L/min

Table 3.1 – Process parameters used by MX3D [3]

3.2 Design issues related to WAAM

Wire-and-Arc Manufacturing presents a series of challenges regarding the produced material, which are not characteristic of the traditional one.

Among these issues, which may concern porosity, residual stresses, cracking and delamination, what is of outmost interest from a design point-of-view is the anisotropy of the material as well as the irregularities present in the produced geometry.

Regarding the geometry of the 3D-printed element, it is characterized by a rough surface (Figure 3.1), due to the production technique, which comprises the deposition and welding of wires. Additionally, as stated in section 2.1, WAAM produces elements at higher deposition rates than other AM techniques, causing the outcomes to be less precise.

As analyzed in detail in [14], the rough surface of the produced elements causes a variability in their cross-sectional area, which may then lead to a non-uniform distribution of stresses, affecting the mechanical performance of the material.

Therefore, it is important to somehow quantify the geometrical irregularity and, consequentially, its influence on the mechanical behavior of the material.

This can be done first by establishing a relationship between nominal and effective dimensions (as done in section 5.3.4), and then through a further calibration by means of the definition of partial safety factors (performed in chapter 6).

Figure 3.1 – Close-up of the rough surface of WAAM specimens [14]

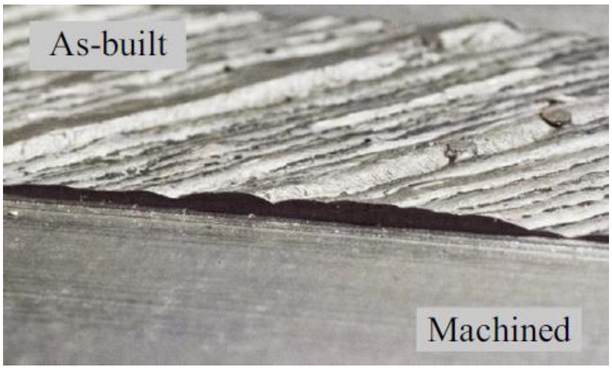

Figure 3.2 – Comparison between as-built and machined surfaces [5]

Additionally, the WAAM-produced material is characterized by anisotropy, meaning that the material's behavior is dependent on directionality. Hence, its mechanical properties vary depending on the direction loads are applied to the element.

Therefore, the material must be studied and tested along different directions (elaborated on in section 5.2), in order to see how its mechanical properties change, and which are the orientations for which it performs best (i.e. presents higher stress levels, higher ductility) and worst.

The mechanical behavior of the material can also be influenced by the rough nature of the produced surfaces. Generally, according to previous studies, such as [5], [15], [14], milled specimens tend withstand larger stresses.

Figure 3.3 displays, from a merely qualitative point of view, how stress-strain curves can change with respect to load directionality, as well as to whether the specimens are subjected to post-production processes aimed at obtaining smooth surfaces.

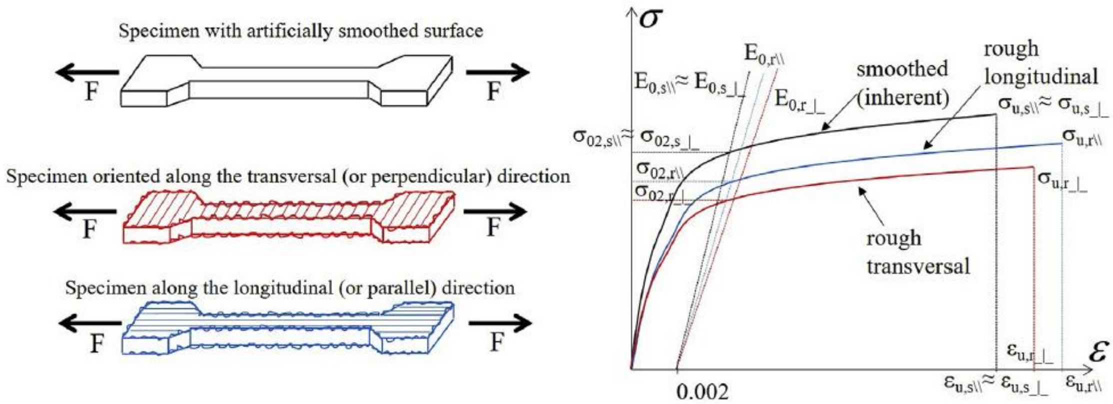

Figure 3.3 – Qualitative stress-strain curves depending on printing direction and milling [15]

Another process that can influence the mechanical behavior of the material is the cooling strategy. This process can, in general, either be controlled or uncontrolled: in the first case, in between the deposition of successive layer, compressed air is blown onto the previous layer, hence reducing the waiting time during production; the latter simply means that each layer is left to naturally cool down, without speeding up the process in any way.
[14] observes how the main difference in the mechanical response between specimens produced adopting active and uncontrolled cooling is that the latter for elongations at rupture that are 1.5-2x those reached by actively-cooled specimens.
The differences between the outcomes of the two strategies can also be appreciated in terms of effective thickness: in chapter 6, it can be appreciated how, for both directions L and T, specimens realized with uncontrolled cooling have larger values of the effective thickness, and in particular, on average they are larger than the nominal value. This can be appreciated in terms of a coefficient φ, relating effective and nominal values, which is reported in Table 6.1 and Table 6.4, for L and T specimens respectively.

Finally, regarding mechanical properties, from a design point-of-view, there are two viable approaches: either control the direction the element is produced, so that it can perform at its best under the required loading conditions, or deal with the element as if it were isotropic, assuming the mechanical properties related to the worst behavior, in order to follow a safe approach.

4. Eurocode 0

Eurocode 0, or EN 1990 [1], establishes principles and requirements for the safety assessment of structures, in conjunction with EN 1991 to EN 1999, describing the basis of their design, providing guidelines for structural reliability. Furthermore, Eurocode 0 defines a procedure for design assisted by testing on the basis of a semi-probabilistic approach; said procedure is described in its Annex D.

4.1 Partial safety factor method

As thoroughly explained in Part 6 of [1], this method assigns safety factors to characteristic values of loads and resistances in order to obtain design values for which the following must hold:

$$E_d \leq R_d \tag{4.1}$$

where:

E_d is the design value of the action

R_d is the design value of the resistance

Safety factors are defined based on either, or both:

- statistical evaluation of experimental data;
- calibration to experience from a long building tradition.

These values should be calibrated in order to reach a reliability level that is as close as possible to the target one; this calibration can be performed based on full probabilistic methods, which often cannot be carried out due to lack of data, or on First Order Reliability Methods.
Viable reliability methods are shown in Figure 4.1 below.

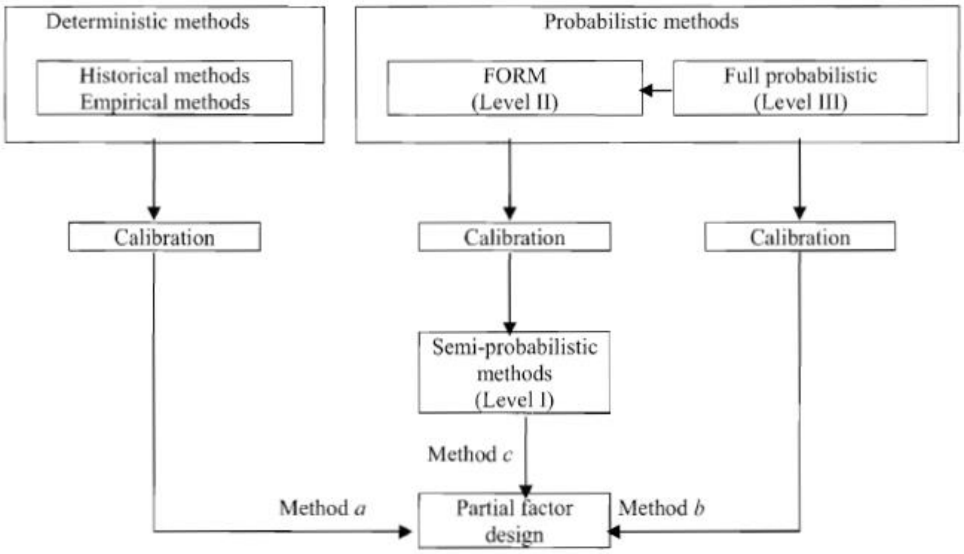

Figure 4.1 – Reliability methods [1]

Annex B of [1] indicates the appropriate level of safety that should be guaranteed depending on the Consequence Class (CC). As reported in Table 4.1, each Consequence Class is defined on the basis of the impact that the failure of the structure would have in terms of casualties, as well as economic, social and environmental effects.

Consequences Class	Description	Examples of buildings and civil engineering works
CC3	**High** consequence for loss of human life, *or* economic, social or environmental consequences **very great**	Grandstands, public buildings where consequences of failure are high (e.g. a concert hall)
CC2	**Medium** consequence for loss of human life, economic, social or environmental consequences **considerable**	Residential and office buildings, public buildings where consequences of failure are medium (e.g. an office building)
CC1	**Low** consequence for loss of human life, *and* economic, social or environmental consequences **small or negligible**	Agricultural buildings where people do not normally enter (e.g. storage buildings), greenhouses

Table 4.1 – Definition of consequence classes [1]

Reliability Classes (RC) are directly associated with Consequence Classes, and correspond to a certain range of values of the reliability index β, as shown in Table 4.2. This index expresses the probability of failure as defined through the Cumulative Distribution Function (CDF) of the standard normal distribution, namely:

$$P_f = \Phi(-\beta) \tag{4.2}$$

Reliability Class	Minimum values for β	
	1 year reference period	50 years reference period
RC3	5,2	4,3
RC2	4,7	3,8
RC1	4,2	3,3

Table 4.2 – Recommended values for the reliability index β [1]

Annex C of [1] provides the relationship between P_f and β, as reported in Table 4.3.
The reliability index accounts for scatteredness of both actions and resistances, and it is usually expressed as normalized with respect to standard deviations σ_E and σ_R, as can be seen in Figure 4.2, which shows that the design point according to a First Order Reliability Method is the point on the failure surface that is closest to the average point in the space of normalized variables.

P_f	10^{-1}	10^{-2}	10^{-3}	10^{-4}	10^{-5}	10^{-6}	10^{-7}
β	1,28	2,32	3,09	3,72	4,27	4,75	5,20

Table 4.3 – Relation between P_f and β [1]

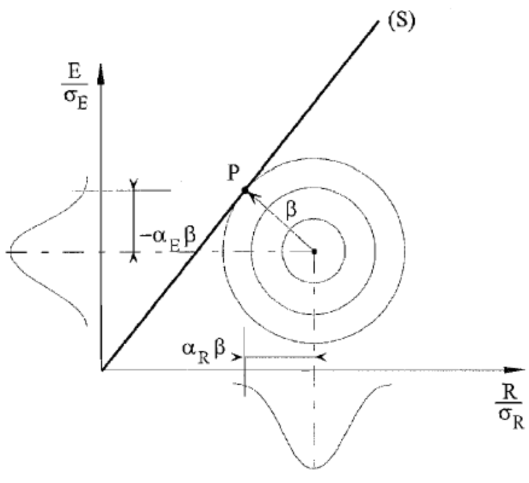

(S) failure boundary $g = R - E = 0$
P design point

Figure 4.2 – Reliability index β according to FORM [1]

According to [16], the target reliability index corresponds to the minimum requirement for human safety related to the expected number of fatalities. The nominal life of a structure, i.e. the reference period, depends on the type of structure and its intended use; for most structures, the design life is 50 years, and they belong to CC2, hence corresponding to β=3,8.

The design values of action effects E_d and of resistances R_d should be evaluated such that equations (4.3) and (4.4) hold.

$$P(E > E_d) = \Phi(+\alpha_E \beta) \tag{4.3}$$

$$P(R \leq R_d) = \Phi(-\alpha_R \beta) \tag{4.4}$$

where:

α_E, α_R are the FORM sensitivity factors, for which $|\alpha| \leq 1$

α_E is negative while α_R is positive, as to provide the most unfavorable scenario for both acting effects and resistances. Annex C considers as valid values for α_E and α_R, respectively, -0.7 and 0.8, provided that equation (4.5) is verified.

$$0{,}16 < \sigma_E / \sigma_R < 7{,}6 \tag{4.5}$$

This assumption is fundamental in order to be able to consider and analyze the resistance function without having to account for loading.

There are several safety factors defined throughout the Code, depending on whether they refer to resistances or acting loads, and what type of uncertainty they account for. They are reported and schematized in Figure 4.3 here below.

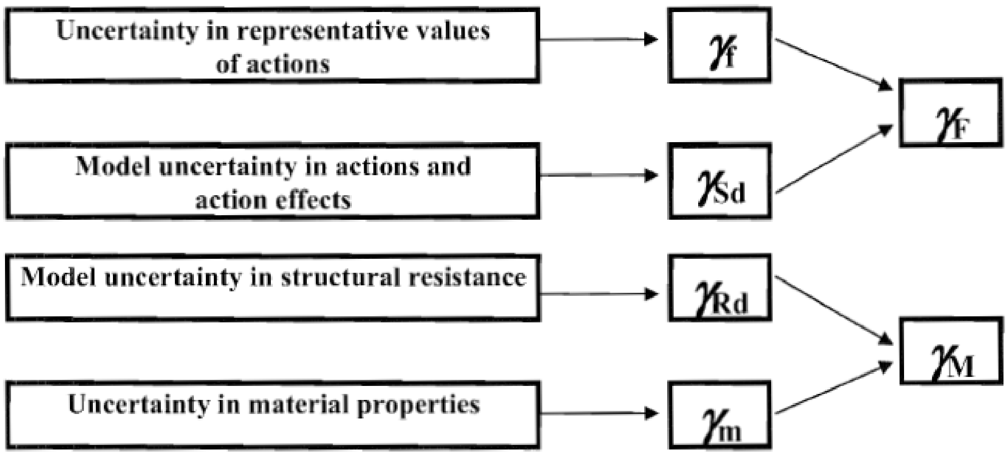

Figure 4.3 – Relation between individual partial factors [1]

In accordance with Figure 4.3 and [16]:

$$\gamma_F = \gamma_f \times \gamma_{Sd} \tag{4.6}$$

$$\gamma_M = \gamma_m \times \gamma_{Rd} \tag{4.7}$$

4.2 Evaluation of the design resistance

Section 6 of [1], as stated earlier, is dedicated to the safety verification by means of the partial safety method. In particular , Section 6.3.5 proposes three possible alternatives for the definition of the design resistance.

4.2.1 Method 1 – general formulation

In general, the design resistance R_d can be evaluated as:

$$R_d = \frac{1}{\gamma_{Rd}} R\{X_{d,i}; a_d\} = \frac{1}{\gamma_{Rd}} R\left\{\eta_i \frac{X_{k,i}}{\gamma_{m,i}}; a_d\right\} \quad i \geq 1 \tag{4.8}$$

where:

γ_{Rd} is a partial safety factor accounting for uncertainties in the resistance model

$X_{d,i}$ is the design value of material property i

a_d is the design value of geometrical data

According to section 6.3.3 of [1], the design value of a material or product property is generally expressed as:

$$X_d = \eta \frac{X_k}{\gamma_m} \tag{4.9}$$

where:

η is the mean value of the conversion factor, and it accounts for volume and scale effects, moisture and temperature effects, and any other relevant parameter

γ_m is the partial factor for the material property, accounting for possible unfavorable deviations from the characteristic value, as well as the random part of η

X_k is the characteristic value of the material property

Section 6.3.4 of [1] concerns geometric properties, whose design value generally corresponds to the nominal value:

$$a_d = a_{nom} \tag{4.10}$$

When the effects of deviations of the geometrical data from the nominal value become significant in terms of reliability of the structure, equation (4.10) becomes:

$$a_d = a_{nom} \pm \Delta a \tag{4.11}$$

where:

Δa accounts for possible unfavorable deviations from the nominal value, as well as the cumulative effect of a simultaneous occurrence of multiple geometrical deviations

Equation (4.8) can also be simplified as:

$$R_d = R\left\{\eta_i \frac{X_{k,i}}{\gamma_{M,i}}; a_d\right\} \quad i \geq 1 \tag{4.12}$$

where:

$\gamma_{M,i}$ is computed according to equation (4.7) and the specific $\gamma_{m,i}$; it may also incorporate the correction factor η_i

4.2.2 Method 2 – simplified formulation

Alternatively to equation (4.12), the design resistance can be expressed without explicitly determining the design values of all basic variables, simply obtaining it from the characteristic value of a material or product resistance:

$$R_d = \frac{R_k}{\gamma_M} \tag{4.13}$$

This formulation can be exploited for products or members made of a single material and also sued in connection with Annex D of [1]; furthermore, as noted in [17], it is employed for the evaluation of the design resistance of most failure modes of EN 1993 [2].

4.2.3 Method 3 – non-linearity

For structures or structural members that are analyzed by mans of non-linear methods and are comprised of more than one material, the following expression can be used instead of (4.12) and (4.13):

$$R_d = \frac{1}{\gamma_{M,1}} R\left\{\eta_1 X_{k,1}; \eta_i X_{k,i} \frac{\gamma_{m,1}}{\gamma_{m,i}}; a_d\right\} \quad i > 1 \tag{4.14}$$

4.3 Annex D – Design assisted by testing

4.3.1 Overview

Annex D of Eurocode 0 [1] outlines, by means of a semi-probabilistic approach, procedures for the safety assessment of design methods.

Firstly, it defines and differentiates several types of testing depending what their scope is, and they can be divided into two main categories, according to [16]:

- tests whose results are directly used in design, through the application of the statistical techniques addressed in Annex D itself, and further explained later on in this section;
- control or acceptance tests, which are valid whenever there is no availability of test data at the time of design.

Furthermore, section D4 of Annex D explains in detail how tests should be planned and carried out. This is not of particular interest in the development of this thesis, as the experimental data used have been performed accordingly prior to this project.

Regarding the derivation of design values for a material property, a model parameter or a resistance, section D5 of Annex D states that it should be either done following either:

- Method A: assessment of a characteristic value, a safety factor, and possibly a conversion factor, needed to determine the design value, in accordance with expressions (4.8), (4.13) and (4.14);
- Method B: direct determination of the design value.

The derivation of the characteristic value for Method A should account for the scatteredness of data, the statistical uncertainty related to the number of tests, and the prior statistical knowledge. The partial safety factor should be taken from the appropriate Eurocode, provided that the tests are sufficiently similar to the usual field of application in which the partial factor is employed; otherwise, they can be calibrated by means of correction factors.

The evaluation of test results is quite a sensitive matter and requires particular attention.

Firstly, the behavior of test specimens should be compared with theoretical predictions; when this does not hold, additional testing may be required.

The evaluation of test results should be based on statistical methods, as explained in section D6 of Annex D, given that the following conditions are satisfied:

- the statistical data are taken from an identified, sufficiently homogeneous population;
- a sufficient number of observations is available.

The level of interpretation of results, in fact, depends on the number of performed tests:

1. if very few tests are performed, the results must be implemented with extensive prior knowledge (Bayesian procedures);
2. if a larger series of tests is performed, a classical statistical interpretation if possible, with the addition of some previous knowledge on the analyzed parameter;
3. if a very large series of tests is performed, classical statistical interpretation is possible without accounting for any prior knowledge on the matter.

4.3.2 Statistical determination of a single property

Following Method A, namely assessing the characteristic value, the design value of a single property is computed as:

$$X_d = \eta_d \frac{X_{k(n)}}{\gamma_m} \qquad (4.15)$$

where:

η_d is the design value of the conversion factor

The Code allows to define the characteristic value of the analyzed property either following a Normal or a Lognormal distribution.

Which type of Probability Density Function (PDF) better describes the available set of data can be determined by means of goodness-of-fit tests, such as the Kolmogorov-Smirnoff test, which compares the CDF of a sample with that of a reference probability distribution. Coefficient ks, resulting from this test, must be compared with a critical value cv, which depends on the number of data and on the significant level α (usually 0.5): the reference probability distribution is considered a good fit for the set of data as long as the value of ks is lower than cv.

In case of a Normal distribution:

$$X_{k(n)} = m_x(1 - k_n V_x) \qquad (4.16)$$

where:

n is the number of sample results

k_n is a factor that depends on the value of V_X and is taken from

m_x is the mean value of the n sample results

V_x is the coefficient of variation of X, which can be either known from previous knowledge or else computed as:

$$V_x = \frac{s_x}{m_x} \qquad (4.17)$$

s_x is the estimated value of the standard deviation of X, by definition:

$$s_x = \frac{\sum_i (x_i - m_x)^2}{n-1} \tag{4.18}$$

n	1	2	3	4	5	6	8	10	20	30	∞
V_X known	2,31	2,01	1,89	1,83	1,80	1,77	1,74	1,72	1,68	1,67	1,64
V_X unknown	-	-	3,37	2,63	2,33	2,18	2,00	1,92	1,76	1,73	1,64

Table 4.4 – Values of k_n for the 5% characteristic value [1]

If the sample fits a Lognormal distribution:

$$X_{k(n)} = e^{m_y - k_n s_y} \tag{4.19}$$

where:

$$m_y = \frac{\sum_i \ln(x_i)}{n} \tag{4.20}$$

if V_x is known from prior knowledge

$$s_y = \sqrt{\ln(V_x^2 + 1)} \cong V_x \tag{4.21}$$

if V_x is unknown

$$s_y = \sqrt{\frac{\sum_i \left(\ln x_i - m_y\right)^2}{n-1}} \tag{4.22}$$

4.3.3 Statistical determination of resistance models

Before dealing with the procedure needed to evaluate a resistance model, it is important to underline that the validity of said model should be checked by means of statistical interpretation of the available test data; if that is not the case, the model should be adjusted and checked again.

Some assumptions are made for the standard evaluation procedure:

- the resistance function is a function of independent variables $\underline{X}$;
- a sufficient number of tests is available;
- all relevant properties, both mechanical and geometrical, are measured;
- the variables in the resistance function are uncorrelated;
- all variables follow either a Normal or a Lognormal distribution.

The standard procedure is comprised of the following steps:

1. Develop a design model: the design model for the theoretical resistance r_t is represented by the resistance function expressed in (4.23).

$$r_t = g_{rt}(\underline{X}) \tag{4.23}$$

2. Compare experimental and theoretical values: the measured properties are put into the theoretical resistance function r_{ti} in order to compare it with the experimental values r_{ei} for each test specimen i.

   The points representing each pair of values (r_{ti}, r_{ei}) should be plotted on a diagram, as shown in Figure 4.4; if the resistance function is exact and complete, all the points will lie on the line characterized by θ=45°. In reality, the points will present some scatter, and the causes of the systematic deviation should be checked either in the test procedures or in the resistance function itself.

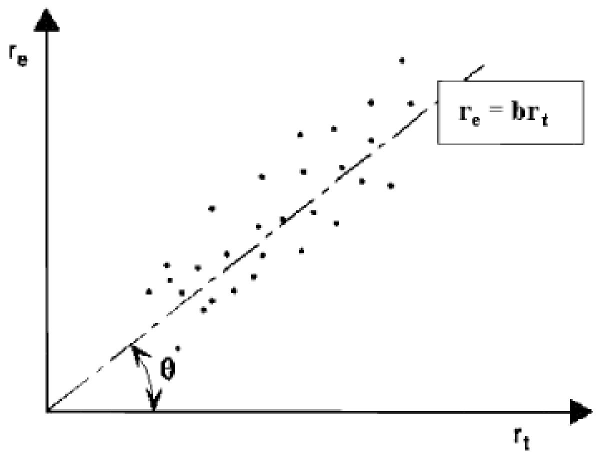

Figure 4.4 – r_e-r_t diagram [1]

3. Estimate the mean value correction factor b: the probabilistic model of the resistance can be written as reported in expression (4.24).

$$r = b r_t \delta \tag{4.24}$$

   where:

   b	is the correction factor, and is the "Least Squares" best fit to the slope

$$b = \frac{\sum r_e r_t}{\sum r_t^2} \tag{4.25}$$

   δ	is the error

   The mean value r_m of the theoretical resistance function can be computed using the mean values $\underline{X}_m$ of the basic variables.

$$r_m = b g_{rt}(\underline{X}_m)\delta \tag{4.26}$$

4. Estimate the coefficient of variation of the error: the error term δ_i is computed for each specimen i, as expressed in (4.27); it is then expressed in lognormal terms (expression(4.28)) and the mean and variance are computed following (4.29) and (4.30), respectively. Finally, the coefficient of variation of the error V_δ is computed as reported in (4.31).

$$\delta_i = \frac{r_{ei}}{br_{ti}} \tag{4.27}$$

$$\Delta_i = \ln \delta_i \tag{4.28}$$

$$\overline{\Delta} = \frac{\sum_i \Delta_i}{n} \tag{4.29}$$

$$s_\Delta^2 = \frac{\sum_i \left(\Delta_i - \overline{\Delta}\right)^2}{n-1} \tag{4.30}$$

$$V_\delta = \sqrt{\exp(s_\Delta^2) - 1} \tag{4.31}$$

5. Analyze compatibility: in order to build the resistance function, some assumptions have been made, and it is necessary to check whether the test population is compatible. This can be done by assessing the scatteredness of the (r_{ti},r_{ei}) values; in case the scatteredness needs to be reduced, one can either:
   - correct the design model in order to account for parameters that had been ignored in the definition of the resistance function;
   - modify the correction factor b and the coefficient of variation (CoV) of the error V_δ by subdividing the total population into subsets. In this case, k_n can still be referred to the initial population; furthermore, this subdivision may help determine which parameters have the biggest influence on the scatteredness.
6. Determine the coefficients of variation of the basic variables: the values of the CoV V_{Xi} for each basic variable X_i are computed as per definition of coefficient of variation; these values are then employed for the definition of V_{rt} of the theoretical resistance function, through expression (4.32), valid for simple resistance functions defined, for example, as the product of the basic variables. More in general, V_{rt} should be determined using (4.33).

$$V_{rt}^2 = \sum_j V_{xj}^2 \tag{4.32}$$

$$V_{rt}^2 = \frac{1}{g\left(\underline{X}_m\right)^2} \sum_j \left(\frac{\partial g_{rt}(X_j)}{\partial X_j} \sigma_j\right)^2 \tag{4.33}$$

7. Determine the characteristic/design value of the resistance: the scatteredness due to the model (V_δ) and that due to the basic variables (V_{rt}) can be combined into V_r, as reported in (4.34).

$$V_r^2 + 1 = \left(V_\delta^2 + 1\right)\left(V_{rt}^2 + 1\right) \tag{4.34}$$

The standard deviations of the lognormal variables are given by:

$$Q_\delta = \sqrt{\ln\left(V_\delta^2 + 1\right)} \tag{4.35}$$

$$Q_{rt} = \sqrt{\ln(V_{rt}^2 + 1)} \tag{4.36}$$

$$Q = \sqrt{\ln(V_r^2 + 1)} \tag{4.37}$$

Finally, the characteristic resistance r_k can be computed as:

$$r_k = b g_{rt}(X_m) \exp(-k_\infty \alpha_{rt} Q_{rt} - k_n \alpha_\delta Q_\delta - 0{,}5Q^2) \tag{4.38}$$

where:

$$\alpha_{rt} = \frac{Q_{rt}}{Q} \tag{4.39}$$

$$\alpha_\delta = \frac{Q_\delta}{Q} \tag{4.40}$$

and k_∞ and k_n can be found in Table 4.4.

If the number of test specimens is n>30, (4.38) becomes:

$$r_k = b g_{rt}(X_m) \exp(-k_\infty Q - 0{,}5Q^2) \tag{4.41}$$

The design value of the resistance is found following the same procedure as for the characteristic one, though equation (4.38) becomes (4.42), while (4.41) becomes (4.43):

$$r_d = b g_{rt}(X_m) \exp\left(-k_{d,\infty} \alpha_{rt} Q_{rt} - k_{d,n} \alpha_\delta Q_\delta - 0{,}5Q^2\right) \tag{4.42}$$

$$r_d = b g_{rt}(X_m) \exp\left(-k_{d,\infty} Q - 0{,}5Q^2\right) \tag{4.43}$$

where $k_{d,\infty}$ and $k_{d,n}$ are reported in Table 4.5.

n	1	2	3	4	5	6	8	10	20	30	∞
V_X known	4,36	3,77	3,56	3,44	3,37	3,33	3,27	3,23	3,16	3,13	3,04
V_X unknown	-	-	-	11,40	7,85	6,36	5,07	4,51	3,64	3,44	3,04

Table 4.5 – Values of $k_{d,n}$ for the ULS design value [1]

5. Statistical analysis of experimental results

5.1 Overview

Several data sets have been provided, regarding both mechanical and geometrical properties. The tested specimens, whose dimensions are reported in Figure 5.1, were both as-built, namely with a rough surface, and artificially machined. Furthermore, they are oriented differently with respect to the printing direction, i.e. parallel (or longitudinal – L), orthogonal (or transverse – T) and inclined at a 45° angle (or diagonal – D), as shown in Figure 5.2, due to the fact that the 3D-printed material is anisotropic, i.e. behaves differently with respect to the direction of the applied load, as more thoroughly explained in section 3.2.

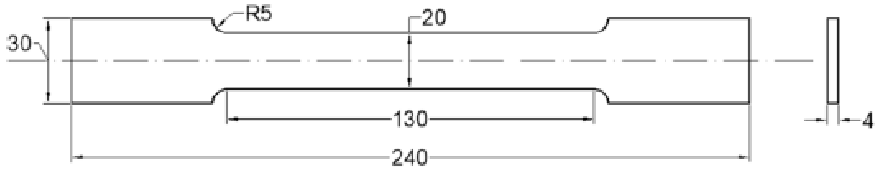

Figure 5.1 – Nominal dimensions (in mm) of test specimen [18]

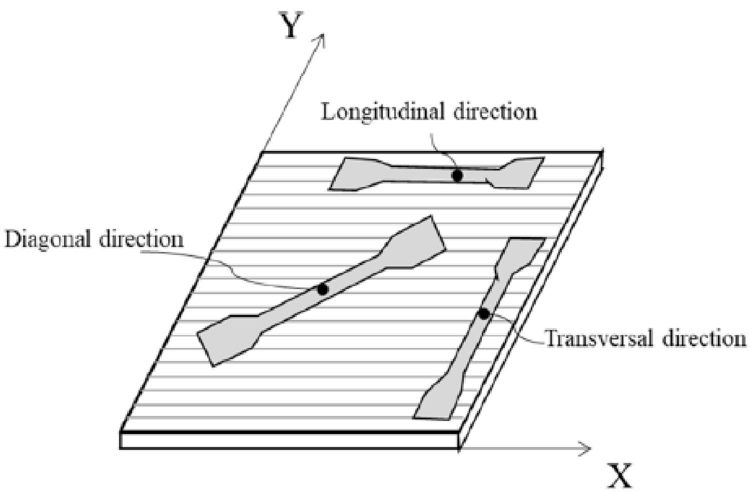

Figure 5.2 – Orientation of the test specimens [3]

5.2 Mechanical properties

In this dissertation, mechanical properties are only analyzed for machined specimens, i.e. mechanically milled samples, hence having a polished, more uniform finish, rather than as-built ones, which instead present a rough surface. The purpose of this is to have mechanical properties that are independent on geometrical irregularities, whose influence will be analyzed separately later on.

5.2.1 Experimental results

The results are taken from a set of 20 tensile tests performed on specimens oriented according to different inclinations with respect to the printing direction, as reported in Figure 5.2. Said tests were performed as follows: 5 on longitudinal (L) specimens, 5 on transverse (T) specimens, and 10 on diagonal (D) specimens. For sake of conciseness, said directions will be referred to as L, T and D respectively from this point onwards.

The analyzed mechanical properties are: Young's modulus E, 0.01% proof stress $\sigma_{0.01\%}$, 0.2% proof stress $\sigma_{0.2\%}$, ultimate stress σ_u, and ultimate strain ε_u. The results obtained from the tensile tests are reported in Table 5.1, in terms of mean value μ, standard deviation σ and coefficient of variation V.

parameter	**direction**	**μ**	**σ**	**V**
E [GPa]	L	138,54	5,65	0,041
	T	113,41	2,74	0,024
	D	247,29	32,85	0,133
$\sigma_{0.01\%}$ [MPa]	L	252,83	33,86	0,134
	T	250,79	37,11	0,148
	D	285,42	72,70	0,255
$\sigma_{0.2\%}$ [MPa]	L	340,33	13,99	0,041
	T	358,03	14,94	0,042
	D	416,97	39,56	0,095
σ_u [MPa]	L	564,47	18,26	0,032
	T	570,32	30,01	0,053
	D	616,05	58,79	0,095
ε_u [%]	L	26,53	3,82	0,144
	T	23,68	3,94	0,167
	D	27,76	7,07	0,255

Table 5.1 – Key mechanical parameters from tensile testing

Figure 5.3 below shows a graphical overview of said mechanical parameters for each direction, in terms of mean value and standard deviation.

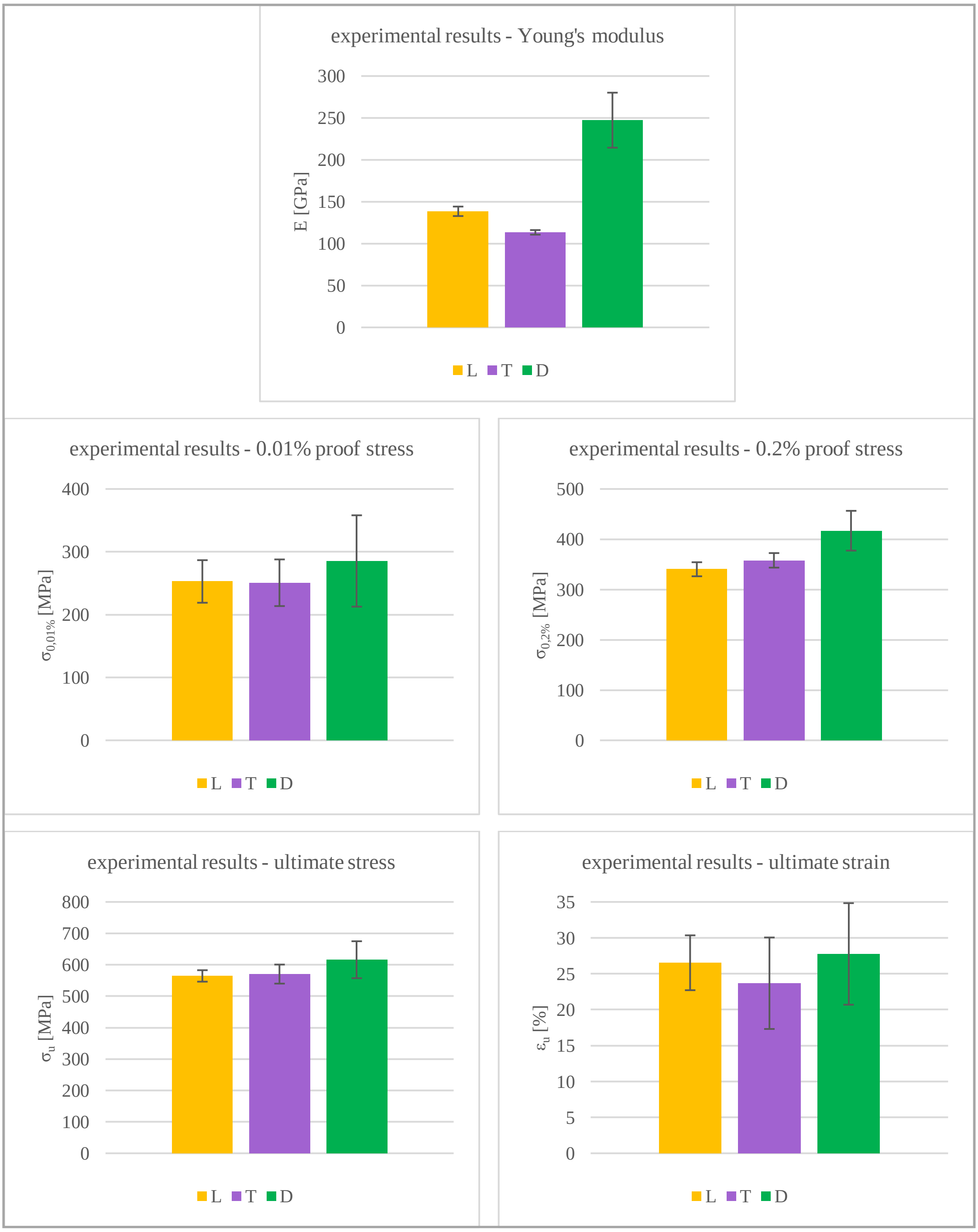

Figure 5.3 – Key mechanical parameters from tensile testing

These results make it very evident how anisotropic the material is, and hence how mechanical properties are dependent on the loading direction.

The main difference is found in terms of Young's modulus: D specimens present values that are, on average, about 120% larger than those for T specimens and about 80% larger than L specimens. Furthermore, it can be noticed how, for all of the analyzed mechanical properties, the diagonal direction performs better than the other two orientations. On the contrary, direction T presents the worst behavior in terms of all key mechanical properties, with the exception of 0.2% proof and ultimate stresses, for which L specimens present a slightly lower average value.
Additionally, ultimate strain is the property for which there is most uncertainty, as coefficients of variation are as high as 0.190 on average over the three directions; this is especially significant for D specimens.

5.2.2 Statistical interpretation of experimental data

In order to be able to apply the procedures outlined in Annex D, and specified in section 4.3.2 of this dissertation, the sets of experimental data should follow either a Normal or Lognormal distribution.

For this reason, statistical analyses are carried out in order to find the "best-fit" distribution of each mechanical parameter in each direction according to maximum-likelihood estimators, assuming Normal and Lognormal distribution models.
A comparison between the statistical distributions resulting from the collected experimental data and the best-fit cumulative (CDF) and probability (PDF) density functions is provided below: in Figure 5.4 for Young's modulus E, in Figure 5.5 for 0.01% proof stress $\sigma_{0.01\%}$, in Figure 5.6 for 0.2% proof stress $\sigma_{0.2\%}$, in Figure 5.7 for ultimate stress σ_u, and, finally, in Figure 5.8 for ultimate strain ε_u.
In the PDF plots, experimental data are presented in terms of relative frequency, scaled with reference to the magnitude of each statistical population.

Qualitatively speaking, in accordance with the values of the coefficients of variation, reported in Table 5.1, for Young's modulus and 0.2% proof stress in directions L and T, as well as ultimate stress in direction L, the Normal and Lognormal distributions are almost coincident.
Similarly, 0.01% proof stress and ultimate strain present Normal and Lognormal best-fit distributions that are quite different from each other, especially for D specimens.
From a numerical point of view, results in terms of mean values, standard deviations and coefficients of variation are reported in Table 5.2.

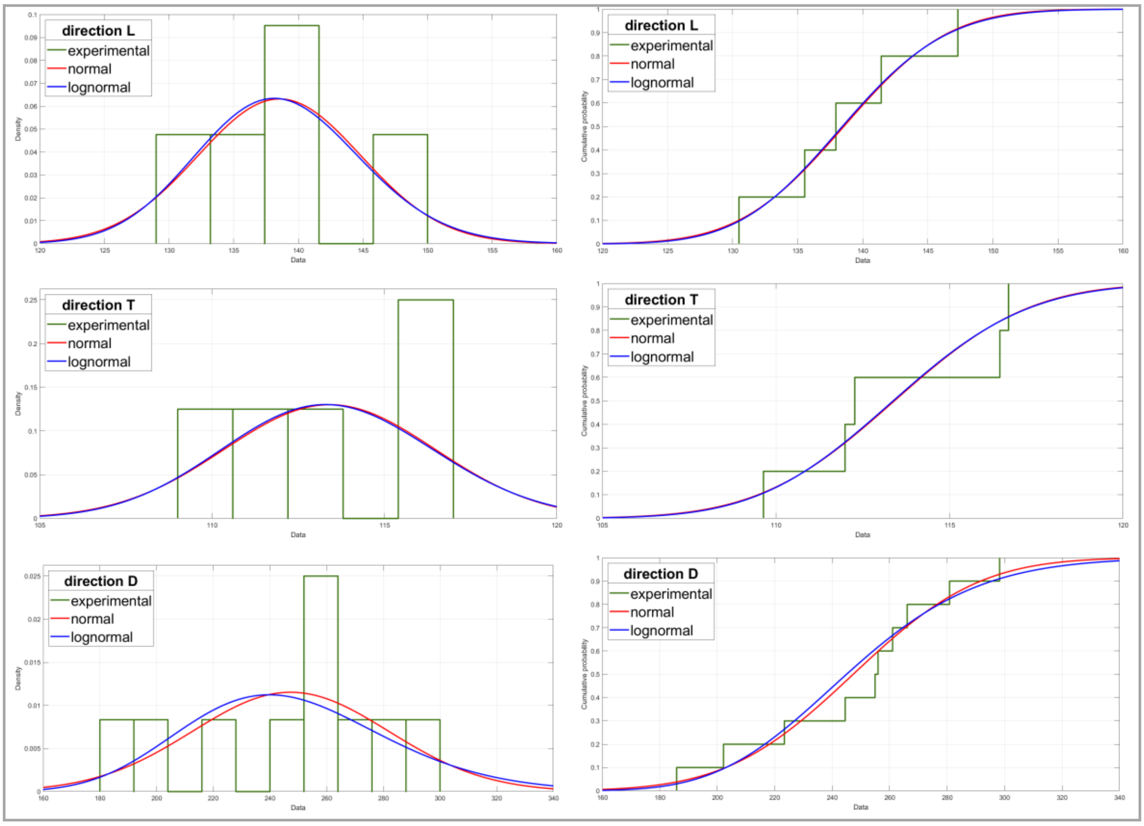

Figure 5.4 – Statistical distributions of Young's modulus E

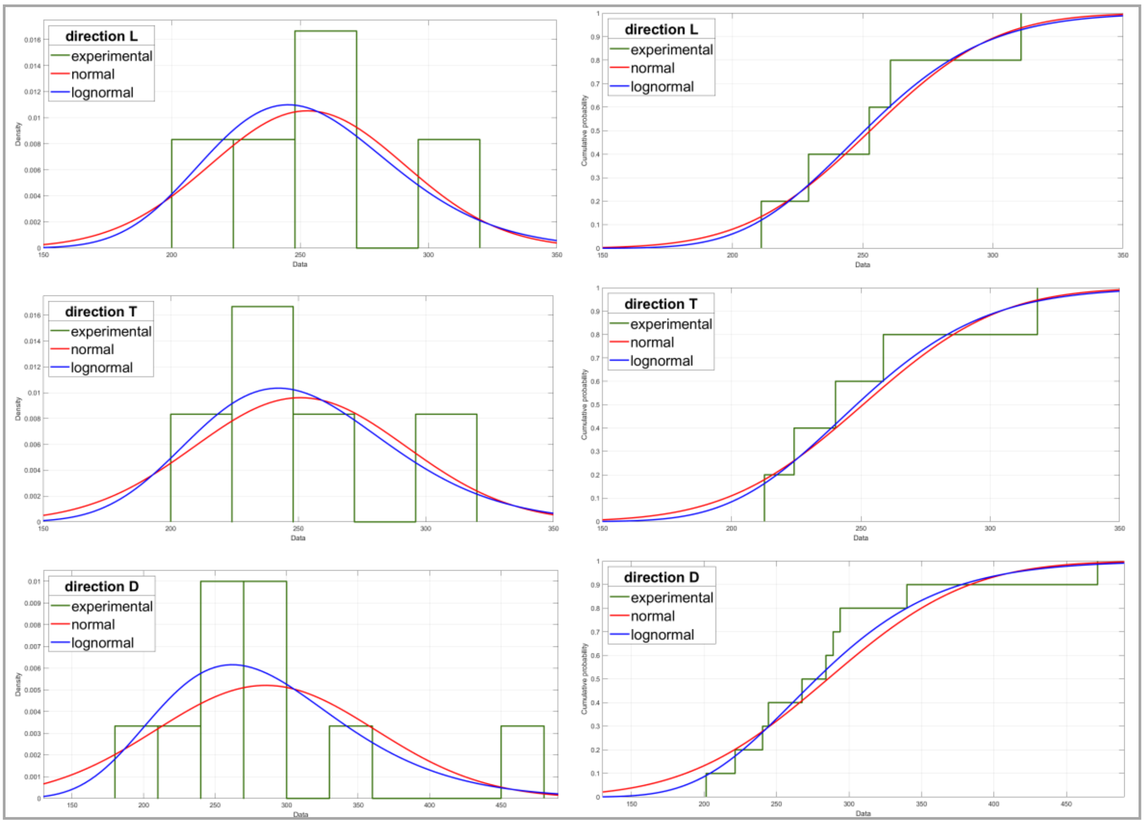

Figure 5.5 – Statistical distributions of 0.01% proof stress $\sigma_{0.01\%}$

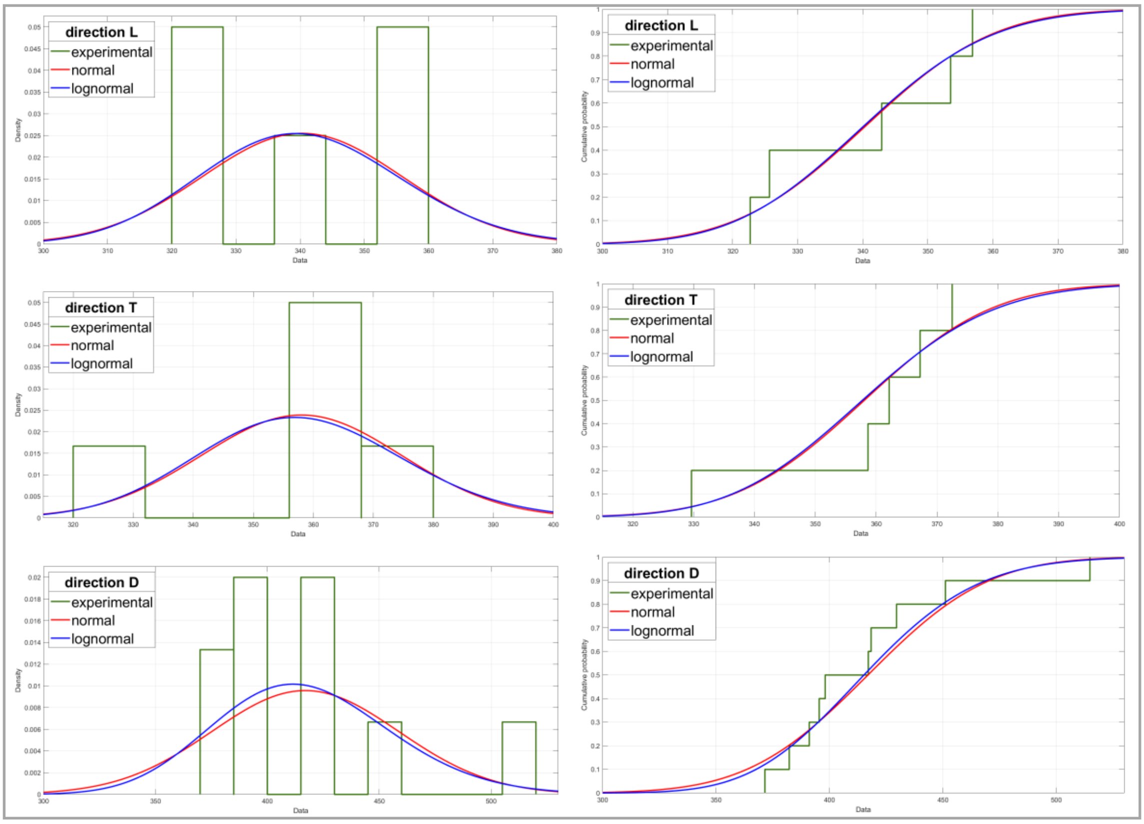

Figure 5.6 – Statistical distributions of 0.2% proof stress $\sigma_{0.2\%}$

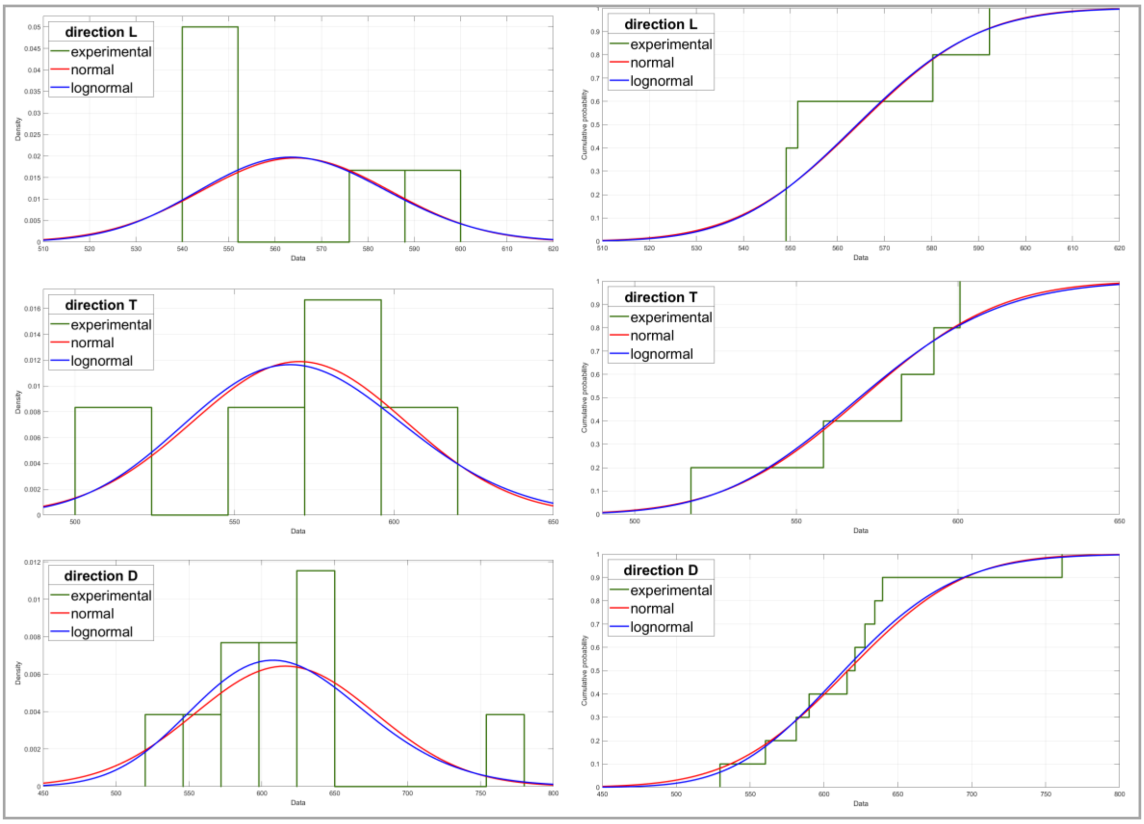

Figure 5.7 – Statistical distributions of ultimate stress σ_u

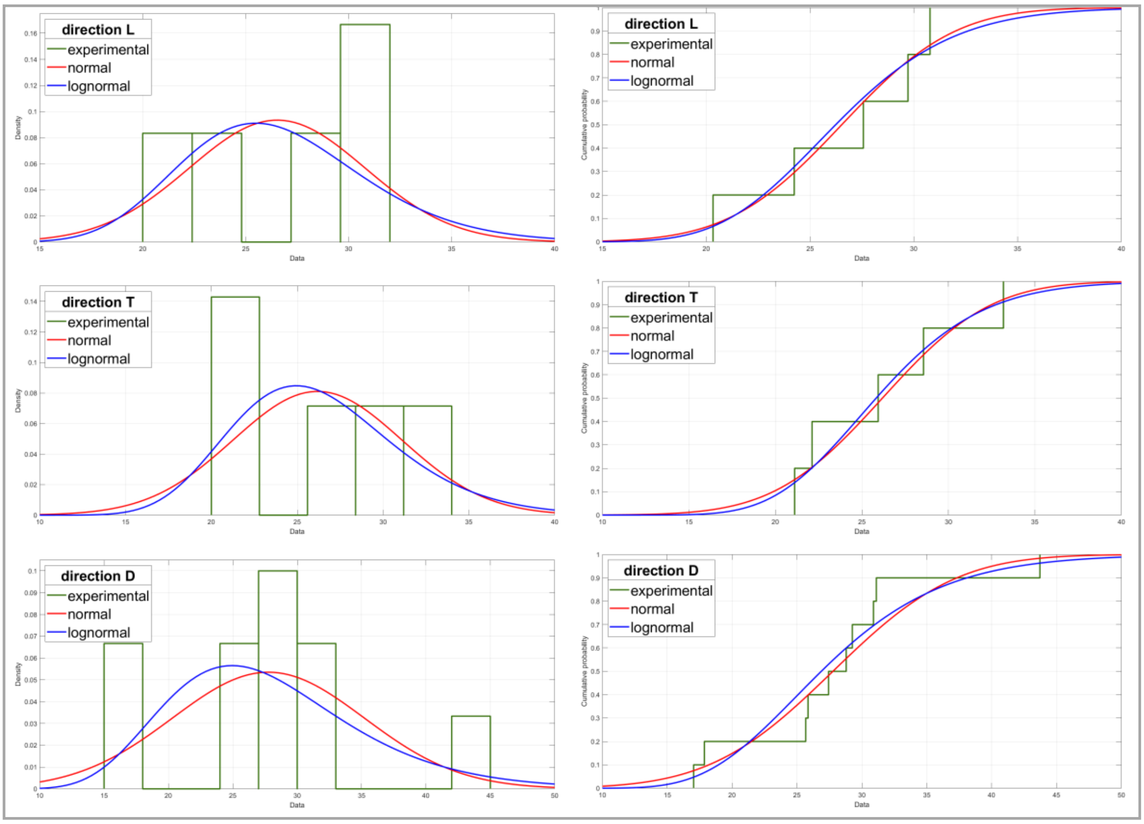

Figure 5.8 – Statistical distributions of ultimate strain ε_u

		Normal			**Lognormal**		
		μ_N	σ_N	V_N	μ_L	σ_L	V_L
E [GPa]	L	138,54	6,31	0,046	138,57	6,30	0,045
	T	113,41	3,07	0,027	113,42	3,07	0,027
	D	247,29	44,71	0,181	247,64	36,50	0,147
$\sigma_{0.01\%}$ [MPa]	L	252,83	37,85	0,150	253,34	37,24	0,147
	T	250,79	41,50	0,165	251,32	39,75	0,158
	D	285,42	76,63	0,268	285,72	69,62	0,244
$\sigma_{0.2\%}$ [MPa]	L	340,33	15,64	0,046	340,41	15,71	0,046
	T	358,03	16,71	0,047	358,12	17,15	0,048
	D	416,97	41,70	0,100	417,10	39,71	0,095
σ_u [MPa]	L	564,47	20,41	0,036	564,54	20,26	0,036
	T	570,32	33,56	0,059	570,54	34,39	0,060
	D	616,05	61,97	0,101	616,27	59,78	0,097
ε_u [%]	L	26,53	4,27	0,161	26,61	4,54	0,171
	T	26,18	4,92	0,188	26,27	4,91	0,187
	D	27,76	7,46	0,269	27,88	7,74	0,278

Table 5.2 – Representative values for best-fit Normal and Lognormal distributions for key mechanical parameters

Kolmogorov-Smirnoff test is run for each parameter, in order to evaluate the "goodness of fit" of the best-fit distributions with respect to the relative experimental data set.

This test evaluates the maximum distance between the best-fit CDF and the empirical one, returning a value for the so-called KS coefficient. For the best-fit distribution to be a valid model for the data set, KS should be smaller than a critical value CV, assessed based on the magnitude of the set's population and the significance level α, which is usually set to 5%, as in the case of the evaluations carried out here.

The results of Kolmogorov-Smirnoff tests are reported in Table 5.3 below. It is evident how both Normal and Lognormal best-fit distributions are valid models for all the considered mechanical parameters in all directions.

			Normal	**Lognormal**
		CV	**KS_N**	**KS_L**
E [GPa]	L	0,5633	0,1379	0,1308
	T	0,5633	0,2450	0,2417
	D	0,4093	0,1869	0,2066
$\sigma_{0.01\%}$ [MPa]	L	0,5633	0,2182	0,1945
	T	0,5633	0,2246	0,1966
	D	0,4093	0,2558	0,2059
$\sigma_{0.2\%}$ [MPa]	L	0,5633	0,2257	0,2254
	T	0,5633	0,3150	0,3221
	D	0,4093	0,1866	0,1707
σ_u [MPa]	L	0,5633	0,3365	0,3358
	T	0,5633	0,2422	0,2465
	D	0,4093	0,2518	0,2326
ε_u [%]	L	0,5633	0,1963	0,2152
	T	0,5633	0,1954	0,1979
	D	0,4093	0,2267	0,2336

Table 5.3 – Kolmogorov-Smirnoff test results for Normal and Lognormal best-fit distributions for key mechanical parameters

5.2.3 Definition of characteristic values

Since both Normal and Lognormal best-fit distributions are good estimators of the data sets provided, characteristic values for the analyzed mechanical parameters can be assessed according to expressions (4.16) and (4.19), respectively.

According to Table 4.4, the value for k_n is equal to 2.33 for a population of 5 (direction L and T), and to 1.92 for 10 samples (direction D), given that V_x is unknown prior.

From Table 5.3, it is possible to appreciate whether the Normal or Lognormal approach is more fitting for each parameter.

Table 5.4 provides the characteristic values obtained following the approach from Annex D corresponding to the most suitable distribution. Said values are presented graphically in Figure 5.9, which also highlights the values for Young's modulus, yielding and ultimate stresses provided by the code for 304L austenitic stainless steel (Table 5.5), to which grade 308LSi stainless-steel wires can be referred to in terms of mechanical behavior.

		distribution	**characteristic value**
E [GPa]	L	Lognormal	135,48
	T	Lognormal	111,88
	D	Normal	184,23
$\sigma_{0.01\%}$ [MPa]	L	Lognormal	235,66
	T	Lognormal	232,29
	D	Lognormal	255,75
$\sigma_{0.2\%}$ [MPa]	L	Lognormal	333,83
	T	Normal	323,22
	D	Normal	402,85
σ_u [MPa]	L	Lognormal	556,78
	T	Normal	500,39
	D	Lognormal	595,89
ε_u [%]	L	Normal	17,62
	T	Normal	14,49
	D	Normal	14,18

Table 5.4 – Characteristic values of key mechanical parameters according to the best fitting distributions

type of stainless steel	**grade**	**E [GPa]**	**f_y [MPa]**	**f_u [MPa]**
Austenitic	1.4301	200	230	540

Table 5.5 – Nominal values of E, f_y and f_u for 304L austenitic stainless-steel [19]

Figure 5.9 – Characteristic values of key mechanical parameters according to the best fitting distributions

The characteristic values of Young's modulus for all three directions are smaller than the nominal one for the traditional material, more significantly so for directions L and T: that for direction L is about 68% of the nominal value, while that for direction T is about 56%. This means that, for the same amount of strain, in the elastic phase the WAAM-produced material reaches lower strains than the conventional material.

Values of 0.2% proof stress, on the contrary, are larger for the 3D-printed material in all considered directions than the nominal value f_y provided for 304L stainless-steel: for L specimens, it is 45% larger than f_y, 40% for T specimens, and 75% for D specimens. Consequently, according to these results, the strain at yielding for the Wire-and-Arc Additively Manufactured material is far larger than that of the traditionally-produced material.
The behavior in terms of ultimate stress is comparable to that of conventional 304L stainless-steel for L specimens, it is about 8% smaller for T specimens and about 10% larger for D specimens.

The characteristic values of 0.01% proof stress are quite similar for the three directions, in the range of 230-255 MPa, with D specimens presenting the largest value and T having the smallest, despite it being larger than the nominal yielding stress value for the conventionally-produced material, nonetheless.
Finally, in terms of ultimate strain, directions T and D present characteristic values that are comparable and are about 80% of that of L specimens.

5.3 Geometrical properties

As mechanical properties were analyzed on milled specimens only, there is the need to characterize the geometry of rough specimens, aiming at the definition of a corrective coefficient φ that carries the influence of geometrical irregularities and that is to be applied to adjust nominal dimensions of elements, which is particularly useful from a design point-of-view.

5.3.1 Experimental results

The analyzed results are taken from a set of 40 specimens, 20 of which oriented along parallelly with respect to the deposition direction (or longitudinal – L) and 20 along the orthogonal direction (or transversal – T). Again, for sake of conciseness, these directions will be referred to as L and T from here onwards.

The nominal dimensions of the specimens are reported in Figure 5.1.

The geometry of the specimens has been characterized only in terms of average effective thickness t_{eff}, as it is the geometrical feature that characterizes the specimens' roughness.

These values have been previously defined by means of volume measurements on an analogic hydraulic scale, exploiting Archimedes' principle. The results obtained from such measurements are reported in Table 5.6, in terms of mean value μ, standard deviation σ and coefficient of variation V.

The same results are provided from a graphical perspective in Figure 5.10, in terms of mean value and standard deviation.

parameter	**direction**	**μ**	**σ**	**V**
t_{eff} [mm]	L	3,890	0,394	0,101
	T	3,948	0,383	0,097

Table 5.6 – Key geometrical parameter from volume-based measurements

From these outcomes, it is apparent how the orientation of the specimens does not significantly influence geometry, in terms of average effective thickness.

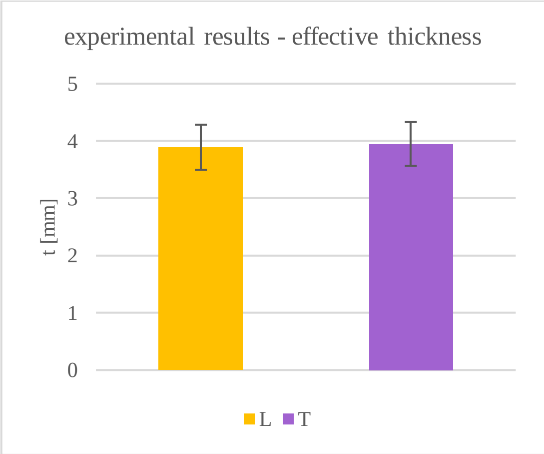

Figure 5.10 – Key geometrical parameter from volume-based measurements

5.3.2 Statistical interpretation of experimental data

As for mechanical parameters, it is necessary to refer the data sets to either a Normal or Lognormal distribution, in order to be able to apply the procedures delineated in Annex D of Eurocode 0 and examined in section 4.3.2 of this dissertation.

Therefore, the aim is to carry out statistical analyses and find the “best-fit” distribution of both parameters in both directions according to maximum-likelihood estimators, assuming Normal and Lognormal distribution models.

Figure 5.11 provides a representation of the relative scaled frequency and the best-fit probability density functions (PDF), as well as the empirical and best-fit cumulative density functions (CDF), for thickness t_{eff}.

Since t_{eff} is characterized by small coefficients of variation, it is to be expected that Normal and Lognormal best-fit distributions are graphically almost overlapped.

Practically, numerical results in terms of mean values, standard deviations and coefficients of variation are reported in Table 5.7.

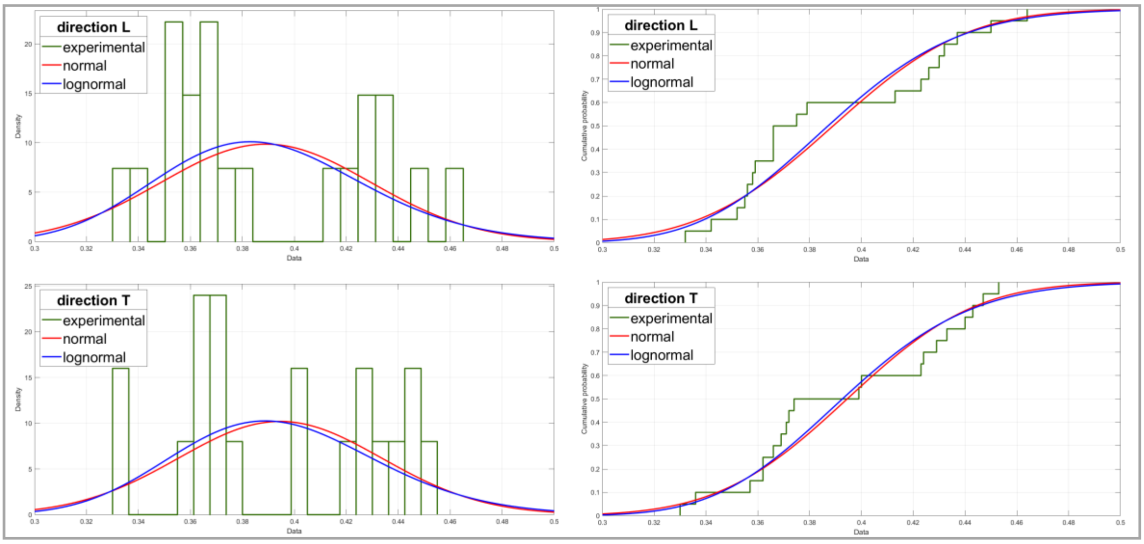

Figure 5.11 – Statistical distributions of average effective thickness t_{eff}

		Normal			Lognormal		
		μ_N	**σ_N**	**V_N**	**μ_L**	**σ_L**	**V_L**
t_{eff} [mm]	L	3,891	0,405	0,104	3,891	0,400	0,103
	T	3,945	0,391	0,099	3,946	0,394	0,100

Table 5.7 – Representative values for best-fit Normal and Lognormal distributions for key geometrical parameters

The best-fit Normal and Lognormal distributions for each parameter and each direction are evaluated in terms of "goodness of fit" by means of Kolmogorov-Smirnoff test.

The results of these tests are reported in Table 5.8, in terms of KS coefficient as well as critical value CV for a significance level α of 0.05. Both Normal and Lognormal best-fit distributions provide a suitable model for the considered geometrical properties in both directions.

			Normal	Lognormal
		CV	**KS_N**	**KS_L**
t_{eff} [mm]	L	0,2941	0,2156	0,2077
	T	0,2941	0,2000	0,1876

Table 5.8 – Kolmogorov-Smirnoff test results for Normal and Lognormal best-fit distributions for key geometrical parameter

5.3.3 Definition of characteristic values

Taking the best-fit Lognormal distribution as the most suitable one for both data sets, the characteristic values for t_{eff} are assessed according to expression (4.19).

According to Table 4.4, the value for k_n for a set of 20 specimens is equal to 1,76, which is valid for both L and T directions, as the coefficients of variation of the parameters are not known beforehand.

Table 5.9 provides the characteristic values obtained following the approach from Annex D corresponding to the Lognormal distribution, hence according to (4.19). Said values are presented graphically in Figure 5.12, which also highlights the nominal value of the thickness of the specimens represented in Figure 5.1, which is listed in Table 5.10.

		distribution	characteristic value
t_{eff} [mm]	L	Lognormal	3,39
	T	Lognormal	3,45

Table 5.9 – Characteristic values of key geometrical parameter according to the best fitting distributions

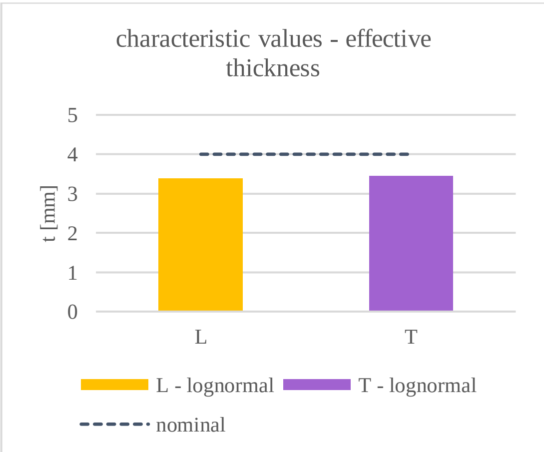

Figure 5.12 – Characteristic values of key geometrical parameter according to the best fitting distributions

type of specimen	t_{nom} [mm]	A_{avg} [mm^2]
"Dog-bone"	4,0	97,02

Table 5.10 – Nominal values of test specimens' dimensions [18]

5.3.4 *Definition of the geometrical corrective factor φ*

Figure 5.12 provides an evaluation of the effective values of thickness, and their comparison to the nominal ones. It is clear how for both directions considered, the effective value is lower than the nominal one.

One of the aims of this study is to quantify a corrective factor φ that can be related to the nominal dimensions of a structural element, so that the geometrical imperfections that inherently characterize the 3D-printing process are taken into account at the design stage, without having to produce specimens and perform any further hand-measurements or comprehensive 3-dimensional scans.

In order to do this, corrective factor φ is defined as the ratio between the values previously obtained and indicated in Table 5.9 and the respective nominal one, according to Table 5.10. Table 5.11 reports the values of φ that have computed as just indicated. As L and T specimens provide results that are quite similar to each other, it is fair to evaluate φ as an average of the results obtained for each direction separately.

		nominal values	**effective values**	**φ [-]**	**φ_{avg} [-]**
t [mm]	L	4,00	3,39	0,847	0,855
	T	4,00	3,45	0,862	

Table 5.11 – Assessment of geometrical corrective factor φ

6. Resistance function

6.1 Overview

The scope of this chapter is to calibrate partial safety factors that are already defined in the existing Code [19]. This is achieved by means of the procedure outlined in Annex D [1], and further explained in section 4.3.3, and by exploiting the characteristic values obtained in section 5.2 for mechanical properties, and more specifically yielding and ultimate strengths, and in section 5.3 for geometrical properties, namely the geometrical corrective coefficient φ.

The procedure thoroughly described in section 4.3.3 is used to define the design resistance function r_d, while the characteristic resistance function r_k is defined by means of the single properties' characteristic values, defined in chapter 5. Finally, as per its definition, the safety factor is defined as the ratio between characteristic and design values of the resistance function; following, overall, a similar approach to that carried out in [17].

This method is carried out for both yielding and ultimate resistances, in order to properly calibrate the respective partial safety factors. Furthermore, both are evaluated for directions L and T: separately, as to give more precise results that could be needed for more specific and accurate design applications, as well as together, in order to provide a value that is independent on the orientation.
The analyzed population is comprised of 16 specimens oriented in the longitudinal direction (L) and 16 in the transversal direction (T), all of which present a rough surface, namely they have not been subjected to any milling, and a nominal geometry that is shown in Figure 5.1.

6.2 Procedure

The procedure followed for the definition of design and characteristic resistance functions, and, therefore, calibrate the partial safety factors, is delineated hereafter:

1. Development of the design model: the theoretical resistance function r_t is defined as a function of basic variables $\underline{X}$;
2. Comparison between experimental and theoretical values: for each specimen i, the experimental resistance function r_{ei} is provided by the outcomes of laboratory testing, while r_{ti} is computed according to the defined model;
3. Estimation of correction factor b: b is defined and computed according to equation (4.25);
4. Estimation of the CoV of the error: V_δ, obtained through expression (4.31), represents the scatteredness due to the model defined in step 1;
5. Analysis of compatibility: it is necessary to verify whether the test population is compatible with the model, namely if the variability of the model is small enough;
6. Definition of the CoV of the basic variables: the coefficients of variation for each basic variable are computed, and then properly combined into V_{rt}, which is representative of the scatteredness of the results given by the basic variables, according to equation (4.32);
7. Definition of the design resistance function: r_d is computed according to either expression (4.42) or (4.43);
8. Definition of the characteristic resistance function: following a similar approach to that introduced in [17], r_k is defined through the reference characteristic values of the basic variables, as obtained in chapter 5;
9. Computation of the partial safety factor: γ^*_M is defined according to its definition, i.e. as the ratio between characteristic and design values of the resistance function;
10. Definition of the corrective factor: in order to maintain the values of the partial safety factor defined in the codes, and specifically in [19] for stainless-steel, that obtained in step 9 is scaled by means of a corrective factor η^*.

6.3 Problem formulation

Before performing evaluations and calculations, the problem must be adequately formulated.
In general, the tensile resistance is defined as:

$$R_i = A_{eff,i} f_i \eta \quad (6.1)$$

where:

$A_{eff,i}$ is the effective cross-sectional aera of element i, characterized by a certain statistical distribution

f_i is the strength of the material of element i, also characterized by a statistical distribution

η is the uncertainty associated to the model

One crucial aspect in the definition of the resistance function, according to Annex D of EC0 [1], is that the basic variables should be independent on each other.
For this reason, it is not possible to define both strengths and effective cross-sectional areas as basic variables, since, from experimental data, strengths are defined through the value of A_{eff}, namely:

$$f_i = \frac{F_i}{A_{eff,i}} \quad (6.2)$$

where:

F_i is the reaction force recorded for specimen i in correspondence of the target strength, be it yielding or ultimate

As the geometrical characterization can only be done on rough specimens, while mechanical properties can be extracted from milled ones, the value for the strength (yielding or ultimate) for the definition of the theoretical resistance function for each specimen i will be taken as the average value for milled specimens, as indicated in Table 5.1.

According to this reasoning, the only basic variable in the definition of the resistance function is the effective cross-sectional area, and, more specifically, geometrical corrective factor φ.
This way, the influence of the roughness on the resistance will be highlighted, while strengths are totally independent on any geometrical irregularity, as they are defined for machined specimens.

6.4 Yielding resistance

As defined in the previous paragraph, the first step to carry out is the definition of the theoretical resistance function. It is defined as:

$$r_t = \varphi A_n f_y \tag{6.3}$$

where:

φ is the geometrical corrective factor, as defined in section 5.3.4, namely

$$\varphi = \frac{t_{eff}}{t_{nom}} \tag{6.4}$$

A_n is the nominal cross-sectional area referred to the gauge length; hence, recalling Figure 5.1, it is equal to 80 mm^2

f_y is the yielding strength or 0.2% proof stress from milled specimens

Therefore the basic variable for the so-defined resistance function are the geometrical corrective factor φ and the yielding strength f_y.

6.4.1 Longitudinal direction

In Table 6.1 are reported all the values for basic variable φ obtained from the tested specimens, the relative values of r_{ti} computed according to expression (6.3), as well as the mean value of f_y obtained for milled specimens, and the values of the reaction forces reached at yielding by each specimen, which correspond to the experimental resistance function r_{ei}.

In order not to bias the results, the value of the nominal area for the computation of r_{ti} for each specimen is evaluated as:

$$A_{ni} = t_n L_i \tag{6.5}$$

where:

t_n is the nominal thickness of the specimens (4 mm)

L_i is the width of the specimen referred to the gauge length

This specification is made because the value of L_i does not depend on the production of the material, but rather on how precisely the specimen were cut out of the printed plates, while the focus is on the roughness of the WAAM-produced material, and hence any variability should be solely related to the effective thickness.

Ideally, if the theoretical resistance function were exact and complete, all (r_{ti},r_{ei}) points would lie on the line for which r_e=r_t. As this does not find correspondence within reality, the point will present some scatter with respect to said line, as can be seen in Figure 6.1.

	theoretical				experimental
specimen	**φ [-]**	**L [mm]**	**$\sigma_{0.2\%}$ [MPa]**	**r_{ti} [kN]**	**r_{ei} [kN]**
1A	0,889	19,8	340,33	23,97	24,96
1bisA	0,829	20,0	340,33	22,57	25,09
1B	0,915	20,0	340,33	24,91	23,62
1bisB	0,886	20,8	340,33	25,09	25,28
2A	0,899	20,0	340,33	24,46	25,47
2bisA	0,879	19,5	340,33	23,35	26,67
2B	0,948	20,4	340,33	26,33	23,87
2bisB	0,915	20,0	340,33	24,90	24,23
4A	1,125	28,2	340,33	43,18	39,27
4bisA	1,091	22,6	340,33	33,58	38,39
4B	1,159	22,6	340,33	35,67	31,05
4bisB	1,032	27,6	340,33	38,79	35,72
5A	1,080	27,6	340,33	40,57	38,02
5bisA	1,057	27,6	340,33	39,72	35,67
5B	1,064	30,0	340,33	43,45	39,52
5bisB	1,075	25,3	340,33	37,03	33,04

Table 6.1 – Values of r_{ti} and r_{ei} for L specimens at yielding

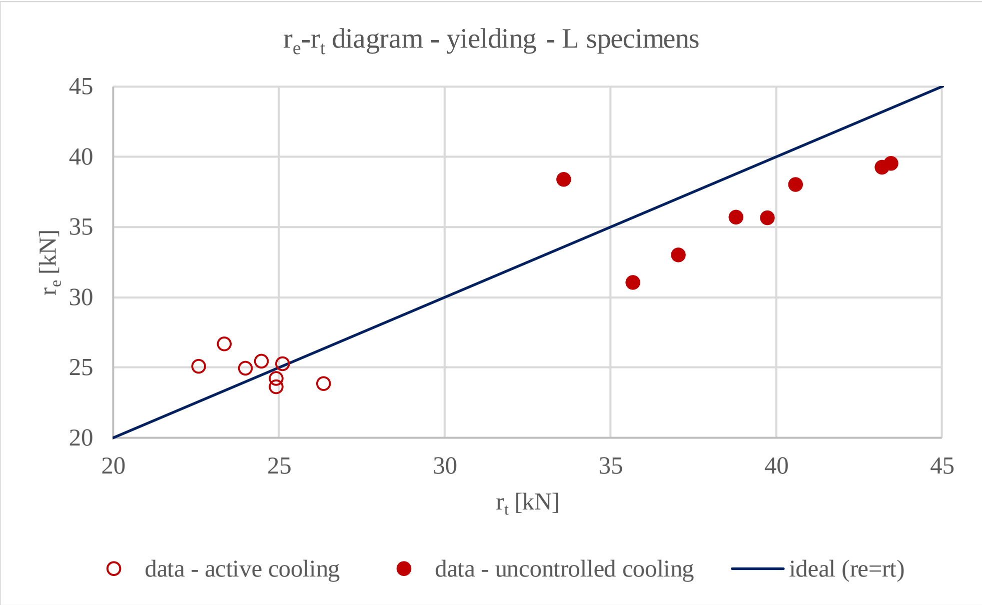

Figure 6.1 – r_e-r_t diagram for L specimens at yielding

The theoretical and experimental values of the resistance function are related by means of the corrective factor b, which is defined as the "Least Squares" best fit to the slope, according to expression (4.25), resulting in b = 0,953. This result is reported in Figure 6.2, where it is evident how it almost coincides with the ideal line.

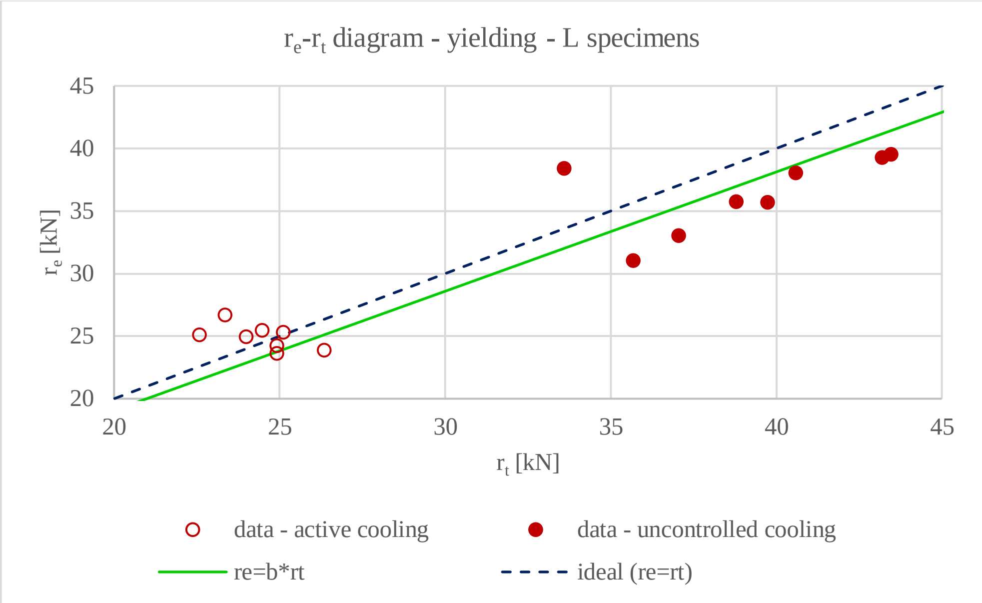

Figure 6.2 – r_e-r_t diagram for L specimens at yielding, with best-fit slope (b=0,953)

The error carried by the model for each specimen i, according to the problem formulation described in section 6.3, is directly related to the influence of the repeatability of the roughness among specimens.

Numerically, it is evaluated according to expression (4.27), and then evaluated in lognormal terms, as expressed by (4.28): these results are reported in Table 6.2.

The mean value and the variance of the error in lognormal terms are then defined through equations (4.29) and (4.30), respectively. Finally, the coefficient of variation is evaluated by exploiting expression (4.31), representing the scatteredness given by the model, defined as indicated in (6.3).

The coefficient of variation of the error is, in this case, V_δ = 0,092.

In order to build the resistance function, some assumptions have been made, and it is necessary to check whether the test population is compatible with the model.

The scatteredness of the (r_{ti},r_{ei}) values is represented by the value of V_δ. Due to the intrinsic uncertainties that characterize the WAAM process and the scarce repeatability of the available data, it is fair to assume that coefficients of variation related to the model are valid up to 10%.

Therefore, being V_δ = 0,092, considering the assumption above, the compatibility is checked.

specimen	δ [-]	Δ [-]
1A	1,093	0,088
1bisA	1,166	0,154
1B	0,995	-0,005
1bisB	1,057	0,055
2A	1,092	0,088
2bisA	1,199	0,181
2B	0,951	-0,050
2bisB	1,021	0,021
4A	0,954	-0,047
4bisA	1,200	0,182
4B	0,913	-0,091
4bisB	0,966	-0,034
5A	0,983	-0,017
5bisA	0,942	-0,059
5B	0,954	-0,047
5bisB	0,936	-0,066

Table 6.2 – Values of δ_i and Δ_i for L specimens at yielding

As there is only one basic variable defining the resistance function, the overall scatteredness related to basic variables V_{rt} is simply:

$$V_{rt} = V_\varphi \tag{6.6}$$

After evaluating the mean m and the standard deviation s for geometrical corrective coefficient φ, its coefficients of variation is, by definition, computed as the ratio between s and m, resulting in V_φ = 0,102.

The overall scatteredness V_r is given by both V_δ and V_{rt}, and it is obtained through expression (4.34), hence:

$$V_r = \sqrt{(V_{rt}^2 + 1)(V_\delta^2 + 1) - 1} \tag{6.7}$$

The global scatteredness given by the model and the basic variables is V_r = 0,138.

Standard deviations V_δ, V_{rt} and V_r can be expressed in lognormal terms, by means of equations (4.35), (4.36) and (4.37), respectively.

Q_δ and Q_{rt} can then be normalized with respect to Q, according to expressions (4.40) and (4.39), correspondingly.

The mean value of the theoretical function r_{tm} is computed, as indicated in (6.8), as the resistance function evaluated for the mean value of the basic variable (m_{φ} = 0,990), resulting in r_{tm} = 26,96 kN.

$$r_{tm} = m_{\varphi} A_n f_y \tag{6.8}$$

In order to compute the value of the design resistance function r_d, according to expression (4.42), the value of $k_{n,d}$ must be defined based on Table 4.5: as the number of specimens analyzed is 16, $k_{16,d}$ is evaluated by means of linear interpolation, and it is equal to 3,988.
The resulting value for the design resistance function is r_d = 15,84 kN.

The characteristic value of the resistance function r_k is evaluated as:

$$r_k = \varphi_k A_n f_{yk} \tag{6.9}$$

where:

φ_k = 0,855	as computed in section 5.3.4
A_n = 80,00 mm^2	according to Figure 5.1
f_{yk} = 333,8 MPa	as computed in section 5.2.3 for L specimens

The computed value for the characteristic resistance function is r_k = 22,83 kN.
In general, the partial safety factor γ^*_M is computed as:

$$\gamma_M^* = \frac{r_k}{r_d} \tag{6.10}$$

According to [19], the partial factor for the resistance of cross-sections to excessive yielding is γ_{M0} = 1,10.

In general, the design tensile resistance at yielding is evaluated as:

$$R_{yd} = \frac{1}{\gamma_{M0}} A_{eff} f_{yk} \tag{6.11}$$

In order for the partial safety factor to remain the same as those found in the code [19] (in general, γ_M), a coefficient α^* is introduced to account for the computed γ^*_M as:

$$\alpha^* = \frac{\gamma_M}{\gamma_M^*} \tag{6.12}$$

Being γ^*_{M0} = 1,442, α^*_0 = 0,76.

Furthermore, as the effective cross-sectional area A_{eff} is defined through the nominal value A_n by means of the geometrical corrective factor φ_k, as expressed in equation (6.13), the design tensile resistance at yielding R_{yd} can be formulated as reported in expression (6.14).

$$A_{eff} = \varphi_k A_n \tag{6.13}$$

$$R_{yd} = \left(\alpha_0^* \frac{1}{\gamma_{M0}}\right)(\varphi_k A_n) f_{yk} \tag{6.14}$$

Finally, corrective factor η* is defined accounting both for coefficient α*, which calibrates the partial safety factor, and for coefficient φ_k, which corrects the nominal value of the cross-sectional area, and is the same in both L and T directions; namely:

$$\eta^* = \alpha^* \varphi_k \tag{6.15}$$

The resulting corrective factor is $\eta^*_0 = 0{,}65$.

Therefore, R_{yd} can be expressed as:

$$R_{yd} = \eta_0^* \left(\frac{1}{\gamma_{M0}} A_n f_{yk}\right) \tag{6.16}$$

All the numerical data and results obtained for the evaluation of the resistance of L specimens at yielding, following the procedure described in section 6.2, are reported in Table 6.3 below.

step		parameter	value	unit
step 3	correction factor b	b	0,953	-
step 4	CoV of the error V_δ	$\overline{\Delta}$	0,022	-
		s_Δ^2	0,008	-
		V_δ	0,092	-
step 6	CoV of basic variables V_{rt}	m_φ	0,990	-
		s_φ	0,101	-
		V_φ	0,102	-
		V_{rt}	0,102	-
step 7	design resistance r_d	V_r	0,138	-
		Q_δ	0,091	-
		Q_{rt}	0,102	-
		Q	0,137	-
		α_δ	0,667	-
		α_{rt}	0,745	-
		r_{tm}	26,96	kN
		r_d	15,84	kN
step 8	characteristic resistance r_k	φ_k	0,855	-
		A_n	80,00	mm^2
		f_{yk}	333,8	MPa
		r_k	22,83	kN
step 9	partial safety factor γ^*_M	γ^*_{M0}	1,442	-
step 10	corrective factor η^*	α^*_0	0,76	-
		η^*_0	0,65	-

Table 6.3 – Data and results for the yielding resistance of L specimens

6.4.2 Transversal direction

Following the same approach used for the L direction, in Table 6.4 are reported the value of basic variable φ from the tested as-built T specimens, the mean value of $\sigma_{0.2\%}$ from milled T specimens (Table 5.1), and the values of r_{ti} computed according to expression (6.3), as well as the values of the reaction force reached at yielding by each specimen during testing, which correspond to r_{ei}.

	theoretical				**experimental**
specimen	**φ [-]**	**L [mm]**	**$\sigma_{0.2\%}$ [MPa]**	**r_{ti} [kN]**	**r_{ei} [kN]**
1C	0,999	20,1	358,03	28,75	24,41
1bisC	0,998	20,4	358,03	29,15	24,24
1D	0,914	20,0	358,03	26,18	25,86
1bisD	0,905	19,9	358,03	25,78	24,21
2C	0,906	19,5	358,03	25,29	23,97
2bisC	0,928	20,0	358,03	26,58	24,93
2D	0,936	19,6	358,03	26,28	24,22
2bisD	0,930	20,2	358,03	26,92	23,07
4C	1,081	22,8	358,03	35,31	30,32
4bisC	1,072	26,6	358,03	40,85	34,69
4D	1,141	22,7	358,03	37,09	28,33
4Dbis	1,107	26,0	358,03	41,22	33,92
5C	1,100	29,4	358,03	46,33	38,14
5bisC	1,118	25,4	358,03	40,68	31,95
5D	1,061	30,5	358,03	46,34	39,94
5bisD	1,058	27,5	358,03	41,68	35,13

Table 6.4 – Values of r_{ti} and r_{ei} for T specimens at yielding

All (r_{ti},r_{ei}) values are plotted in Figure 6.3, where also the ideal line along which the points would lie if the theoretical resistance function were exact and complete is represented, as well as the line characterized by correction factor b, computed according to expression (4.25): b = 0,851.

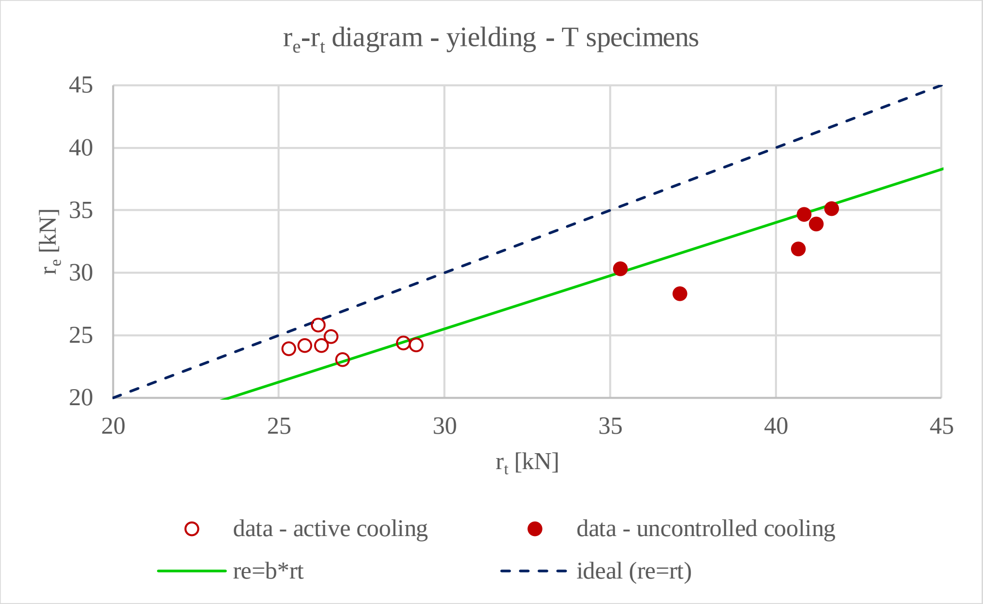

Figure 6.3 – r_e-r_t diagram for T specimens at yielding, with best-fit slope (b=0,851)

Table 6.5 reports the values of the error related to the model for each specimen δ_i, evaluated by means of expression (4.27), also in lognormal terms, i.e. Δ_i, according to (4.28).

specimen	**δ [-]**	**Δ [-]**
1C	0,998	-0,002
1bisC	0,978	-0,022
1D	1,161	0,149
1bisD	1,104	0,099
2C	1,114	0,108
2bisC	1,103	0,098
2D	1,084	0,080
2bisD	1,008	0,008
4C	1,010	0,010
4bisC	0,998	-0,002
4D	0,898	-0,107
4Dbis	0,967	-0,033
5C	0,968	-0,033
5bisC	0,923	-0,080
5D	1,013	0,013
5bisD	0,991	-0,009

Table 6.5 – Values of δ_i and Δ_i for T specimens at yielding

The mean value and the variance of the error in lognormal terms can be then defined using equations (4.29) and (4.30), respectively. Finally, the coefficient of variation of the error V_δ is computed through expression (4.31), which is representative of the scatteredness given by the model, defined as (6.3). Therefore, $V_\delta = 0{,}071$.
The compatibility of the test population with the model is evaluated considering a valid maximum level of scatteredness of 10%, for which V_δ is verified.

The coefficients of variation for the basic variable, i.e. the geometrical corrective factor is $V_\varphi = 0{,}082$; hence. according to equation (6.6), $V_{rt} = 0{,}082$.

The overall scatteredness, according to (6.7), is $V_r = 0{,}108$.
V_δ, V_{rt} and V_r are expressed in lognormal terms as Q_δ, Q_{rt} and Q, respectively, following equations (4.35), (4.36) and (4.37); Q_δ and Q_{rt} are then normalized with respect to Q as α_δ and α_{rt}, correspondingly.
The mean value of the theoretical function r_{tm} is computed as (6.8), where $m_\varphi = 1{,}016$, resulting in $r_{tm} = 29{,}10$ kN.
Finally, with $k_{n,d} = 3{,}988$, the design value of the resistance function, according to expression (4.42), is $r_d = 16{,}94$ kN.

The characteristic value of the resistance function r_k is evaluated as (6.9), with $\varphi_k = 0{,}855$ (section 5.3.4), $A_n = 80$ mm^2 (Figure 5.1) and $f_{yk} = 323{,}2$ MPa (section 5.2.3), resulting in $r_k = 22{,}11$ kN.
Consequently, following expression (6.10), $\gamma^*_{M0} = 1{,}305$; subsequentially, as $\gamma_{M0} = 1{,}10$ and according to (6.12), $\alpha^*_0 = 0{,}84$.
Finally, the corrective factor accounting for the calibration of the partial safety factor and of the geometry of the element, as stated in expression (6.15), $\eta^*_0 = 0{,}72$.

Table 6.6 reports all data and results obtained for the evaluation of the resistance of T specimens at yielding.

step		parameter	value	unit
step 3	correction factor b	b	0,851	-
step 4	CoV of the error V_δ	$\overline{\Delta}$	0,017	-
		s_Δ^2	0,005	-
		V_δ	0,071	-
step 6	CoV of basic variables V_{rt}	m_φ	1,016	-
		s_φ	0,083	-
		V_φ	0,082	-
		V_{rt}	0,082	-
step 7	design resistance r_d	V_r	0,108	-
		Q_δ	0,071	-
		Q_{rt}	0,081	-
		Q	0,108	-
		α_δ	0,658	-
		α_{rt}	0,753	-
		r_{tm}	29,10	kN
		r_d	16,94	kN
step 8	characteristic resistance r_k	φ_k	0,855	-
		A_n	80,00	mm^2
		f_{yk}	323,2	MPa
		r_k	22,11	kN
step 9	partial safety factor γ^*_M	γ^*_{M0}	1,305	-
step 10	corrective factor η^*	α^*_0	0,84	-
		η^*_0	0,72	-

Table 6.6 – Data and results for the yielding resistance of T specimens

6.4.3 Both directions (L and T)

In addition to analyzing L and T specimens separately, it is useful to evaluate both directions together, in order to provide a value for the corrective coefficient η^* that is independent on the orientation of the applied load with respect to that of the layer deposition.

The approach followed is that explicated in section 6.2, as it was for the evaluation carried out for L and T specimens separately.

The data provided in Table 6.1 and Table 6.4 must be revised, taking as $f_{y,avg}$ = 349,18 MPa, i.e. as the average between the mean value for milled L specimens and that for milled T ones.

Corrective factor b can then be computed according to expression (4.25), hence b = 0,900; this result is reported graphically in Figure 6.4.

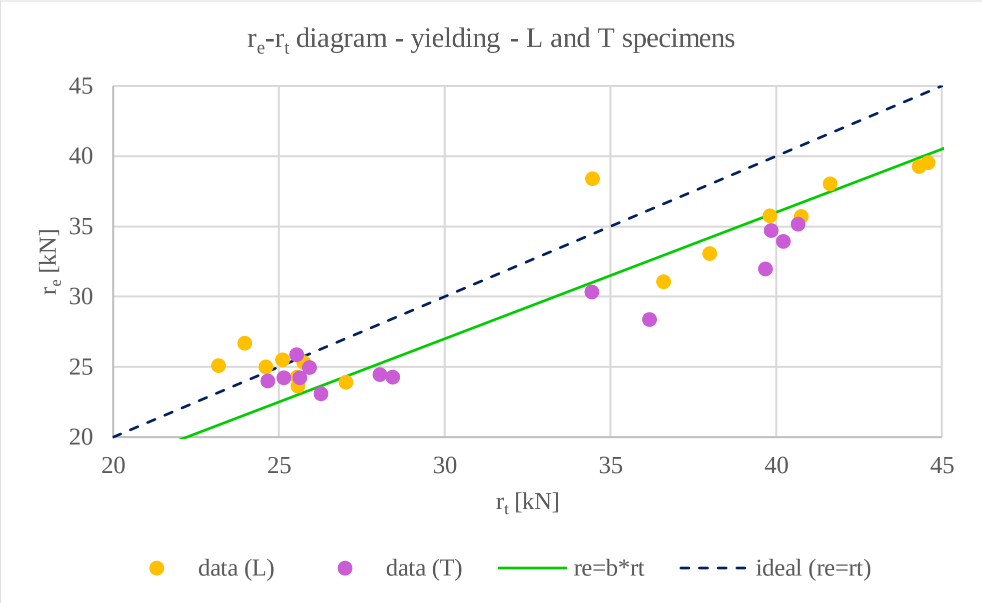

Figure 6.4 – r_e-r_t diagram for both L and T specimens at yielding, with best-fit slope (b=0,900)

The scatteredness provided by the defined model is quantified as expressed in (4.31), resulting in V_δ = 0,088. Instead, that carried by the basic variable is V_{rt} = 0,093, following equation (6.6), as the coefficient of variation for the geometrical corrective factor is V_φ = 0,093.

The overall scatteredness is evaluated according to expression (6.7) and is V_r = 0,128.

The compatibility of the data set with the model is assessed setting a maximum value for V_δ of 10%, hence the population can be considered compatible with the model.

Evaluating Q_δ, Q_{rt} and Q, respectively, following equations (4.35), (4.36) and (4.37), and consequently α_δ and α_{rt}, as correspondingly stated in (4.40) and (4.39), and knowing that r_{tm} = 28,02 kN according to (6.8), where m_φ = 1,003, allows for the computation of the design value of the resistance function as r_d = 16,96 kN, following expression (4.43).

As T specimens present a lower value of the 0.2% proof stress, the value of f_{yk} is set accordingly equal to 323,2 MPa, while A_n = 80 mm^2 and φ_k = 0,855; consequently r_k = 22,11 kN as for T specimens only.

The partial safety factor computed according to (6.10) is γ^*_{M0} = 1,303; therefore, the calibrating factor α^*_0 is equal to 0,84, evaluated as indicated in expression (6.12).
Finally, α^*_0 is combined with the geometrical corrective factor φ_k according to equation (6.15), and the resulting corrective factor is η^*_0 = 0,72.

All data, computations and results involved in the evaluation of the corrective factor η^*_0, needed in order to express the design resistance at yielding as (6.16) are reported in Table 6.7.

step		parameter	value	unit
step 3	correction factor b	b	0,900	-
step 4	CoV of the error V_δ	$\overline{\Delta}$	0,020	-
		s_Δ^2	0,008	-
		V_δ	0,088	-
step 6	CoV of basic variables V_{rt}	m_φ	1,003	-
		s_φ	0,094	-
		V_φ	0,093	-
		V_{rt}	0,093	-
step 7	design resistance r_d	V_r	0,128	-
		Q_δ	0,088	-
		Q_{rt}	0,093	-
		Q	0,128	-
		α_δ	0,686	-
		α_{rt}	0,728	-
		r_{tm}	28,02	kN
		r_d	16,96	kN
step 8	characteristic resistance r_k	φ_k	0,855	-
		A_n	80,00	mm^2
		f_{yk}	323,2	MPa
		r_k	22,11	kN
step 9	partial safety factor γ^*_M	γ^*_{M0}	1,303	-
step 10	corrective factor η^*	α^*_0	0,84	-
		η^*_0	0,72	-

Table 6.7 – Data and results for the yielding resistance of both L and T specimens

6.4.4 *Results*

In Table 6.8 below are reported all significant values obtained following the procedure explicated in section 6.2, for L and T specimens, both separately and combined.

parameter	**direction L**	**direction T**	**directions L and T**	**units**
b	0,953	0,851	0,900	-
V_δ	0,092	0,071	0,088	-
V_{rt}	0,102	0,082	0,093	-
V_r	0,138	0,108	0,128	-
r_d	15,84	16,94	16,96	kN
r_k	22,83	22,11	22,11	kN
γ^*_{M0}	1,442	1,305	1,303	-
α^*_0	0,76	0,84	0,84	-
η^*_0	0,65	0,72	0,72	-

Table 6.8 – Summary of results for yielding resistance

Scatteredness V_δ, characterizing the model only, is 7-9%, in general; T specimens, in particular resent a smaller variability.

Regarding basic variable φ, hence in terms of V_{rt}, T specimens present the smallest value, which means that the experimental values for φ carry a lower level of dispersion with respect to their mean; on the contrary, L presents the largest value of V_{rt}.

Regarding the ratio between the traditional value of the partial safety factor γ_{M0} = 1,1 and that computed according to (6.10), i.e. α^*_0, Table 6.8 shows that γ_{M0} is about 76 to 84% of the computed one, γ^*_{M0}. In other words, the traditional value must be increased of about 19 to 32%.

Recalling equation (6.16):

$$R_{yd} = \eta_0^* \left(\frac{1}{\gamma_{M0}} A_n f_{yk}\right)$$

The main result obtained from the procedure carried out throughout this chapter is, therefore, the corrective factor η^*_0.

This coefficient, in fact, allows to maintain the standard formulation of the design resistance at yielding, and calibrates it in order to account for the peculiarities of the 3D-printed material, in particular the roughness of the as-built element, and any other imperfection that could not be accounted for in previous evaluations and calibrations, such as those carried out in chapter 5.

Focusing on the corrective factor η^*_0, Table 6.8 shows that the value for L specimens is lower than for the other two cases.
This difference in the final result is partly due the fact that L specimens are characterized by a higher value of f_{yk} and, therefore of r_k; at the same time, the value of r_d is quite smaller than for the other cases, and this can be associated to the fact that the overall scatteredness is larger for direction L than for T or for the two orientations combined.
This effect on the evaluation of η^*_0 is somehow decreased for the two directions combined, even though the value of V_r is closer to that for L specimens, due to the fact that r_k is evaluated according to direction T, hence is smaller than that for L.

As the values of V_δ are dependent on the geometrical irregularities, based on the way the problem is defined (section 6.3), as well as, by definition, in V_r, the overall scatteredness can be intended as a measure of the influence of the repeatability of the cross-sectional area.

For this reason, moving forward into the development of this technology for the construction industry, one of the main objectives is for companies that produce Wire-and-Arc Additively Manufactured elements to be able to guarantee a certain level of variability in terms of roughness. This way, from a design point-of-view, there can be a generalized approach for the characterization of the design resistance by means of a corrective factor η^*_0.

6.5 Ultimate resistance

As for the resistance at yielding, for the ultimate resistance, the procedure outlined in section 6.2 is carried out in order to obtain a corrective factor η^*_2 that calibrates the traditional partial safety factor for the resistance of cross-sections in tension to fracture γ_{M2}, which, according to [19], is equal to 1,25.

Similarly to the case at yielding analyzed in section 6.4, the theoretical resistance function is defined as:

$$r_t = \varphi A_n f_t \tag{6.17}$$

where:

- φ is the geometrical corrective factor, defined as (6.4)
- A_n is the nominal cross-sectional area referred to the gauge length; hence, referring to Figure 5.1, it is equal to 80 mm^2
- f_t is the ultimate strength, hence the maximum bearable stress

Consequently, the basic variables for the so-defined resistance function are the geometrical corrective factor φ and the ultimate strength f_t.

Table 6.9 reports the values of basic variable φ for each of the tested longitudinal specimen, the mean value of f_t for milled L specimens, the relative values of r_{ti} (computed according to expression (6.17), where the value of A_n for each specimen is evaluated as (6.5)), and the values of the maximum reaction forces reached by each specimen, which correspond to the experimental resistance function r_{ei}.

All (r_{ti},r_{ei}) values are plotted in Figure 6.5. Said graph reports the ideal line r_e=r_t, as well as the line characterized by the best-fit slope b, computed as (4.25): b = 1,007.

specimen	theoretical				experimental
	φ [-]	**L [mm]**	**σ_u [MPa]**	**r_{ti} [kN]**	**r_{ei} [kN]**
1A	0,889	19,8	564,47	39,76	40,59
1bisA	0,829	20,0	564,47	37,44	39,84
1B	0,915	20,0	564,47	41,31	38,46
1bisB	0,886	20,8	564,47	41,62	39,87
2A	0,899	20,0	564,47	40,58	40,41
2bisA	0,879	19,5	564,47	38,72	40,56
2B	0,948	20,4	564,47	43,67	37,68
2bisB	0,915	20,0	564,47	41,31	38,65
4A	1,125	28,2	564,47	71,62	72,12
4bisA	1,091	22,6	564,47	55,70	68,24
4B	1,159	22,6	564,47	59,16	56,87
4bisB	1,032	27,6	564,47	64,34	64,02
5A	1,080	27,6	564,47	67,29	67,89
5bisA	1,057	27,6	564,47	65,88	65,90
5B	1,064	30,0	564,47	72,07	72,87
5bisB	1,075	25,3	564,47	61,43	61,92

Table 6.9 – Values of r_{ti} and r_{ei} for L specimens at the ultimate state

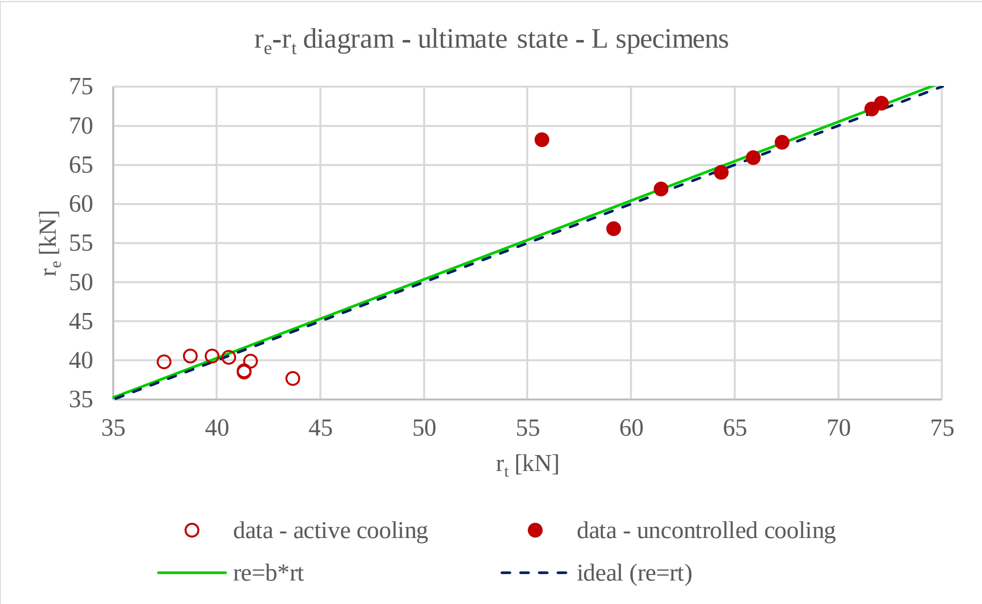

Figure 6.5 – r_e-r_t diagram for L specimens at the ultimate state, with best-fit slope (b=1,007)

The definition of the model unavoidably carries some error, which can be computed for each specimen according to expression (4.27). Through the evaluation of said error in lognormal terms, as expressed in (4.28), and the consequent evaluation of the variance, according to (4.30), the coefficient of variation V_δ is computed as reported in equation (4.31).

Table 6.10 reports the values of the error related to the model for each specimen δ_i, also in lognormal terms, i.e. Δ_i.
The resulting coefficient of variation related to the defined model is V_δ = 0,074.

The validity of the model in terms of compatibility of the test population with said model can be checked by limiting the scatteredness of the model at 10%. Since V_δ = 0,074, the compatibility is verified.

specimen	**δ [-]**	**Δ [-]**
1A	1,014	0,013
1bisA	1,057	0,055
1B	0,925	-0,078
1bisB	0,951	-0,050
2A	0,989	-0,011
2bisA	1,040	0,039
2B	0,857	-0,155
2bisB	0,929	-0,074
4A	1,000	0,000
4bisA	1,217	0,196
4B	0,955	-0,046
4bisB	0,988	-0,012
5A	1,002	0,002
5bisA	0,993	-0,007
5B	1,004	0,004
5bisB	1,001	0,001

Table 6.10 – Values of δ_i and Δ_i for L specimens at the ultimate state

Basic variable φ is also characterized by some scatteredness; its coefficient of variation is computed as the ratio between their standard deviation and the mean value, as per definition; resulting in V_φ = 0,102. Therefore, according to equation (6.6), V_{rt} = 0,102.

Finally, the overall scatteredness, related to both the basic variables and the model itself, as indicated by expression (6.7): V_r = 0,127.

These coefficients of variation can be expressed in lognormal terms: Q_δ, Q_{rt} and Q are evaluated according to (4.35), (4.36) and (4.37), respectively.
Q_{rt} and Q_δ can then be normalized with respect to Q, by means of expressions (4.39) and (4.40), correspondingly.

The mean value of the theoretical function is computed as:

$$r_{tm} = m_{\varphi} A_n f_t \tag{6.18}$$

Therefore, r_{tm} is evaluated as the resistance function of the mean values of the basic variable , namely m_{φ} = 0,990, resulting in r_{tm} = 44,72 kN.

According to Table 4.5, and performing a linear interpolation, for a population of 16 specimens, $k_{n,d}$ = 3,988.

The design value of the resistance function at the ultimate state for L specimens is then computed according to equation (4.42): r_d = 29,20 kN.

In order to evaluate the partial safety factor γ^*_M as the ratio between the characteristic and the design values of the resistance function, according to (6.10), the characteristic value r_k is evaluated as:

$$r_k = \varphi_k A_n f_{tk} \tag{6.19}$$

where:

φ_k = 0,855	as computed in section 5.3.4
A_n = 80,00 mm^2	according to Figure 5.1
f_{yk} = 556,8 MPa	as computed in section 5.2.3 for L specimens

The computed value for the characteristic resistance function is r_k = 38,09 kN.

Consequently, γ^*_{M2} = 1,304.

As the ultimate tensile resistance can be defined, in general, as (6.20), in order to maintain as valid the traditional partial safety factor γ_{M2} = 1,25, a coefficient α^* is computed according to (6.12), resulting in α^*_2 = 0,96.

$$R_{td} = \frac{1}{\gamma_{M2}} A_{eff} f_{tk} \tag{6.20}$$

The geometrical corrective factor φ_k can be incorporated in corrective factor η^*, as expressed in (6.15). The resulting corrective factor is η^*_2 = 0,82.

This way, the ultimate tensile resistance can be computed as:

$$R_{td} = \eta_2^* \left(\frac{1}{\gamma_{M2}} A_n f_{tk} \right) \tag{6.21}$$

All the numerical data and results obtained for the evaluation of the ultimate resistance of L specimens, following the procedure described in section 6.2, are reported in Table 6.11 below.

step		**parameter**	**value**	**unit**
step 3	correction factor b	b	1,007	-
step 4	CoV of the error V_δ	$\overline{\Delta}$	-0,008	-
		s_Δ^2	0,006	-
		V_δ	0,074	-
step 6	CoV of basic variables V_{rt}	m_φ	0,990	-
		s_φ	0,101	-
		V_φ	0,102	-
		V_{rt}	0,102	-
step 7	design resistance r_d	V_r	0,127	-
		Q_δ	0,074	-
		Q_{rt}	0,102	-
		Q	0,126	-
		α_δ	0,588	-
		α_{rt}	0,809	-
		r_{tm}	44,72	kN
		r_d	29,20	kN
step 8	characteristic resistance r_k	φ_k	0,855	-
		A_n	80,00	mm^2
		f_{tk}	556,8	MPa
		r_k	38,09	kN
step 9	partial safety factor γ^*_M	γ^*_{M2}	1,304	-
step 10	corrective factor η^*	α^*_2	0,96	-
		η^*_2	0,82	-

Table 6.11 – Data and results for the ultimate resistance of L specimens

6.5.1 Transversal direction

The same approach followed for the longitudinal specimens is adopted for T specimens as well. In Table 6.12 are reported the values of the basic variable, i.e. geometrical corrective factor, for each tested specimen, the mean value of the ultimate strength for milled T specimens (Table 5.1), as well as the values of the theoretical function r_{ti}, according to expression (6.17), and the values of the maximum force withstood by each specimen during testing, corresponding to experimental values r_{ei}.

	theoretical				**experimental**
specimen	**φ [-]**	**L [mm]**	**σ_u [MPa]**	**r_{ti} [kN]**	**r_{ei} [kN]**
1C	0,999	20,1	570,32	45,80	40,10
1bisC	0,998	20,4	570,32	46,43	39,06
1D	0,914	20,0	570,32	41,71	40,12
1bisD	0,905	19,9	570,32	41,07	38,99
2C	0,906	19,5	570,32	40,28	35,17
2bisC	0,928	20,0	570,32	42,33	39,43
2D	0,936	19,6	570,32	41,86	38,91
2bisD	0,930	20,2	570,32	42,88	39,14
4C	1,081	22,8	570,32	56,25	55,96
4bisC	1,072	26,6	570,32	65,08	63,57
4D	1,141	22,7	570,32	59,08	54,07
4Dbis	1,107	26,0	570,32	65,67	63,30
5C	1,100	29,4	570,32	73,80	66,98
5bisC	1,118	25,4	570,32	64,80	58,31
5D	1,061	30,5	570,32	73,81	74,17
5bisD	1,058	27,5	570,32	66,40	60,22

Table 6.12 – Values of r_{ti} and r_{ei} for T specimens at the ultimate state

Figure 6.6 presents graphically all (r_{ti},r_{ei}) values, as well as the line characterized by the ideal slope, i.e. with an inclination of 45° passing through the origin of the axes, and the best-fit line, characterized by a correction factor b = 0,934, computed according to expression (4.25).

The model inherently carries an error, and in order to quantify it, the error related to it for each specimen needs to be evaluated, according to (4.27), also in lognormal terms, as expressed by (4.28). These values are reported in Table 6.13

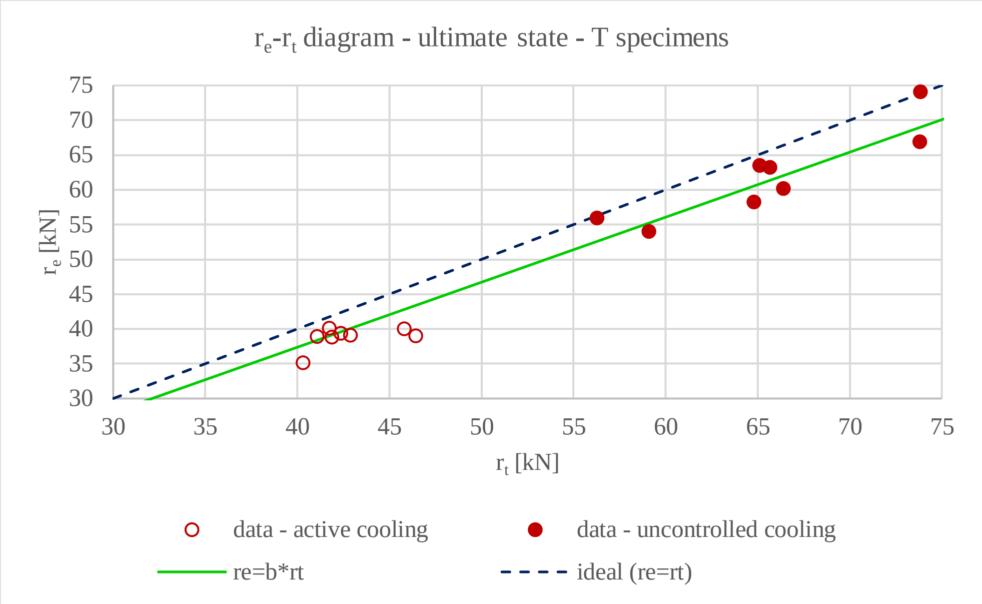

Figure 6.6 – r_e-r_t diagram for T specimens at the ultimate state, with best-fit slope (b=0,934)

specimen	**δ [-]**	**Δ [-]**
1C	0,937	-0,065
1bisC	0,900	-0,105
1D	1,030	0,029
1bisD	1,016	0,016
2C	0,935	-0,068
2bisC	0,997	-0,003
2D	0,995	-0,005
2bisD	0,977	-0,023
4C	1,065	0,063
4bisC	1,045	0,044
4D	0,979	-0,021
4Dbis	1,032	0,031
5C	0,971	-0,029
5bisC	0,963	-0,038
5D	1,075	0,073
5bisD	0,971	-0,030

Table 6.13 – Values of δ_i and Δ_i for T specimens at the ultimate state

After evaluating the variance of the error in lognormal terms, as expressed in (4.30), the scatteredness provided by the model is computed according to equation (4.31), and the coefficient of variation is equal to $V_\delta = 0{,}049$.
As V_δ is smaller than 10%, the test population can be considered compatible with the model.

The basic variable, namely the geometrical corrective factor, is characterized by a certain scatteredness: $V_\varphi = 0{,}082$; consequently, $V_{rt} = 0{,}082$ as well, according to (6.6).

Combining V_δ and V_{rt} as indicated by (6.7), the overall scatteredness is $V_r = 0{,}095$.
All these coefficients of variation can be expressed in lognormal terms, according to (4.35), (4.36) and (4.37), obtaining Q_δ, Q_{rt} and Q, correspondingly. The values related to the model and the basic variables only are then normalized by means of Q, resulting in α_δ and α_{rt}, according to (4.40) and (4.39), respectively.
According to equation (6.8), in which $m_\varphi = 1{,}016$, the mean value of the resistance function is $r_{tm} = 46{,}35$ kN.
Finally, being $k_{n,d} = 3{,}988$ and along with expression (4.42), the design value of the resistance function is $r_d = 31{,}52$ kN.

The characteristic values of the basic variables, as evaluated in chapter 5, are: $f_{tk} = 500{,}4$ MPa and $\varphi_k = 0{,}855$, while $A_n = 80{,}00$ mm^2, as reported in Table 5.10. Applying equation (6.9), the characteristic value of the resistance function is $r_k = 34{,}23$ kN.

The resulting partial safety factor, computed as expressed by (6.10), is $\gamma^*_{M2} = 1{,}086$, which is related to the traditional value γ_{M2}, reported in [19], by means of factor $\alpha^*_2 = 1{,}15$, according to (6.12). In order to account for the geometrical corrective factor φ_k as well as α^*_2 and express the ultimate tensile resistance as indicated in expression (6.21), corrective factor η^*_2 is introduced and computed according to equation (6.15), resulting in $\eta^*_2 = 0{,}98$.

Table 6.14 reports all data and results obtained for the evaluation of the resistance of T specimens at the ultimate stress.

step		parameter	value	unit
step 3	correction factor b	b	0,934	-
step 4	CoV of the error V_δ	$\overline{\Delta}$	-0,008	-
		s_Δ^2	0,002	-
		V_δ	0,049	-
step 6	CoV of basic variables V_{rt}	m_φ	1,016	-
		s_φ	0,083	-
		V_φ	0,082	-
		V_{rt}	0,082	-
step 7	design resistance r_d	V_r	0,095	-
		Q_δ	0,049	-
		Q_{rt}	0,081	-
		Q	0,095	-
		α_δ	0,517	-
		α_{rt}	0,856	-
		r_{tm}	46,35	kN
		r_d	31,52	kN
step 8	characteristic resistance r_k	φ_k	0,855	-
		A_n	80,00	mm^2
		f_{tk}	500,4	MPa
		r_k	34,23	kN
step 9	partial safety factor γ^*_M	γ^*_{M2}	1,086	-
step 10	corrective factor η^*	α^*_2	1,15	-
		η^*_2	0,98	-

Table 6.14 – Data and results for the ultimate resistance of T specimens

6.5.2 *Both directions (L and T)*

As for the resistance at yielding, directions L and T are evaluated together, in order to provide a value for the corrective coefficient η* that is independent on the orientation of the printed material. Again, the procedure outlined in section 6.2 is followed for said evaluation.

The data provided in Table 6.9 and Table 6.12 are reviewed, setting $f_{t,avg}$ = 567,39 MPa, i.e. as the average between the mean value for milled longitudinal and transversal. The corrective factor b is again computed according to (4.25), resulting in b = 0,970; this result is reported in graphical form in Figure 6.7.

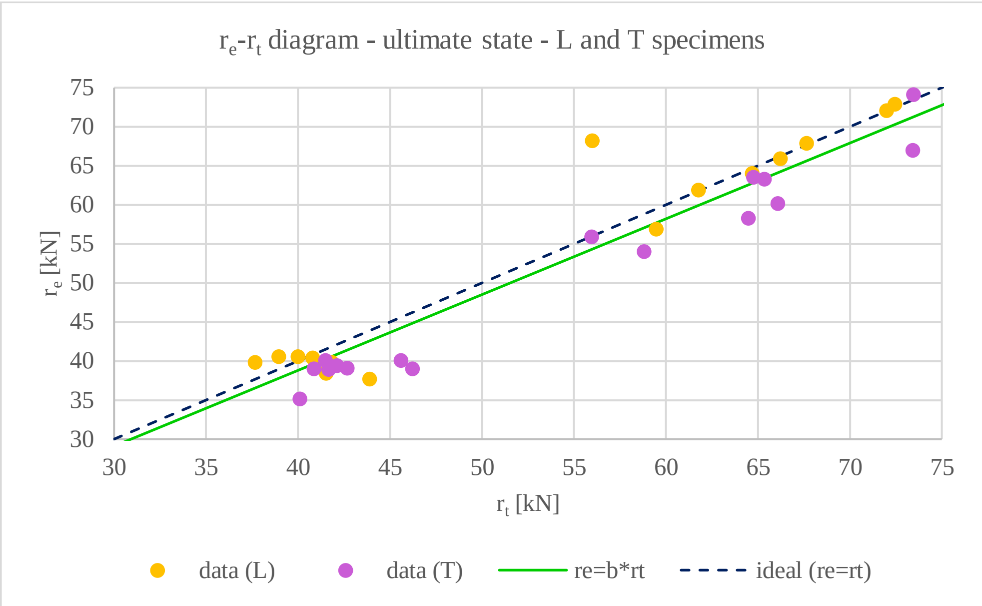

Figure 6.7 – r_e-r_t diagram for both L and T specimens at the ultimate state, with best-fit slope (b=0,970)

According to expression (4.31), the scatteredness provided by the model is V_δ = 0,070, while that carried by the basic variable is V_{rt} = 0,093.
Merging these results in accordance with (6.7), the overall scatteredness is V_r = 0,117.

Since the scatteredness of the model is lower than 10%, which is the maximum allowable value set for this problem, test population and model are compatible.

Q_δ, Q_{rt} and Q are evaluated, following equations (4.35), (4.36) and (4.37) respectively, and α_δ and α_{rt} are consequentially computed, as correspondingly stated in (4.40) and (4.39).
Knowing that r_{tm} = 45,53 kN according to (6.8), where m_φ = 1,003, the design value of the resistance function can be computed as r_d = 30,78 kN, following (4.43).

As for the yielding resistance, since T specimens present a lower value of the ultimate stress, the value of f_{tk} is taken accordingly, equal to 500,4 MPa, while A_n = 80,00 mm^2 and φ_k = 0,855; consequently r_k = 34,23 kN as for T specimens only.

The partial safety factor is computed according to (6.10) and is γ^*_{M2} = 1,112; hence, the calibrating factor α^*_2 is equal to 1,12, applying expression (6.12).
Finally, α^*_2 is combined with the geometrical corrective factor φ_k according to equation (6.15), and the resulting corrective factor is η^*_2 = 0,96.

All data, computations and results involved in the evaluation of the corrective factor η^*_2, according to the procedure delineated in section 6.2, needed to express the design tensile ultimate resistance as (6.21), are reported in Table 6.15 below.

step		parameter	value	unit
step 3	correction factor b	b	0,970	-
step 4	CoV of the error V_δ	$\overline{\Delta}$	-0,008	-
		s_Δ^2	0,005	-
		V_δ	0,070	-
step 6	CoV of basic variables V_{rt}	m_φ	1,003	-
		s_φ	0,094	-
		V_φ	0,093	-
		V_{rt}	0,093	-
step 7	design resistance r_d	V_r	0,117	-
		Q_δ	0,070	-
		Q_{rt}	0,093	-
		Q	0,117	-
		α_δ	0,603	-
		α_{rt}	0,798	-
		r_{tm}	45,53	kN
		r_d	30,78	kN
step 8	characteristic resistance r_k	φ_k	0,855	-
		A_n	80,00	mm^2
		f_{tk}	500,4	MPa
		r_k	34,23	kN
step 9	partial safety factor γ^*_M	γ^*_{M2}	1,112	-
step 10	corrective factor η^*	α^*_2	1,12	-
		η^*_2	0,96	-

Table 6.15 – Data and results for the ultimate resistance of both L and T specimens

6.5.3 Results

Table 6.16 below reports all noteworthy values obtained following the procedure outlined in section 6.2, for L and T specimens, both separately and combined.

parameter	direction L	direction T	directions L and T	units
b	1,007	0,934	0,970	-
V_δ	0,074	0,049	0,070	-
V_{rt}	0,102	0,082	0,093	-
V_r	0,127	0,095	0,117	-
r_d	29,20	31,52	30,78	kN
r_k	38,09	34,23	34,23	kN
γ^*_{M2}	1,304	1,086	1,112	-
α^*_2	0,96	1,15	1,12	-
η^*_2	0,82	0,98	0,96	-

Table 6.16 – Summary of results for ultimate resistance

Generally speaking, from a qualitative point of view, the conclusions drawn for the yielding resistance (section 6.4.4) are also valid for the ultimate one, as elaborated hereafter.

The model is characterized by a scatteredness that spans between 5 and 7% over the three cases, which is generally lower than for yielding; furthermore, as for the yielding resistance, T specimens present the lower level of variability.
Concerning basic variable φ, namely in terms of V_{rt}, T specimens present the smallest value, which means that the experimental values for the geometrical corrective factor are characterized by a smaller variability; on the other hand, as for yielding, L presents the largest value of V_{rt}.

In terms of α^*_2, i.e. the ratio between the traditional value of the partial safety factor γ_{M2} = 1,25 and that computed according to (6.10), from Table 6.16 it is clear that γ_{M0} is about 96% of γ^*_{M2} for L specimens, while it is about 10-13% larger for T specimens, alone and combined with longitudinal ones. In other words, the traditional value must be increased of about 4% for direction L, while it should be decreased to about 87-89% in the other two cases.

Recalling expression (6.21):

$$R_{td} = \eta_2^* \left(\frac{1}{\gamma_{M2}} A_n f_{tk} \right)$$

The key result is, therefore, corrective factor η^*_2.

This coefficient is defined in a way that allows to maintain the general formulation to evaluate the design resistance at the ultimate state, while calibrating the traditional values to account for the particularities of the WAAM-produced material, namely the roughness of the as-built element and any other imperfection that could not be accounted for in previous evaluation and calibrations, i.e. those performed in chapter 5, regarding strength and geometry as two independent characteristics.

Regarding this, Table 6.16 shows that T specimens, separately as well as together with L ones, are characterized by a similar value of η^*_2, while it is quite smaller for the longitudinal direction alone, as for yielding.

Following the same reasoning developed in section 6.4.4, this difference can be associated to two factors: first, the fact that L specimens are characterized by a larger value of r_k; at the same time, they present a smaller value for r_d, as the overall scatteredness is larger for direction L than for T or for the two orientations combined.
The factor mainly responsible for this behavior is the scatteredness of the basic variable φ, which is a direct measure of the roughness of the WAAM-produced material, since both V_{rt} and V_δ are directly dependent on it.

7. Part A – Conclusions

7.1 Statistical determination of experimental results

The first portion of part A, namely chapter 5, is focused on the definition of the characteristic values of the properties of the material, in particular mechanical and geometrical.

Mechanical properties describe the behavior of the material and its response when subjected to a traction test, in terms of elastic behavior (Young's modulus), performance at yielding (0.01% and 0.2% proof stresses) and at the ultimate state (ultimate stress and strain).
Geometrical properties are related to the definition and quantification of the roughness that is intrinsic of the 3D-printed material.

In both cases, experimental results have been analyzed accounting for the printing direction: parallel (L), orthogonal (T) and inclined of 45° (D) with respect to the orientation of the applied external load.
While for geometrical properties, namely corrective factor φ which relates nominal and effective values for the thickness, can be taken as independent on the printing direction, for mechanical properties the specimen's orientation is of paramount importance and demonstrates the anisotropy of the WAAM-produced material.

In particular, T specimens carry the lowest characteristic values for all mechanical properties, while D specimens behave the best in terms of strength, though L specimens are characterized by the highest ductility. These characteristic values are reported in Table 7.1 below.

			direction		
parameter	**symbol**	**unit**	**L**	**T**	**D**
Young's modulus	E	GPa	135,48	111,88	184,23
0.01% proof stress	$\sigma_{0.01\%}$	MPa	235,66	232,29	255,75
0.2% proof stress	$\sigma_{0.2\%}$	MPa	333,83	323,22	402,85
ultimate stress	σ_u	MPa	556,78	500,39	295,89
ultimate strain	ε_u	%	17,62	14,49	14,18

Table 7.1 – Summary of the characteristic values of key mechanical parameters

7.2 Resistance function

Chapter 6 delves into the definition of the resistance function, both in characteristic and design terms, for the assessment of partial safety factors.
These evaluations are made at yielding and the ultimate state, accounting for L and T specimens, both separately and combined together.

In particular, the design value of the resistance function is assessed based on the mean values of the basic variables, their variability and the scatteredness related to the definition of the model itself; the characteristic value, on the other hand, is simply evaluated by means of the characteristic values previously defined.

Table 7.2 shows how the partial safety factor, computed as the ratio of characteristic and design value of the resistance function, mainly decreases as the scatteredness associated to the geometry decreases, which is evident both in terms of V_δ and V_{rt}.

For this reason, the main objectives for future studies and for the development of WAAM technologies within the construction industry can be: firstly, for the producing companies to be able to assure a certain level of variability in terms of roughness of the printed material; then, for researchers to be able to assign certain values of the corrective coefficient for partial safety factors η^* to said given values of the coefficient of variation of geometrical corrective factor φ.

	yielding			**ultimate state**		
property	**L**	**T**	**L+T**	**L**	**T**	**L+T**
V_δ [%]	9,16	7,13	8,78	7,44	4,92	7,03
V_φ [%]	10,2	8,16	9,32	10,2	8,16	9,32
r_k [kN]	22,83	22,11	22,11	38,09	34,23	34,23
r_d [kN]	15,84	16,94	16,96	29,20	31,52	30,78
γ^*_M [-]	1,44	1,31	1,30	1,30	1,09	1,11
γ_M [-]	1,10	1,10	1,10	1,25	1,25	1,25
α^* [-]	0,76	0,84	0,84	0,96	1,15	1,12
η^* [-]	0,65	0,72	0,72	0,82	0,98	0,96

Table 7.2 – Summary of results in terms of resistance function and partial safety factors

PART B: CALIBRATION OF THE STRESS-STRAIN BEHAVIOR FOR THE FINITE ELEMENT ANALYSIS OF A DIGITAL INPUT MODEL

8. Finite Element Analysis

Structural analysis has become increasingly more complex as designs started presenting more elaborate shapes and employing non-standard geometries, which standard analytical formulations can hardly solve, if at all. Finite Element Analysis is an extremely helpful tool in this sense, as it allows to solve any kind of problems through numerical integration.

8.1 Finite Element Method

The Finite Element Method is comprised of the following steps:

1) Discretization: the component is subdivided into smaller elements, connected to each other through nodes, and hence a mesh is created. Meshes can be h-refined, by increasing the number of elements, which then become smaller and smaller, or p-refined, namely each element is determined by higher-order polynomials, eliminating some degrees of freedom (static condensation).
2) Definition of element governing equations: for each element, the governing equations are defined with respect to the local coordinate system, relating mechanical properties and boundary conditions, by means of the constitutive, compatibility and equilibrium equations, hence through the definition of the stiffness matrix via numerical integration.
3) Assembly of the global governing equations: the elemental governing equations are translated into global governing equations, respecting compatibility (consistency in terms of nodal displacements) and equilibrium rules (uniformity with regards to nodal forces).
4) Imposition of boundary conditions: both Dirichlet, regarding initial displacements and constraints, and Neumann (concerning applied external forces) boundary conditions are applied at the nodes.
5) Solution: the differential equations describing the type of analysis to be performed (static, dynamic, transient, etc.) are solved at this stage.
6) Post-processing: only displacements and forces are obtained through the solution of differential equation; by applying the constitutive, compatibility and equilibrium equations, it is possible to recover derived quantities, such as stresses and strains.

8.2 FEA – Advantages and limitations

The Finite Element Method obviously allows for a very wide range of applications, which makes it a very valid tool in the definition and study of complex structural elements, such as those that can be produced using Wire-and-Arc Additively Manufacturing.

But while exploiting a Finite Element Analysis allows for the study of complex structures and elements, which could be hardly achieved through traditional analytical methods, it is important to keep in mind the limitations that such analysis carries.
Firstly, it is based on numerical integration, therefore the solution is not continuous and how the element is discretized plays a crucial role in the validity of the model itself.
Furthermore, other parameters also depend on the designer's discretion: the behavior of materials, the modeling of restraints, the application of external forces, and so on.

9. Calibration of stress-strain models of rough specimens

9.1 Overview

Two 3D scans of rough specimens were provided: specimen 3A and specimen 4D. These scans can be referred to as “Digital Twins” of said specimens, as they report every single geometrical feature that is proper of the respective WAAM-produced element.

Specimen 3A is oriented in the longitudinal direction, and is shown in Figure 9.1; while specimen 4D is transversal, and its geometrical characteristics can be appreciated from Figure 9.2.

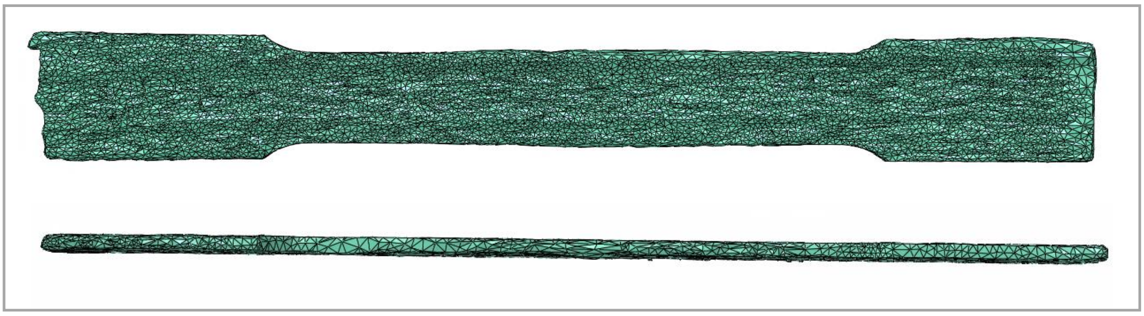

Figure 9.1 – xy and xz views of specimen 3A

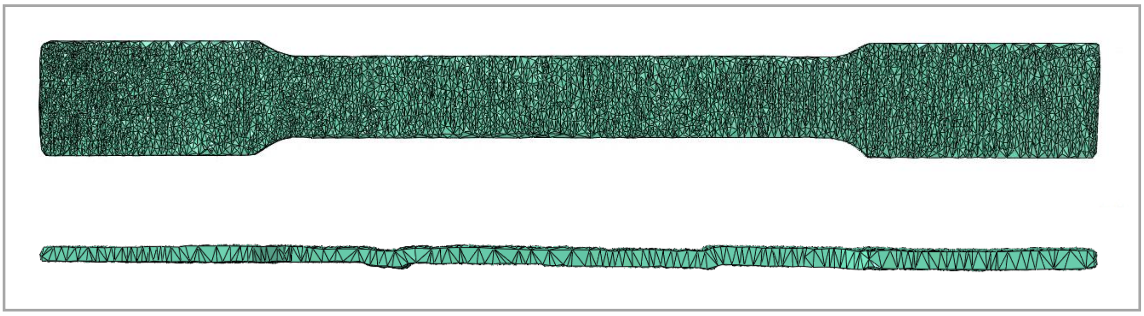

Figure 9.2 – xy and xz views of specimen 4D

Through Digital Image Correlation (DIC), which is an optical method for the measurement of strains and displacements through the comparison between digital images corresponding to different stages of deformation, the constitutive behavior, i.e. the stress-strain relationship, and the response, in terms of force vs displacement, can be obtained.

While the F-u response is unambiguous, stresses and strains are evaluated as expressed by equations (9.1) and (9.2), respectively Hence, based on the way they are defined, they are dependent on the average geometry and, therefore, on the element’s intrinsic roughness and imperfections.

$$\sigma = \frac{F}{A_{eff}} \tag{9.1}$$

$$\varepsilon = \frac{\Delta u}{L_{eff}} \tag{9.2}$$

The goal is to calibrate the stress-strain curve, in particular in terms of Young's modulus E, descriptive of the elastic phase, and 0.2% proof stress $\sigma_{0.2\%}$, representative of the behavior at yielding, which are the main parameters that are of interest at a design level.

The provided Digital Twins are imported into FEA software Abaqus, in which material properties and boundary conditions are properly defined in order to simulate a pull test.
Employing a "Static, General" solver, which is an implicit method, inertia and time-dependent effects, such as creep and swelling, are neglected, which is a fair assumption for the type of analysis that is to be carried; geometrical non-linearity can be taken into account through the solver's settings (NLGeom).

In order to calibrate Young's modulus E, the approach is the following: in the elastic phase, the constitutive law is (9.3), similarly, reaction force F and displacement u are linearly related by means of axial stiffness K, as indicated in (9.4). As axial stiffness is defined as (9.5), E and K are directly proportional; therefore, deriving the relationship between the specimen's actual axial stiffness K_{ac} and that resulting from the simulation run applying the initially available stress-strain relationship K_{in}, the initial value of E can be properly calibrated.

$$\sigma = E\varepsilon \tag{9.3}$$

$$F = Ku \tag{9.4}$$

$$K = \frac{EA}{L} \tag{9.5}$$

Regarding 0.2% proof stress $\sigma_{0.2\%}$, as there is not a linear relationship between its value and the non-linear post-yielding behavior, the calibration approach is that of trial-and-error.

9.2 Stress-strain model

Annex C of [19] provides guidelines for the modelling of the behavior of the material in terms of the stress-strain relationship.

This approach is based on two models: Ramberg-Osgood equation (9.6), formulated in 1943 to describe the non-linear relationship between stresses and strains up until the yielding point of the material [20]; and Rasmussen equation (9.7), which is used to model the material's behavior within the plastic domain.

$$\varepsilon = \begin{cases} \dfrac{\sigma}{E} + 0.002\left(\dfrac{\sigma}{f_y}\right)^n & \sigma \le f_y \qquad (9.6) \\ 0.002 + \dfrac{f_y}{E} + \dfrac{\sigma - f_y}{E_y} + \varepsilon_u\left(\dfrac{\sigma - f_y}{f_u - f_y}\right)^m & f_y < \sigma \le f_u \qquad (9.7) \end{cases}$$

where:

$$n = \frac{\ln 20}{\ln\left(\dfrac{f_y}{R_{p0.01}}\right)} \tag{9.8}$$

$$E_y = \frac{E}{1 + 0.002n\dfrac{E}{f_y}} \tag{9.9}$$

$$m = 1 + 3.5\frac{f_y}{f_u} \tag{9.10}$$

f_y corresponds to 0.2% proof stress $\sigma_{0.2\%}$

f_u corresponds to ultimate stress σ_u

$R_{p0.01}$ corresponds to 0.01% proof stress $\sigma_{0.01\%}$

As thoroughly explained in [21], post-necking behavior cannot be properly described by the stress-strain data collected from testing; instead, the hardening behavior that occurs after diffuse necking must be defined by means of different models.

One widely used model, which will be applied here as well, is that defined by Hollomon [21]: it is a power-law model relating true stresses σ_t and true strains ε_t by means of a strength coefficient K_1 and a strain hardening exponent n_1. This model is described by (9.11).

$$\sigma_t = K_1 \varepsilon_t^{n_1} \tag{9.11}$$

This model is directly defined in terms of true values and not engineering ones: the latter are defined in terms of the initial geometry of the specimen, hence they do not account for changes in the cross-sectional dimensions when large strains occur (Figure 9.3); for this reason, the behavior of the material is more accurately described in terms of true values.

As true values represent a more precise characterization of the material's behavior, those are the values to input as material properties in FEA software programs, such as Abaqus.
True values can be derived from engineering ones as follows:

$$\sigma_t = \sigma_{eng}\left(1 + \varepsilon_{eng}\right) \tag{9.12}$$

$$\varepsilon_t = \ln\left(1 + \varepsilon_{eng}\right) \tag{9.13}$$

It is also useful to separate the elastic and plastic parts of the true strain, as, in the definition of the plastic behavior in Abaqus, only plastic values ($\varepsilon_{t,pl}$) are required. Elastic and plastic values are to be computed according to (9.14) and (9.15), respectively.

$$\varepsilon_{t,el} = \frac{\sigma_t}{E} \tag{9.14}$$

$$\varepsilon_{t,pl} = \varepsilon_t - \varepsilon_{t,el} \tag{9.15}$$

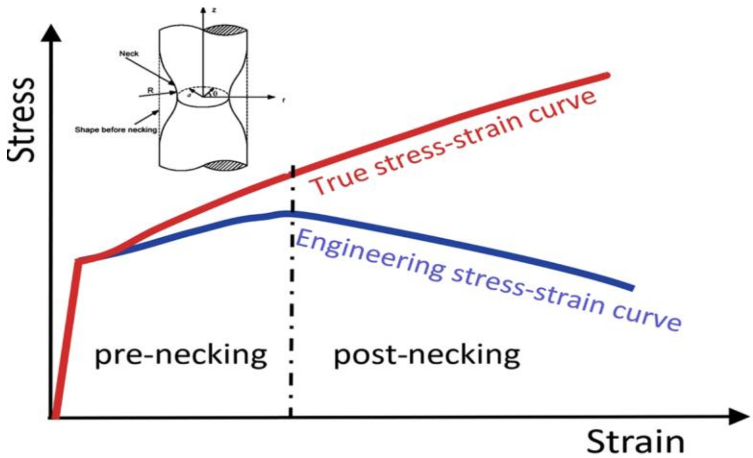

Figure 9.3 – Qualitative schematization of engineering vs true stress-strain curves [21]

According to Considére criterion (Figure 9.4), the onset of diffuse necking is defined as:

$$\sigma_{t,neck} = \left.\frac{d\sigma_t}{d\varepsilon_t}\right|_{\varepsilon_t = \varepsilon_{t,neck}} \tag{9.16}$$

Applying the definition of σ_t, i.e. (9.11), to expression (9.16) above, necking begins at a strain corresponding to the strain hardening exponent, as reported below:

$$\varepsilon_{t,neck} = n_1 \tag{9.17}$$

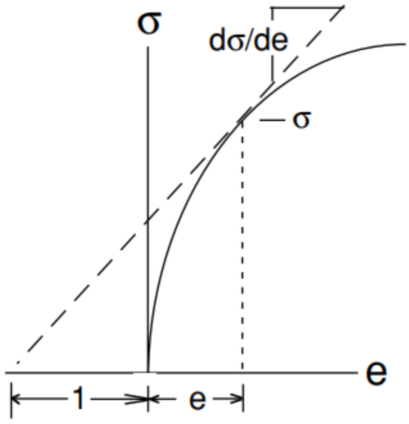

Figure 9.4 – Considére construction for necking in tension [22]

The value of the strain hardening exponent can be evaluated following the procedure delineated in EN ISO 10275:2007 [23]: n_1 is computed considering a portion of the stress-strain curve in the plastic region of a specimen subjected to uniaxial testing.

For the specimens analyzed, said plastic region is that in between 2% strain and ultimate strain, which corresponds to the maximum stress reached during testing (Figure 9.5).

According to this Standard, the tensile strain hardening exponent is to be computed as:

$$n_1 = \frac{N\sum x_i y_i - \sum x_i \sum y_i}{N\sum x_i^2 - (\sum x_i)^2} \tag{9.18}$$

where:

N is the number of measurements made in the plastic interval (>5)

$$x = \ln \varepsilon_{t,pl} \tag{9.19}$$

$$y = \ln \sigma_t \tag{9.20}$$

Regarding strength coefficient K_1, according to [24], there is a relationship between the ultimate tensile strength UTS, namely σ_u, and the strain hardening coefficient n_1, as indicated in (9.21). Therefore, K_1 can be computed as reported in equation (9.22).

$$UTS = K_1 \left(\frac{n_1}{e}\right)^{n_1} \tag{9.21}$$

$$K_1 = UTS \left(\frac{n_1}{e}\right)^{-n_1} \tag{9.22}$$

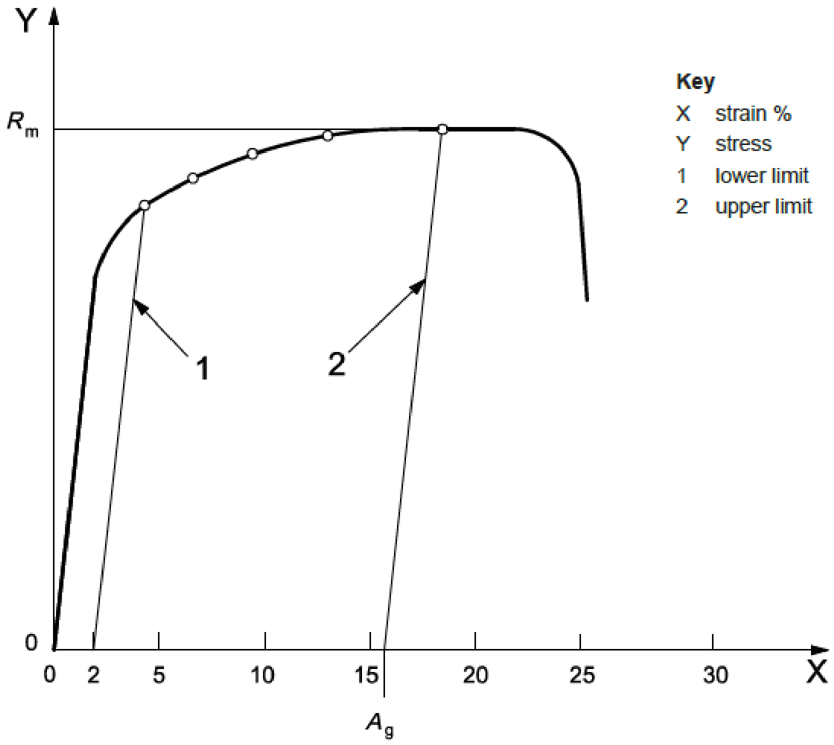

Figure 9.5 – Range for the determination of strain hardening exponent n_1 [23]

Recapitulating, the stress-strain models employed from here onwards are the following:

model	phase	formulation	parameters
Ramberg-Osgood	elastic	$\varepsilon = \frac{\sigma}{E} + 0.002\left(\frac{\sigma}{\sigma_{0.2\%}}\right)^n$	$n = \frac{\ln 20}{\ln\left(\frac{\sigma_{0.2\%}}{\sigma_{0.01\%}}\right)}$
Rasmussen	plastic (pre-necking)	$\varepsilon = 0.002 + \frac{\sigma_{0.2\%}}{E} + \frac{\sigma - \sigma_{0.2\%}}{E_y} + \varepsilon_u\left(\frac{\sigma - \sigma_{0.2\%}}{\sigma_u - \sigma_{0.2\%}}\right)^m$	$E_y = \frac{E}{1 + 0.002n\frac{E}{\sigma_{0.2\%}}}$ $m = 1 + 3.5\frac{\sigma_{0.2\%}}{\sigma_u}$
Hollomon	post-necking	$\sigma_t = K_1\varepsilon_t^{n_1}$	$n_1 = \frac{N\sum x_i y_i - \sum x_i \sum y_i}{N\sum x_i^2 - (\sum x_i)^2}$ $K_1 = \sigma_u\left(\frac{n_1}{e}\right)^{-n_1}$

Table 9.1 – Stress-strain models and parameters

9.3 Specimen 3A

9.3.1 Characterization of the stress strain model

The value of Young's modulus E is extracted from experimental data by means of Ordinary Least Square Regression (OLSR).

Processing the outputs from DIC regarding the effective stress-strain curve, the values of ultimate stress σ_u, as well as ultimate strain ε_u and strain at failure ε_f, can be extracted.

Combining those with the value of E obtained through OLSR, 0.01% and 0.2% proof stresses, $\sigma_{0.01\%}$ and $\sigma_{0.2\%}$, can be evaluated, as shown in Figure 9.6.

Strain at yielding ε_y is extracted from the effective stress-strain curve, in correspondence of the value of $\sigma_{0.2\%}$.

All these mechanical parameters are reported in Table 9.2.

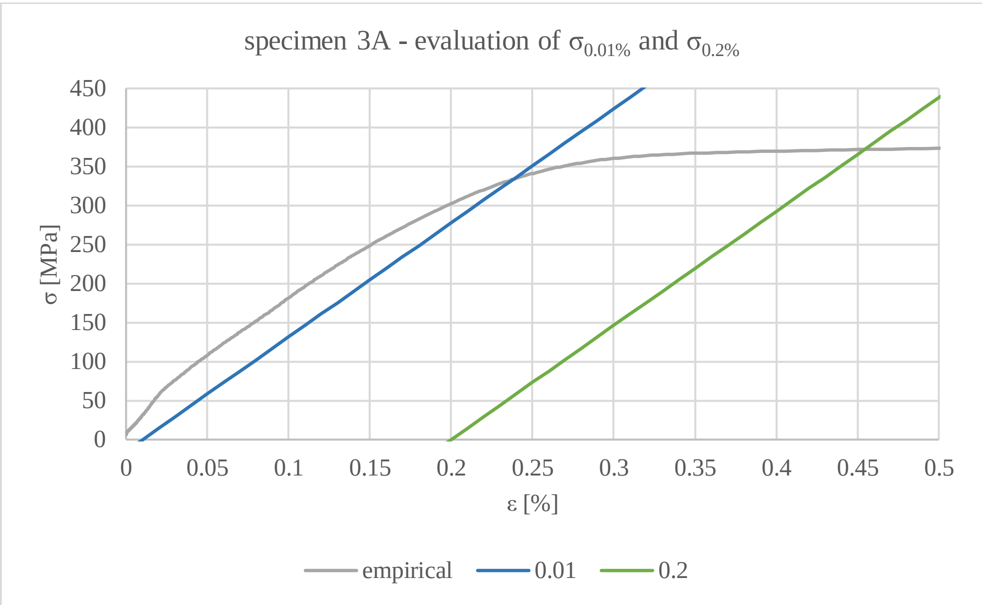

Figure 9.6 – Evaluation of 0.01% and 0.2% proof stresses of specimen 3A

property	symbol	value	unit
Young's modulus	E	146 174	MPa
0.01% proof stress	$\sigma_{0.01\%}$	336,20	MPa
0.2% proof stress	$\sigma_{0.2\%}$	380,05	MPa
ultimate stress	σ_u	599,44	MPa
yielding strain	ε_y	0,765	%
ultimate strain	ε_u	33,27	%
strain at failure	ε_f	37,48	%

Table 9.2 – Mechanical properties of specimen 3A

Applying the models summarized in Table 9.1, the stress-strain model can be defined: all characterizing parameters are reported in Table 9.3. The resulting engineering and true stress-strain curves are plotted in Figure 9.7, next to the experimental ones.

Furthermore, Figure 9.8 compares true experimental and analytical (i.e. based on the defined model) constitutive curves.

model	phase	parameter	value	unit
Ramberg-Osgood	elastic	n	24,43	-
Rasmussen	plastic (pre-necking)	E_y	7 380	MPa
		m	3,22	-
Hollomon	post-necking	n_1	0,26	-
		K_1	1 104	MPa

Table 9.3 – Parameters defining the stress-strain model of specimen 3A

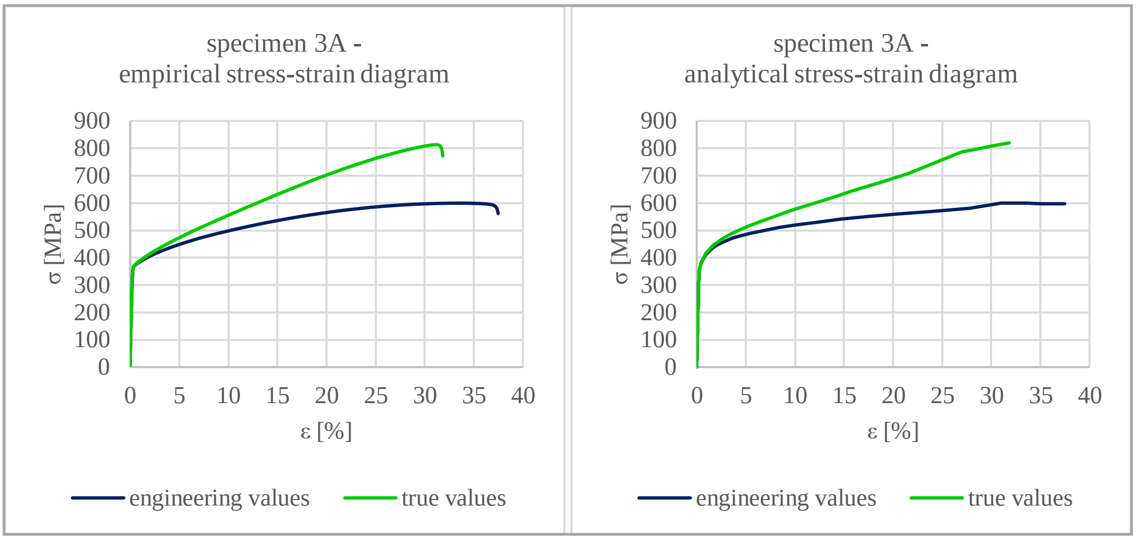

Figure 9.7 – Empirical and analytical engineering and true stress-strain curves of specimen 3A

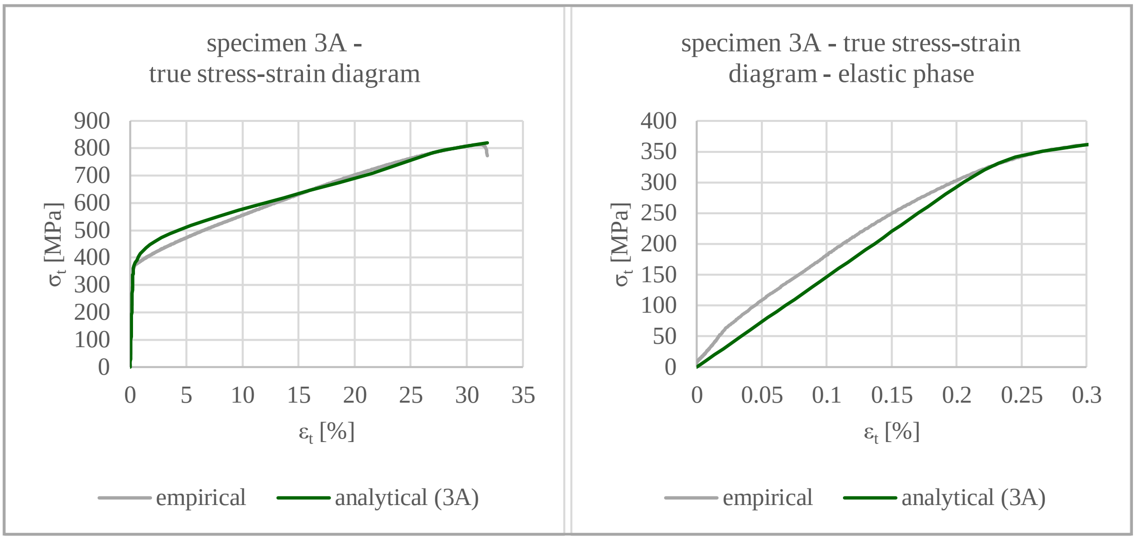

Figure 9.8 – Comparison between empirical and analytical true stress-strain curves of specimen 3A

9.3.2 Definition of the Finite Model in software Abaqus

The first step in the definition of a Finite Model in Abaqus is the characterization of the geometry, in this case, as already stated, a Digital Twin of the specimen was provided as a 3D scan; specimen 3A is shown in Figure 9.1.

Material mechanical properties are defined separately for the elastic and the plastic behaviors. The elastic behavior is considered to be isotropic, and Young's modulus E and Poisson's ratio ν must be set; these input values are reported in Table 9.4.

Regarding the plastic behavior, for which hardening is set as isotropic, the input values required are in terms of yield (true plastic) stress and (true) plastic strain, starting at a stress value corresponding to $\sigma_{0.01\%}$. This is a valid approach thanks to the way Ramberg-Osgood's model is defined; in fact, parameter n makes sure that the interval between the 0.01% and the 0.2% proof stresses is properly modeled.

The true stress-true plastic strain curve is plotted in Figure 9.9, and corresponds to the input values set to define the plastic behavior within the software, some of which are also reported numerically in Table 9.4.

phase	significant steps	input values			
		E [MPa]	**ν [-]**	**σ_t [MPa]**	**$\varepsilon_{t,pl}$ [-]**
elastic	-	146 173	0,44	-	-
plastic	0.01%	-	-	337,006	0
	0.2%	-	-	381,800	0,0020
	necking	-	-	777,790	0,2547
	failure	-	-	819,789	0,3127

Table 9.4 – Main input values in Abaqus for the characterization of material behavior – model 3A

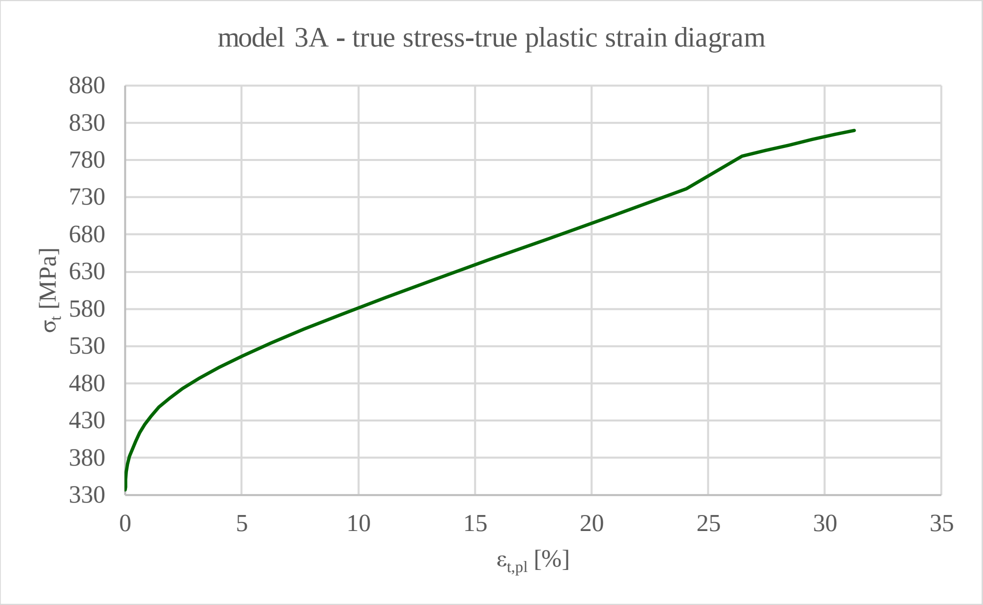

Figure 9.9 – True stress-true plastic strain curve – model 3A

The element must then be discretized by creating a mesh: first, seeds (nodes) are assigned to the part, setting an approximate global size, which in this case is of 2 mm; then, the most suitable element type is attributed to the part and the mesh is therefore created.

For such a complex geometry, the most appropriate element type for its discretization is a C3D10, which is a second-order (10-node) tetrahedral element, schematized in Figure 9.10.

The so-created mesh is comprised of 167703 nodes and 106840 elements.

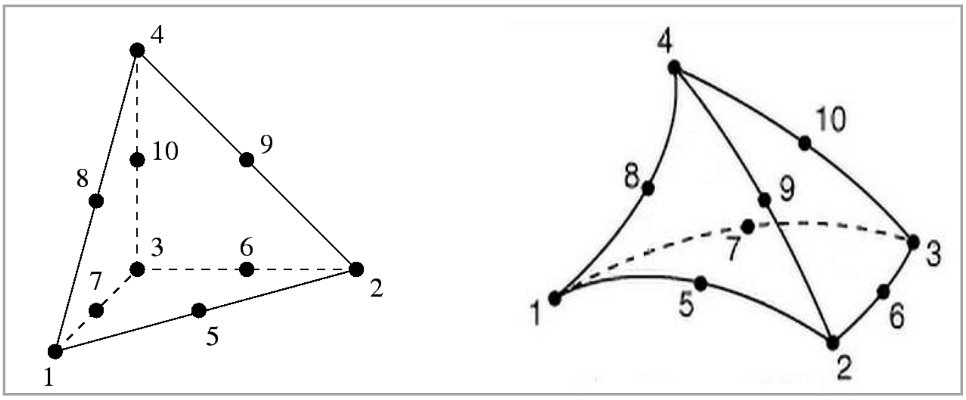

Figure 9.10 – C3D10 Finite Element – undeformed and deformed

The boundary conditions, namely the clamped end and the loaded one, are defined by means of multi-point constraints (MPC), in order to refer many elements' faces to a unique point (Control Point), to which the boundary conditions are directly applied.

Before defining boundary conditions, steps must be defined: at the initial step, the element is at rest; at step "loading", characterized by a Tabular Amplitude relating displacements and time in a 1-to-1 manner, the element undergoes a displacement that linearly increases with time.

Figure 9.11 displays the specimen at the loading step. More in detail, Figure 9.12 shows the fixed end, which is defined by means of an Encastre-type boundary condition; alike, Figure 9.13 depicts the loaded end, characterized by a Displacement-type boundary condition, which fixes all rotations, as well as y and z displacements.

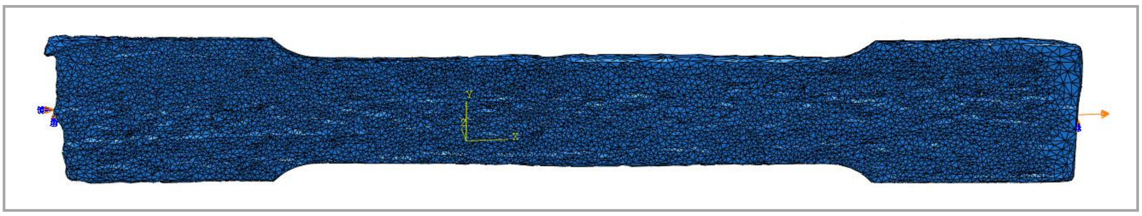

Figure 9.11 – Boundary conditions of model 3A – loading step

Figure 9.12 – Fixed-end of model 3A – xy and zy views

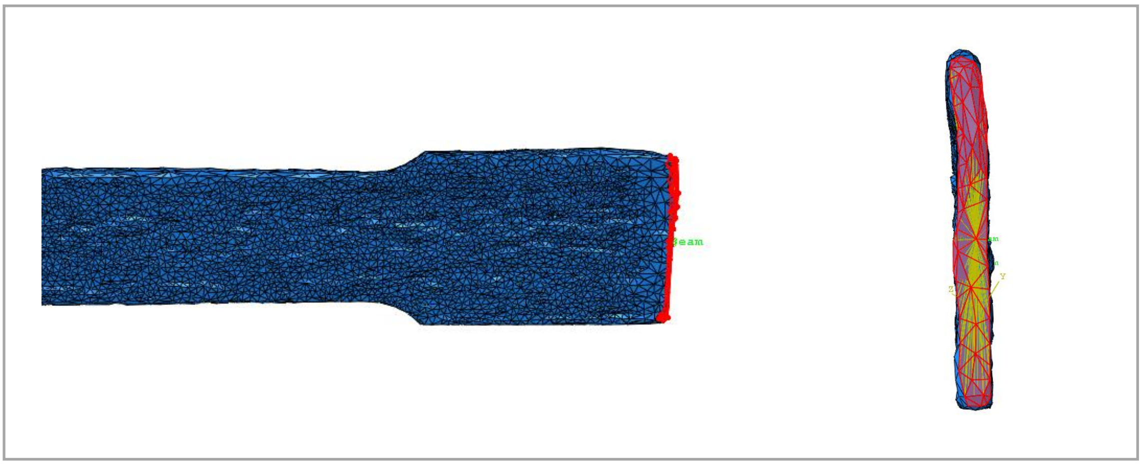

Figure 9.13 – Loaded-end of model 3A – xy and yz views

9.3.3 Results of FEA

The following reported outcomes only regard forces and displacements up until the maximum value of the reaction force F_{max}.

In particular, Figure 9.14 presents the specimen at rest and at the maximum elongation reached for F_{max}; the maximum values in terms of reaction forces and displacements are all reported in Table 9.5.

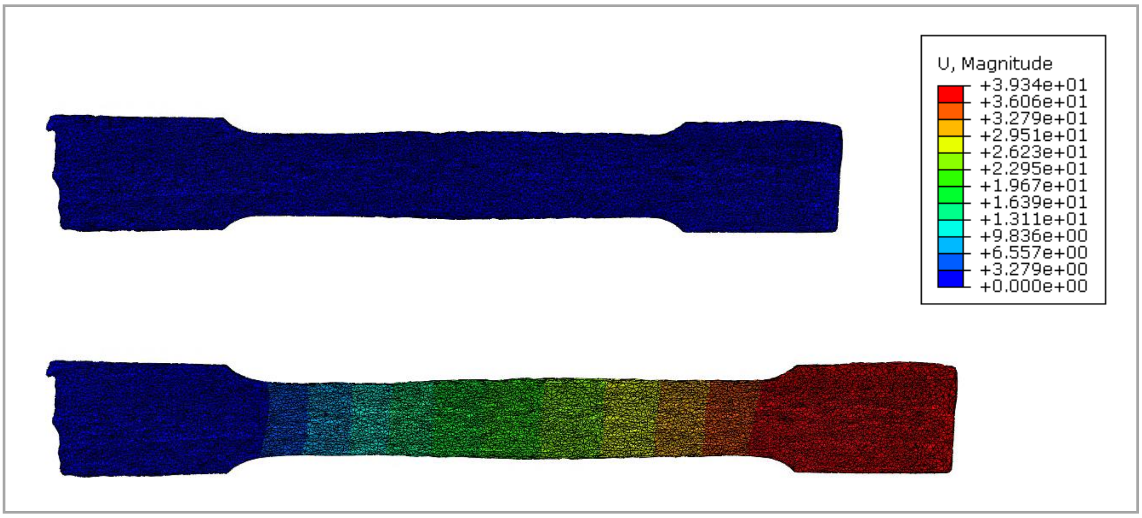

Figure 9.14 – Initial and final displacements from Abaqus – model 3A

	u_{max} [mm]	**F_{max} [kN]**
experimental	52,58	56,25
model 3A	39,34	55,86

Table 9.5 – Maximum values for F-u – model 3A

The results in terms of reaction force versus displacement (F-u) are plotted in Figure 9.15, compared to the experimental results.

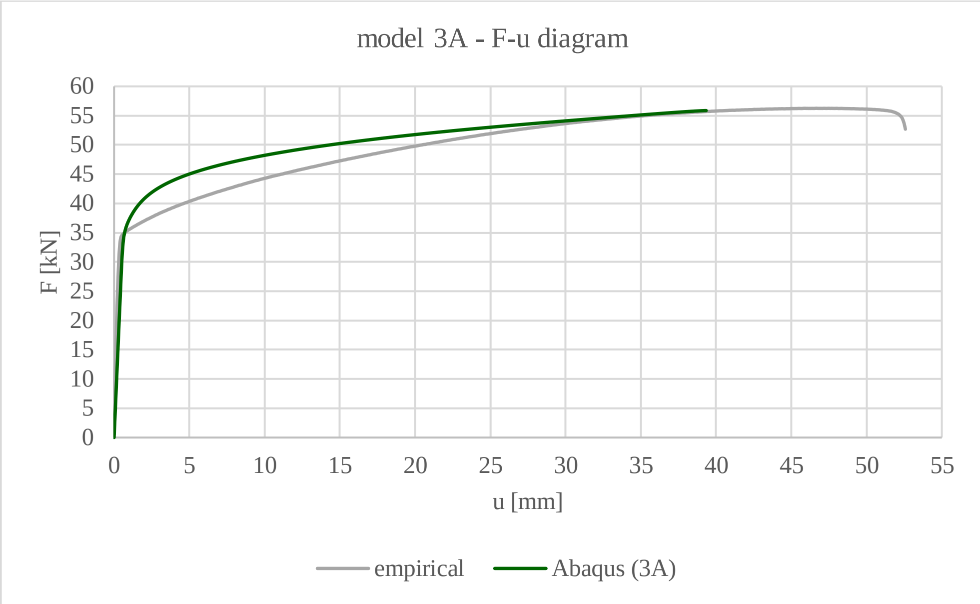

Figure 9.15 – F-u diagram – model 3A

9.3.4 Calibration of Young's modulus E

The first calibration to be performed regards Young's modulus E, hence the elastic phase. In this regard, Figure 9.16 compares the empirical and analytical results in terms of F-u diagram, focusing on the elastic phase, precisely up until u = 1 mm.

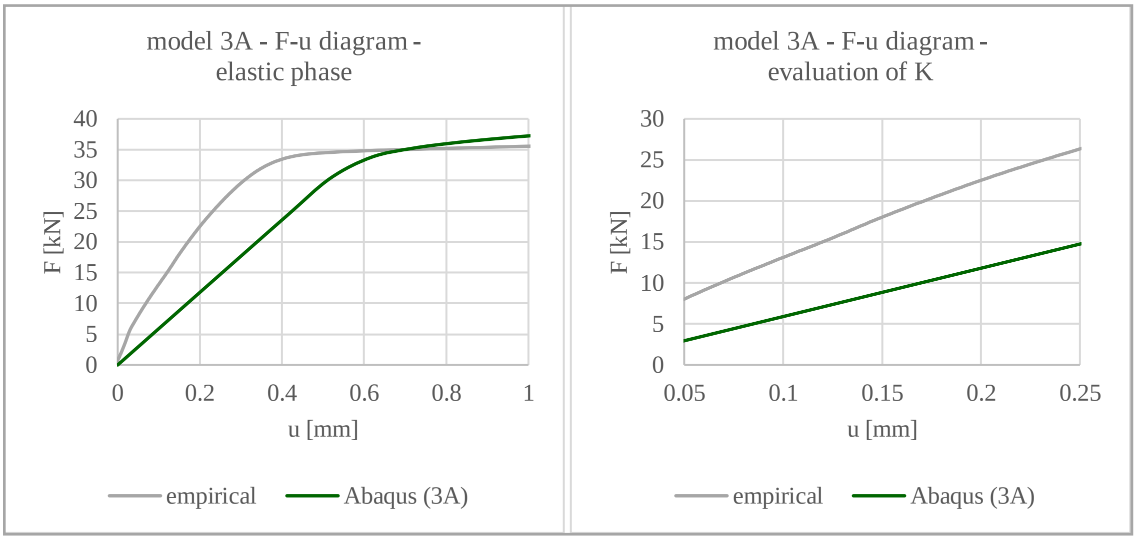

Figure 9.16 – F-u diagram: elastic phase – model 3A

It is evident from Figure 9.16 how the value of E obtained from OLSR and set in the Abaqus model is quite smaller than the actual one.

Referring to an interval of values for the displacement that goes approximately from 0,05 mm to 0,25 mm, by means of linear interpolation, the target axial stiffness can be computed, as reported in Table 9.6: K_{ref} = 91530,35 N/mm.

Regarding the outputs of the finite element analysis, the value of K is assessed for a series of points in the F-u diagram, in between u = 0,010 mm and u = 0,218 mm, obtaining an average value of K_{3A} = 58973,69 N/mm (Table 9.7).

	u [mm]	**F [kN]**	**K [N/mm]**
data	0,050822	8,1090	
	0,249521	26,296	
Δ	0,198698	18,187	
K_{ref}			91530,35

Table 9.6 – Evaluation of axial stiffness K – experimental (3A)

	u [mm]	**F [kN]**	**K [N/mm]**
data	0,010000	0,5898	58978,60
	0,020000	1,1796	58979,00
	0,035000	2,0643	58979,43
	0,057500	3,3913	58978,61
	0,091250	5,3815	58975,78
	0,141875	8,3663	58969,23
	0,217813	12,841	58955,16
K_{3A}			58973,69

Table 9.7 – Evaluation of axial stiffness K – model 3A

As in the elastic phase Young's modulus E and axial stiffness K are directly proportional, thanks to the definition of K itself (9.5), the ratio between reference and model stiffnesses can be applied to the value of E for the model in order to calibrate it; namely:

$$\alpha_E = \frac{K_{ref}}{K_{3A}} \tag{9.23}$$

$$E_{cal1} = \alpha_E E_{3A} \tag{9.24}$$

Therefore, the calibrating factor $\alpha_{E,3A}$ = 1,552; consequently, according to (9.24), the calibrated value of Young's modulus is E_{cal1} = 226 870 MPa. The corresponding stress-strain plot is reported in Figure 9.17.

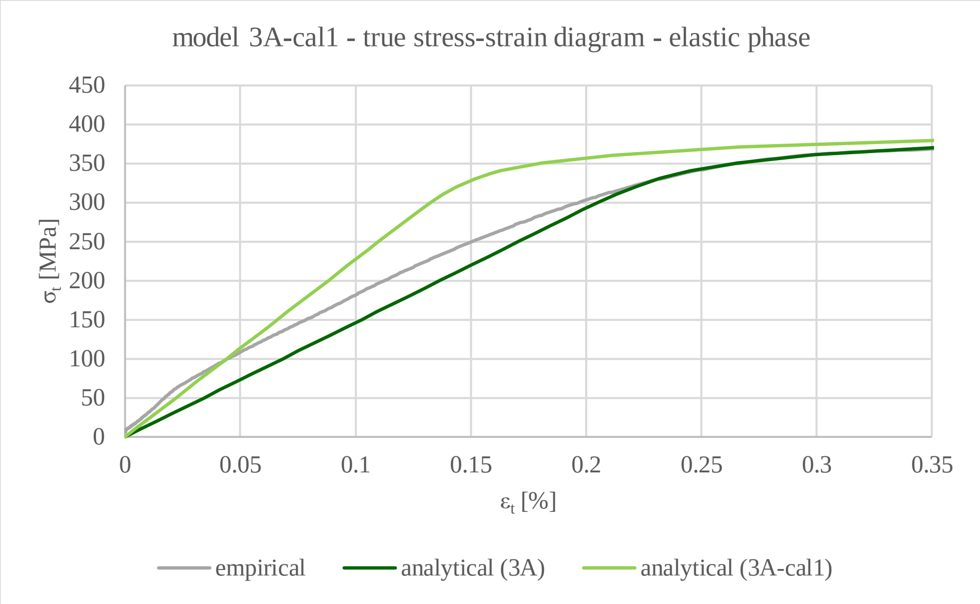

Figure 9.17 – σ-ε diagram: elastic phase – model 3A-cal1

As the first calibration only concerns the elastic phase, and in particular the elastic modulus, the only change in the new input model "3A-cal1" in Abaqus is, indeed, in the definition of E.
With this new value defining the elastic phase, a new output F-u diagram is obtained, and it is reported in Figure 9.18, with a focus on the chosen reference interval for the evaluation of K.

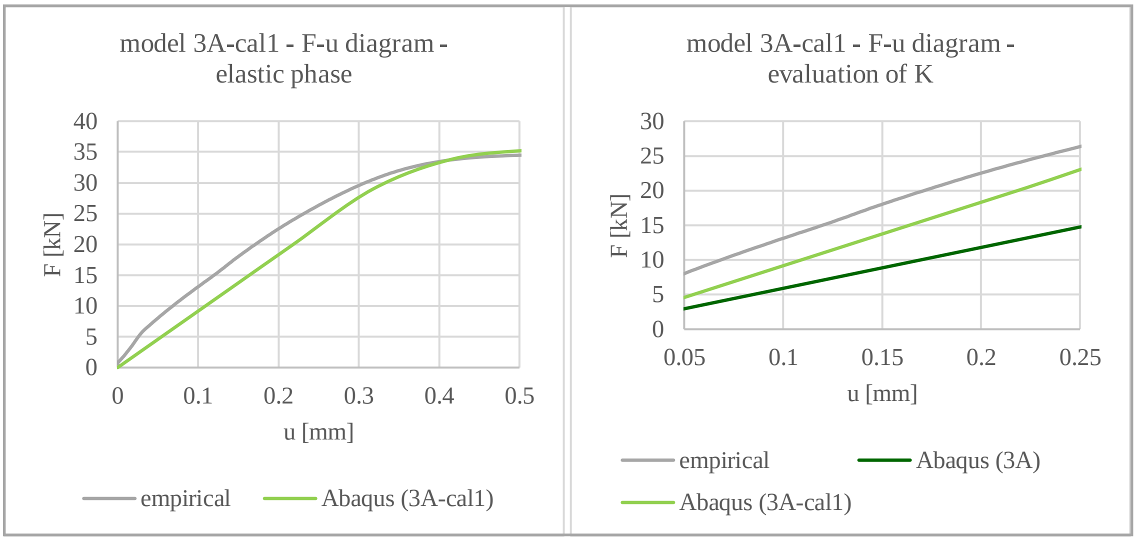

Figure 9.18 – F-u diagram: elastic phase – model 3A-cal1

With the same approach followed for model 3A, the resulting value of the axial stiffness for model 3A-cal1 is K_{cal1} = 91528,68 N/mm (Table 9.8). The corresponding value of $\alpha_{E,cal1}$, according to (9.24), would be 1,000; hence model 3A-cal1 is a valid model for the elastic phase.

	u [mm]	F [kN]	K [N/mm]
data	0,010000	0,9154	91538,70
	0,020000	1,8308	91539,50
	0,035000	3,2039	91539,71
	0,057500	5,2635	91538,61
	0,091250	8,3525	91534,25
	0,141875	12,985	91522,82
	0,217813	19,927	91487,19
K_{cal1}			91528,68

Table 9.8 – Evaluation of axial stiffness K – model 3A-cal1

9.3.5 Calibration of 0.2% proof stress $\sigma_{0.2\%}$

Other than the elastic phase, another crucial point for the behavior and response of a stainless-steel structural element is yielding; in regard to this, the focus is shifted, in particular, in the $\sigma_{0.01\%}$-$\sigma_{0.2\%}$ interval.

Recalling Table 9.1, the model that refers to this interval is Ramberg-Osgood's, characterized by parameter n. Here below are reported equations (9.6) and (9.8) defining the model:

$$\varepsilon = \frac{\sigma}{E} + 0.002\left(\frac{\sigma}{\sigma_{0.2\%}}\right)^{n}$$

$$n = \frac{\ln 20}{\ln\left(\frac{\sigma_{0.2\%}}{\sigma_{0.01\%}}\right)}$$

Recalling the F-u plot for model 3A-cal1, Figure 9.19 focuses on the yielding phase. It can be noticed how the curve follows a path with a wider radius than the one needed to align with the experimental trend. In order for the initial curve to be sharper, the value of exponent n should be higher, hence, $\sigma_{0.2\%}$ should be smaller, while keeping $\sigma_{0.01\%}$ fixed.

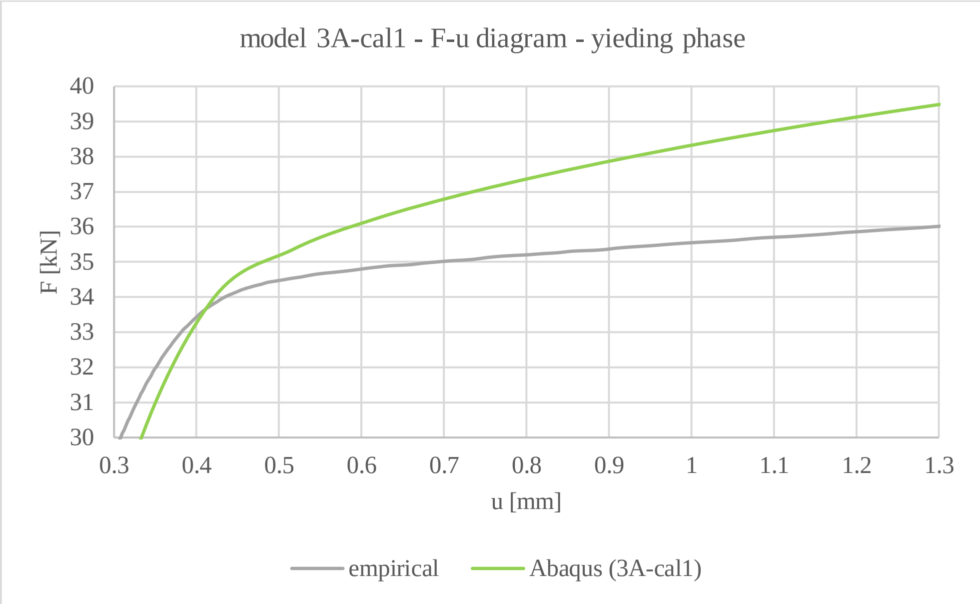

Figure 9.19 – F-u diagram: yielding phase – model 3A-cal1

As a first attempt for the calibration of the value of the 0.2% proof stress, it is assessed based on the calibrated value of the Young's modulus, namely E_{cal1} = 226 870 MPa.
Consequently, according to Figure 9.20, $\sigma_{0.2\%,cal2}$ = 362,99 MPa, hence reducing the initial value of $\sigma_{0.2\%}$ (380,05 MPa) of a factor $\alpha_{0.2\%}$ = 0,955, defined as:

$$\alpha_{0.2\%} = \frac{\sigma_{0.2\%,cal2}}{\sigma_{0.2\%,3A}} \tag{9.25}$$

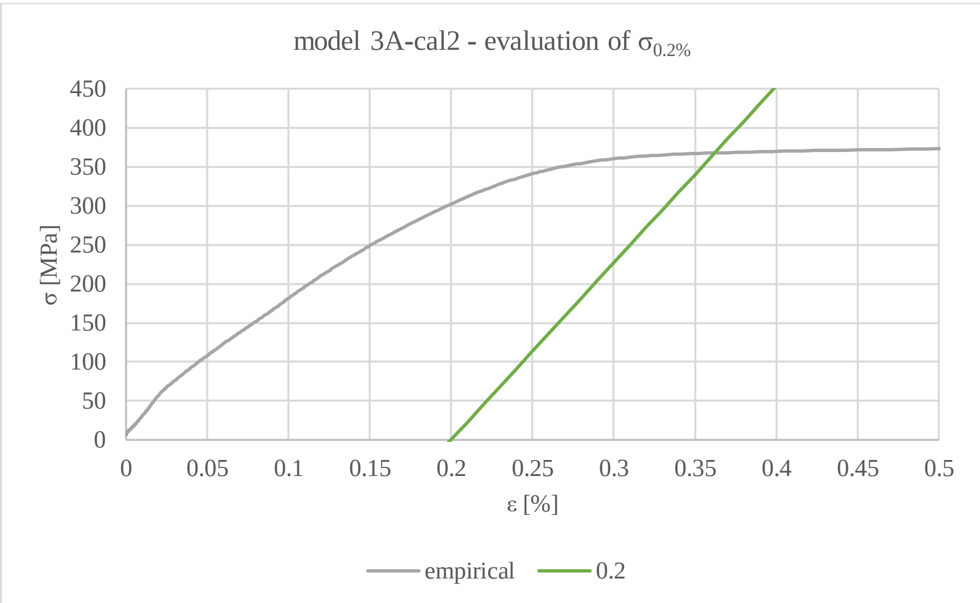

Figure 9.20 – Evaluation of 0.2% proof stress according to E_{cal1}

In Table 9.9 are reported the new values of the parameters defining the model.

Figure 9.21 shows the consequently updated true stress-true plastic strain diagram, whose key values are reported in Table 9.10, which lists the input parameters for the corresponding Abaqus model.

		values	
model	**parameter**	**3A**	**3A-cal2**
Ramberg-Osgood	n [-]	24,43	39,07
Rasmussen	E_y [MPa]	7 380	4 550
	m [-]	3,22	3,12
Hollomon	n_1 [-]	0,26	0,26
	K_1 [MPa]	1 104	1 104

Table 9.9 – Parameters defining the stress-strain model – 3A vs 3A-cal2

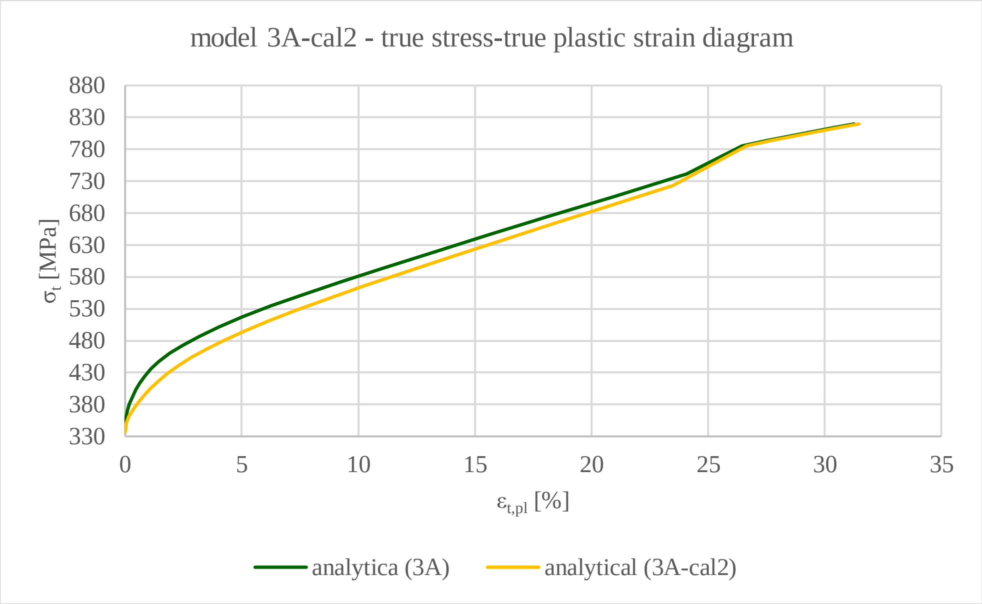

Figure 9.21 – True stress-true plastic strain curve – model 3A-cal2

		input values			
phase	**significant steps**	**E [MPa]**	**ν [-]**	**σ_t [MPa]**	**$\varepsilon_{t,pl}$ [-]**
elastic	-	226 870	0,44	-	-
plastic	0.01%	-	-	337,006	0
	0.2%	-	-	364,298	0,0020
	necking	-	-	777,790	0,2566
	failure	-	-	819,789	0,3147

Table 9.10 – Main input values in Abaqus for the characterization of material behavior – model 3A-cal2

Figure 9.22 reports the F-u plot obtained from model 3A-cal2, focusing on the yielding phase: while in the very first part, the new model provides slightly lower values than the experimental curve in terms of reaction forces, the curve quickly overestimates the target one.
Therefore, the value of $\sigma_{0.2\%}$ should be lower further; assuming a value of $\alpha_{0.2,cal2}$ to be applied to $\sigma_{0.2\%,cal2}$ equal to 0,98, $\sigma_{0.2\%,cal3}$ = 355,73 MPa, evaluated as:

$$\sigma_{0.2\%,cal3} = \alpha_{0.2,cal2}\sigma_{0.2\%,cal2} \tag{9.26}$$

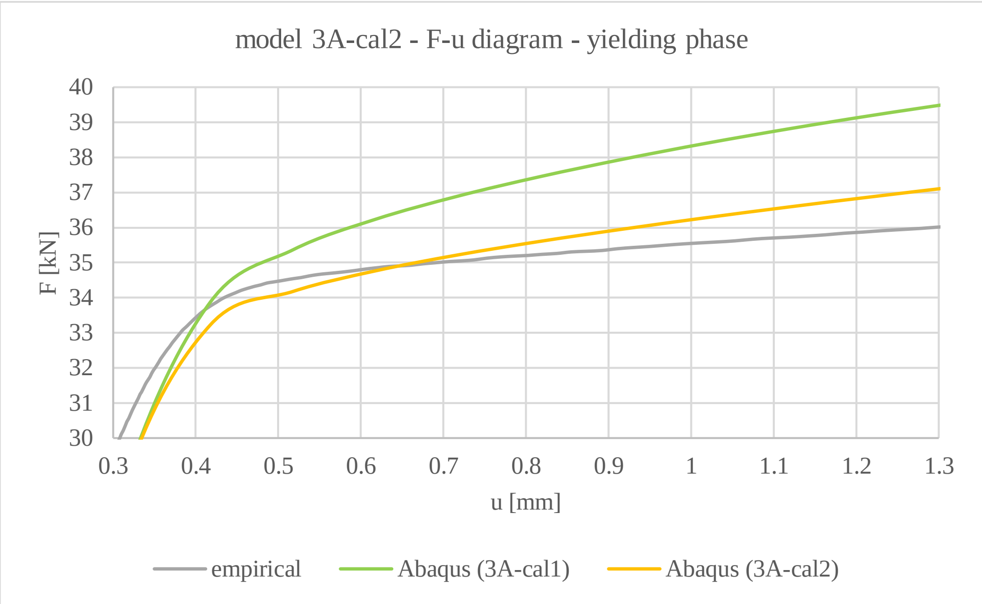

Figure 9.22 – F-u diagram: yielding phase – model 3A-cal2

Model 3A-cal3 is characterized by a new set of parameters for the definition of the stress-strain behavior; the values for said parameters are reported in Table 9.11.
Figure 9.23 plots the true stress-true plastic strain diagram, corresponding to the characterization of the plastic behavior of the material; the input values set in software Abaqus for this latest model are reported in Table 9.12.

		values	
model	**parameter**	**3A-cal2**	**3A-cal3**
Ramberg-Osgood	n [-]	39,07	53,05
Rasmussen	E_y [MPa]	4 550	3 300
	m [-]	3,12	3,08
Hollomon	n_1 [-]	0,26	0,26
	K_1 [MPa]	1 104	1 104

Table 9.11 – Parameters defining the stress-strain model – 3A-cal2 vs 3A-cal3

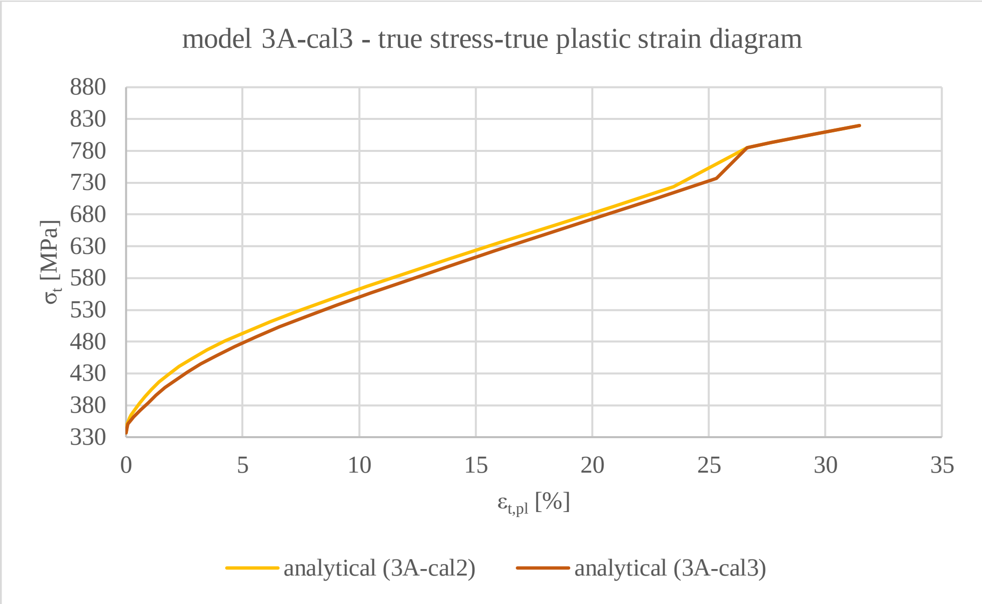

Figure 9.23 – True stress-true plastic strain curve – model 3A-cal3

phase	**significant steps**	**input values**			
		E [MPa]	**ν [-]**	**σ_t [MPa]**	**$\varepsilon_{t,pl}$ [-]**
elastic	-	226 870	0,44	-	-
plastic	0.01%	-	-	337,006	0
	0.2%	-	-	357,000	0,0020
	necking	-	-	777,790	0,2566
	failure	-	-	819,789	0,3147

Table 9.12 – Main input values in Abaqus for the characterization of material behavior – model 3A-cal3

The output F-u diagram is reported in Figure 9.24, with a focus on the yielding phase: the curve slightly underestimates the reaction force at yielding of about 1 kN, which is a valid result, being on the safe side, and then proceeds to tend to the target curve. Therefore, model 3A-cal3 is considered to be the calibrated model for specimen 3A.

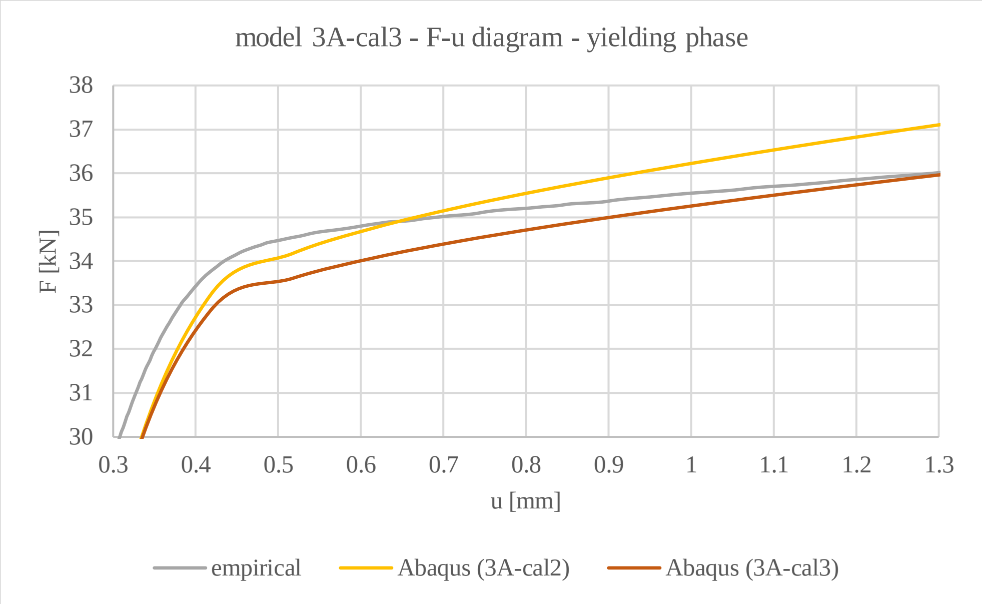

Figure 9.24 – F-u diagram: yielding phase – model 3A-cal3

9.3.6 Results' overview

The overall calibration of the stress-strain model for rough longitudinal specimen 3A is indicated in Table 9.13 below, in terms of calibrating factors α_E and $\alpha_{0.2}$.

Regarding the specimen's response, Figure 9.25 provides an overview of the F-u plot from a graphical point-of-view, while Figure 9.26 offers a close-up on the elastic and yielding phases, focus of the performed calibrations.

Table 9.14 reports the maximum values in terms of displacement and reaction force: it is evident how the model's calibration also impacted the maximum response reached during the software simulation.

	values [MPa]		
property	**initial**	**calibrated**	**α**
Young's modulus E	146 174	226 870	1,552
0.2% proof stress $\sigma_{0.2\%}$	380,05	355,73	0,936

Table 9.13 – Calibrating factors α – specimen 3A

	u_{max} [mm]	**F_{max} [kN]**
initial model	39,34	55,86
calibrated model	47,42	55,73
experimental	52,58	56,25

Table 9.14 – Maximum values for F-u – calibrated model for specimen 3A

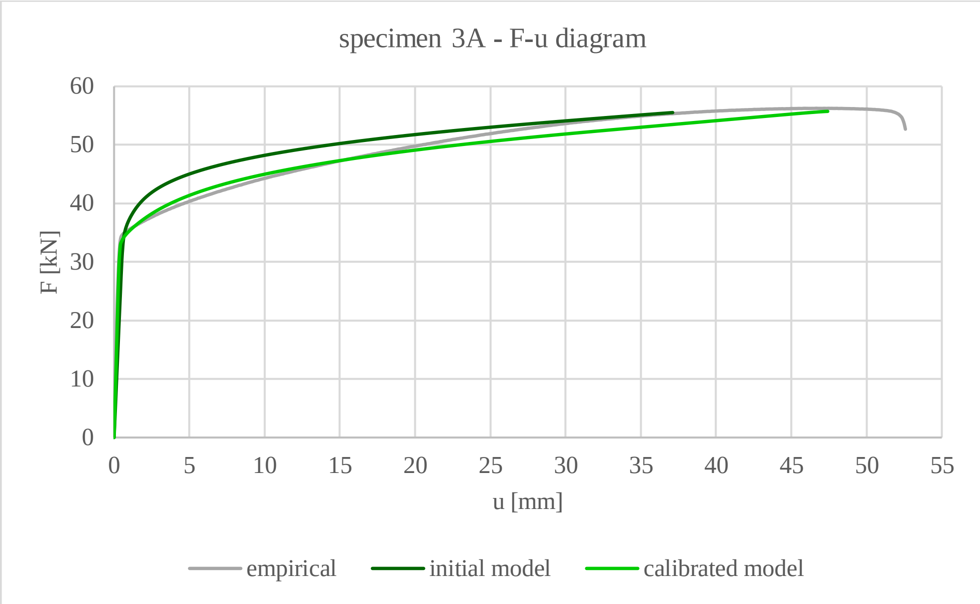

Figure 9.25 – F-u diagram – calibrated model for specimen 3A

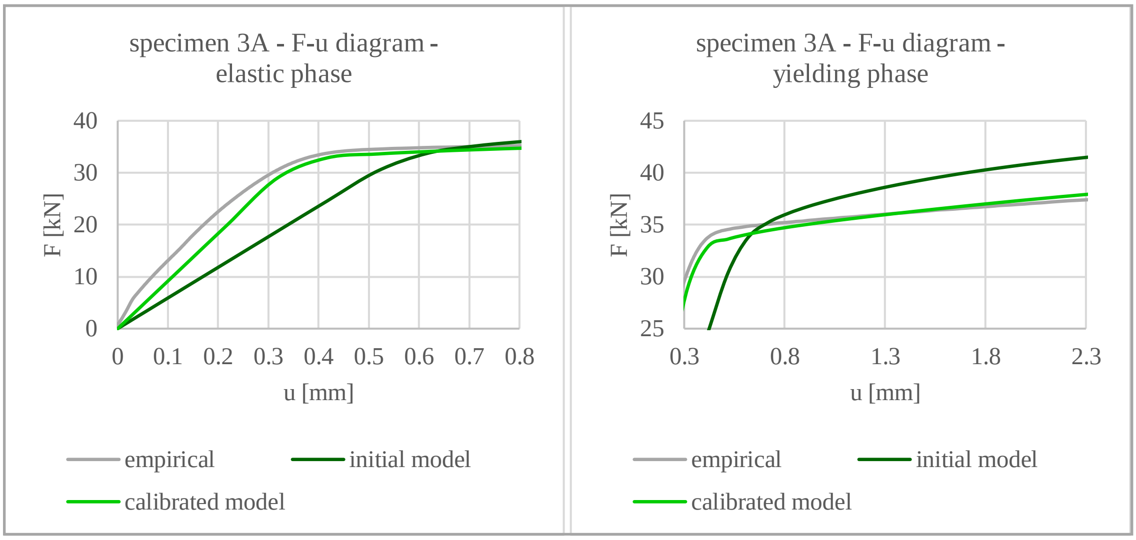

Figure 9.26 – F-u diagram: elastic and yielding phases – calibrated model for specimen 3A

9.4 Specimen 4D

9.4.1 Characterization of the stress-strain model

As for specimen 3A, the values of the mechanical parameters have been obtained from a Digital Image Correlation (DIC) analysis; in particular, Young's modulus E is extracted by means of Ordinary Least-Square Regression (OLSR), and consequently, 0.01% and 0.2% proof stresses can be evaluated as shown in Figure 9.27.

All significant mechanical properties are reported in Table 9.15.

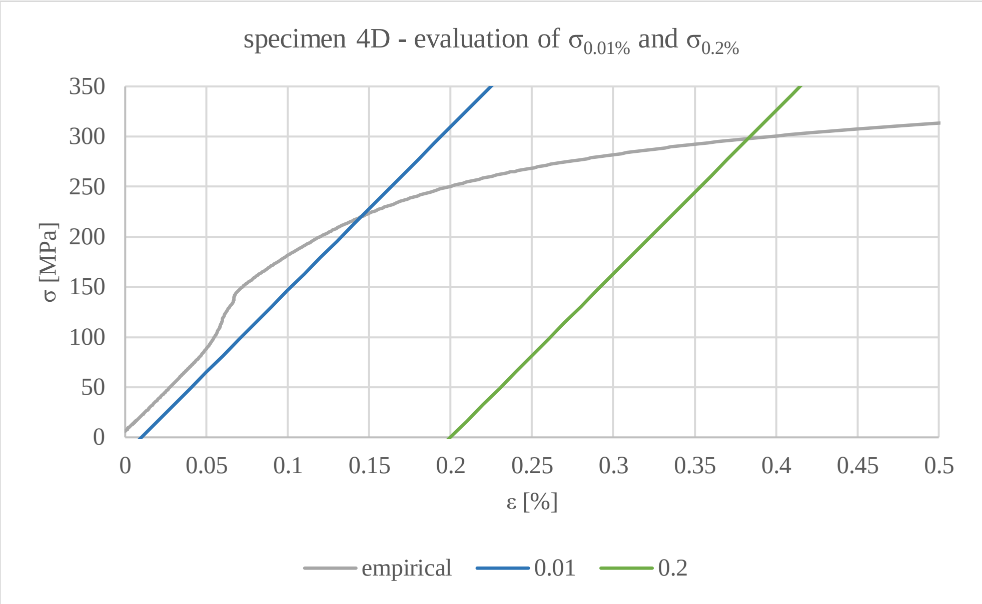

Figure 9.27 – Evaluation of 0.01% and 0.2% proof stresses of specimen 4D

property	**symbol**	**value**	**unit**
Young's modulus	E	162 997	MPa
0.01% proof stress	$\sigma_{0.01\%}$	228,20	MPa
0.2% proof stress	$\sigma_{0.2\%}$	293.39	MPa
ultimate stress	σ_u	555,19	MPa
yielding strain	ε_y	0,356	%
ultimate strain	ε_u	24,10	%
strain at failure	ε_f	25,06	%

Table 9.15 – Mechanical properties of specimen 4D

Table 9.16 below reports all the parameters defining the stress-strain model for specimen 4D, according to the models listed in Table 9.1.

It can be noticed how, in this particular case, the value of the true strain at necking is 26%, which is actually larger than the true strain at failure ε_f, which is equal to 22,36%, according to (9.13). The model is still valid, and this peculiarity can simply be associated to an oddly premature failure of the specimen in question.

model	**phase**	**parameter**	**value**	**unit**
Ramberg-Osgood	elastic	n	11,92	-
Rasmussen	plastic (pre-necking)	E_y	11 440	MPa
		m	2,85	-
Hollomon	post-necking	n_1	0,26	-
		K_1	1 022	MPa

Table 9.16 – Parameters defining the stress-strain model of specimen 4D

Figure 9.28 reports experimental engineering and true stress-strain diagrams, together with the analytical ones, namely those resulting applying the models as defined in Table 9.16.

Furthermore, empirical and analytical constitutive curves in terms of true values are plotted in Figure 9.29.

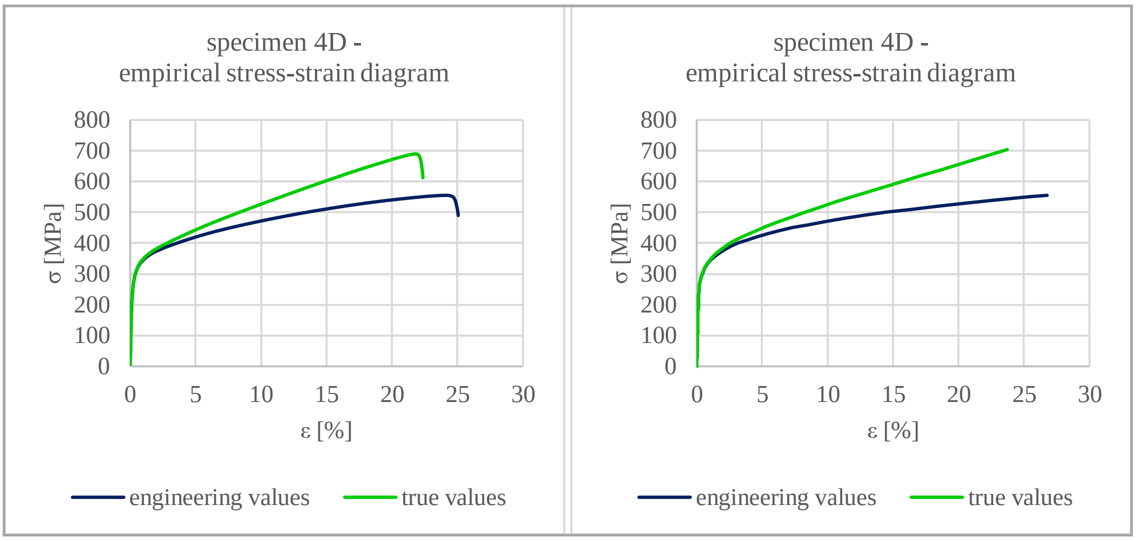

Figure 9.28 – Empirical and analytical engineering and true stress-strain curves of specimen 4D

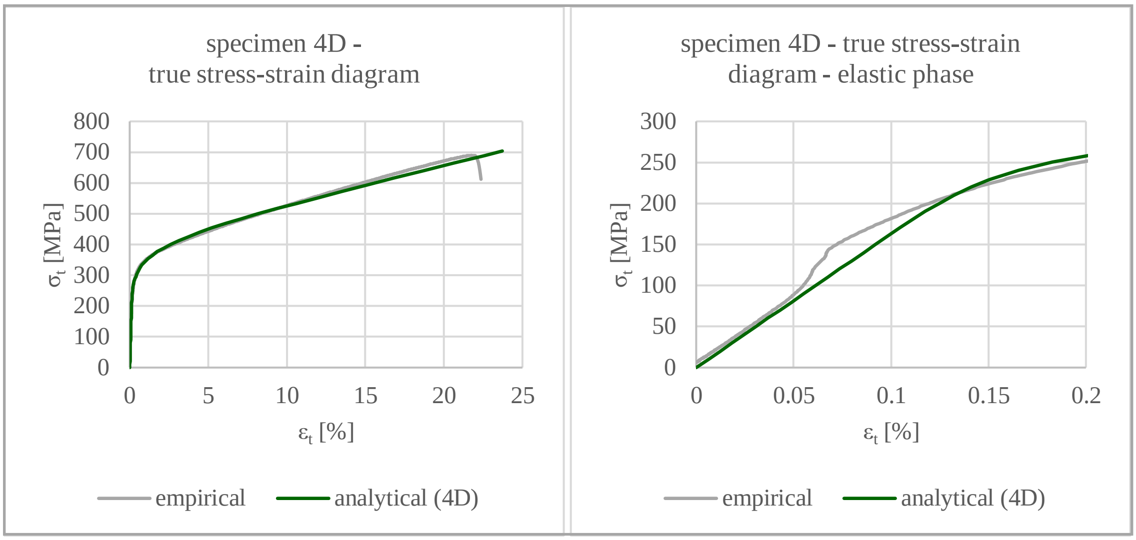

Figure 9.29 – Comparison between empirical and analytical true stress-strain curves of specimen 4D

9.4.2 Definition of the Finite Model in software Abaqus

A 3D scan of specimen 4D was provided, hence standing as a Digital Twin of the specimen itself; for this reason, the geometry within the software was simply determined through the importation of the 3D scan. Figure 9.2 shows a view from the top, as well as a side view, of specimen 4D.

As already explained for specimen 3A, within the software, the material is defined in terms of elastic behavior, by setting Young's modulus E and Poisson's ratio ν, and in terms of plastic behavior, by providing a set of yield stress-plastic strain values, starting from the 0.01% proof stress, which represents the transition between elastic and yielding phases.
These input values are partly reported in Table 9.17, and, regarding the plastic phase, entirely represented in Figure 9.30.

phase	significant steps	input values			
		E [MPa]	**ν [-]**	**σ_t [MPa]**	**$\varepsilon_{t,pl}$ [-]**
elastic	-	162 997	0,33	-	-
plastic	0.01%	-	-	228,538	0
	0.2%	-	-	294,509	0,0020
	failure	-	-	703,799	0,2329

Table 9.17 – Main input values in Abaqus for the characterization of material behavior – model 4D

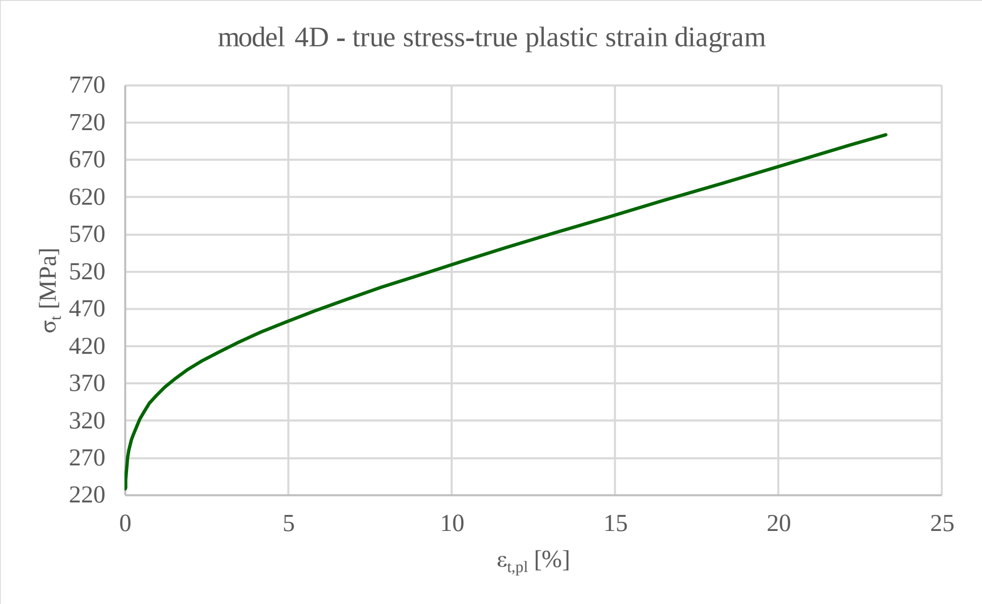

Figure 9.30 – True stress-true plastic strain curve – model 4D

The element is discretized by setting an approximate global size for the seeds of 2 mm, and employing C3D10-type elements (Figure 9.10), which are the most suitable choice for such a complex geometry. The resulting mesh presents 217437 nodes and 143559 elements.

As for specimen 3A, a “loading” step is created, characterized by a Tabular Amplitude relating displacements and time at a 1-to-1 rate. At this step, a displacement that linearly increases over time is applied in direction x.

In order to define boundary conditions, all the faces on each end are related by means of a multi-point constraint (MPC) and referred to a Control Point, to which boundary conditions are then assigned to.

The specimen is presented in Figure 9.31 at the loading step, while Figure 9.32 and Figure 9.33 focus, respectively, on the fixed and loaded ends. In particular, the fixed end is defined as an Encastre-type boundary, while the loaded end as a Displacement-type boundary, for which all displacements but that in the x directions are fixed.

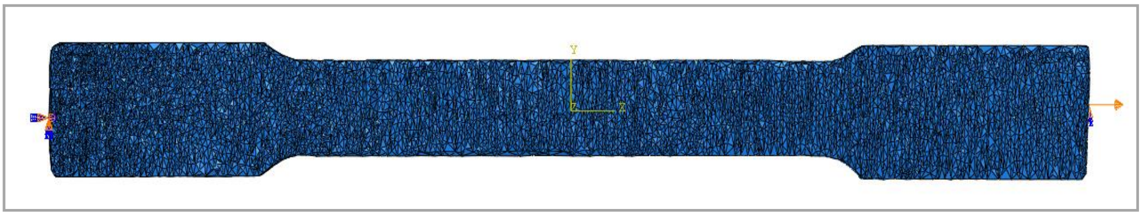

Figure 9.31 – Boundary conditions of model 4D – loading step

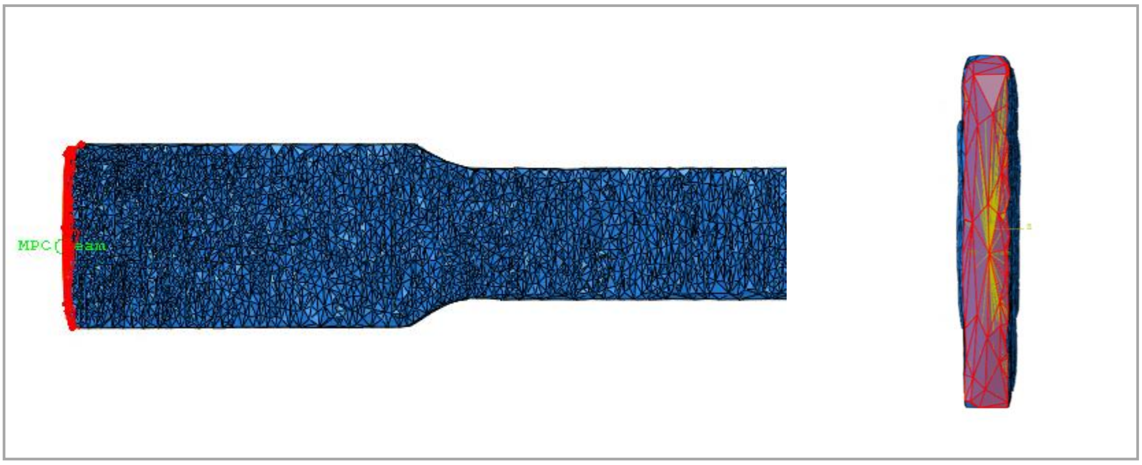

Figure 9.32 – Fixed-end of model 4D – xy and zy views

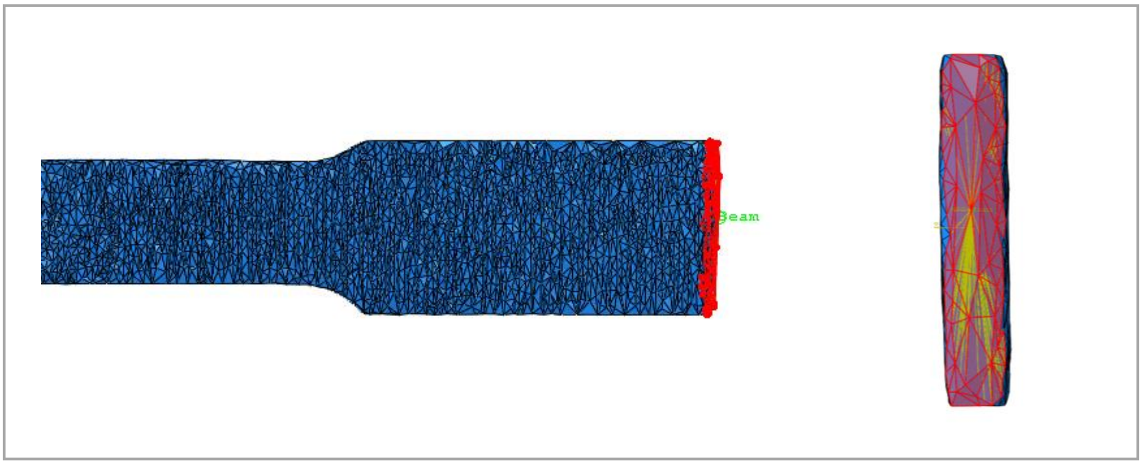

Figure 9.33 – Loaded-end of model 4D – xy and yz views

9.4.3 Results of FEA

Figure 9.34 shows the specimen at the initial stage, i.e. at rest, and at the elongation u_{max} reached at maximum reaction force F_{max}; these maximum values are reported in Table 9.18, in comparison with the target (experimental) ones. The resulting force-displacement diagram is plotted in Figure 9.35, again, compared to the empirical one.

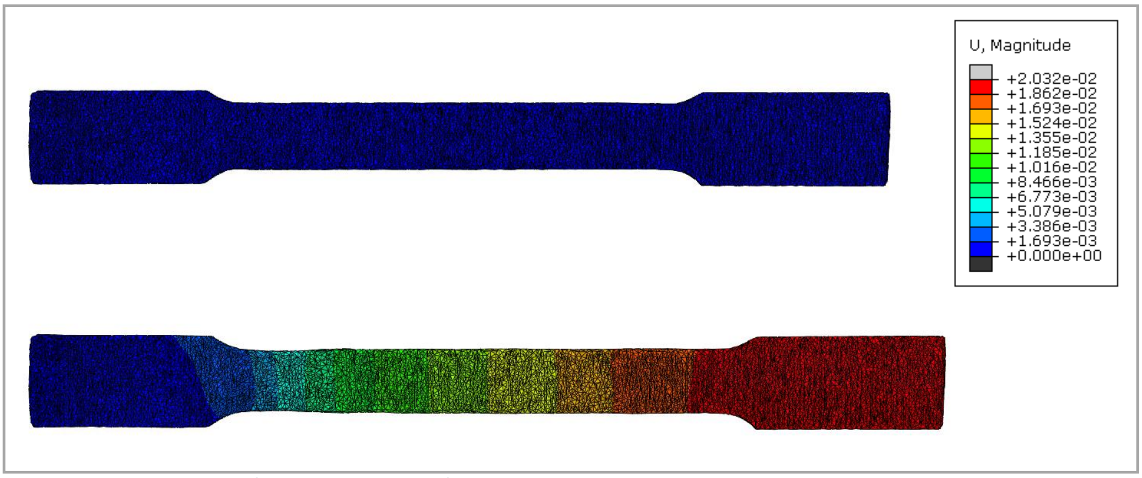

Figure 9.34 – Initial and final displacements from Abaqus – model 4D

	u_{max} [mm]	F_{max} [kN]
experimental	39,85	54,07
model 4D	19,92	56,22

Table 9.18 – Maximum values for F-u – model 4D

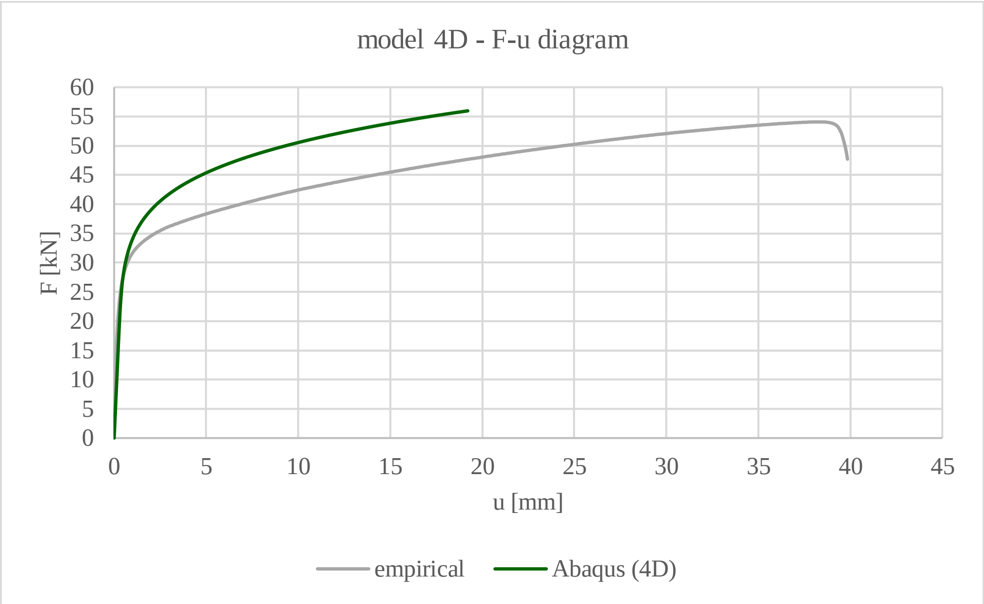

Figure 9.35 – F-u diagram – model 4D

9.4.4 Calibration of Young's modulus E

In order to calibrate the elastic phase, the focus must be on the value of Young's modulus E. Figure 9.36 compares analytical and experimental results in terms of force-displacement response, up to u = 0,8 mm, hence focusing on the elastic phase.

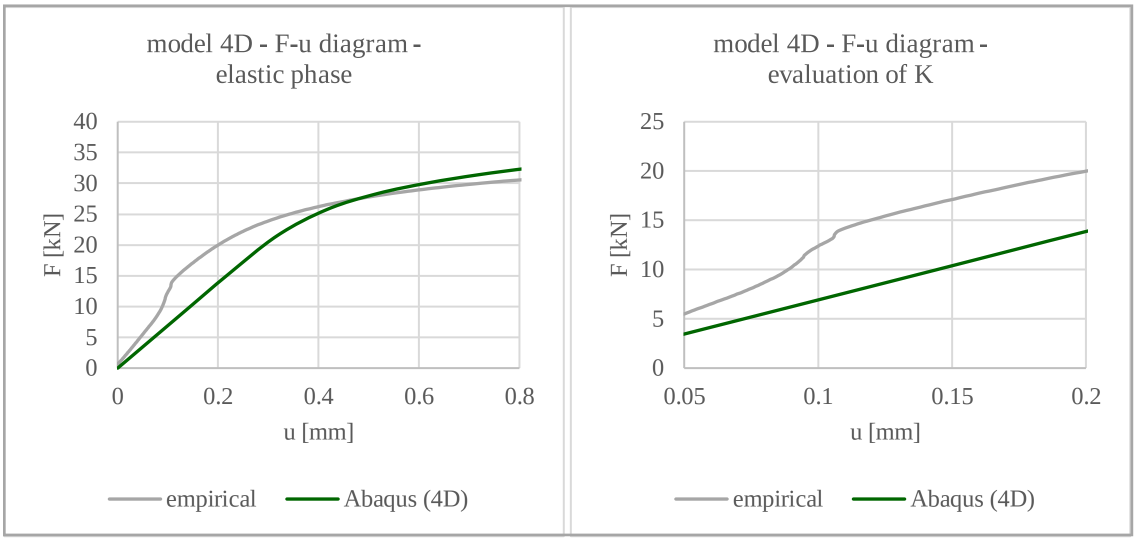

Figure 9.36 – F-u diagram: elastic phase – model 4D

Focusing on an interval that goes approximately from u = 0,05 mm to u = 0,25 mm, the target value of the axial stiffness is computed through linear interpolation, as reported in Table 9.19. The reference value for K is, therefore, K_{ref} = 88563,13 N/mm.

The value of the axial stiffness for the model is assessed on average on a series of F-u values, in between u = 0,010 mm and u = 0,218 mm.

These values are listed in Table 9.20, resulting in a value of K for the model equal to K_{4D} = 69151,37 N/mm.

	u [mm]	F [kN]	K [N/mm]
data	0,050369	5,5311	
	0,229277	21,376	
Δ	0,178908	15,845	
K_{ref}			88563,13

Table 9.19 – Evaluation of axial stiffness K – experimental (4D)

	u [mm]	F [kN]	K [N/mm]
data	0,010000	0,6911	69109,20
	0,020000	1,3824	69118,50
	0,035000	2,4196	69132,00
	0,057500	3,9762	69150,96
	0,091250	6,3124	69176,44
	0,141875	9,8190	69209,02
	0,217813	15,065	69163,46
K_{4D}			69151,37

Table 9.20 – Evaluation of axial stiffness K – model 4D

Exploiting equation (9.23) for K_{4D}, the calibrating factor is α_E = 1,281; consequently, according to (9.24), E_{cal1} = 208 753 N/mm. In terms of true stress-strain relationship in the plastic phase, the calibrated curve is plotted in Figure 9.37.

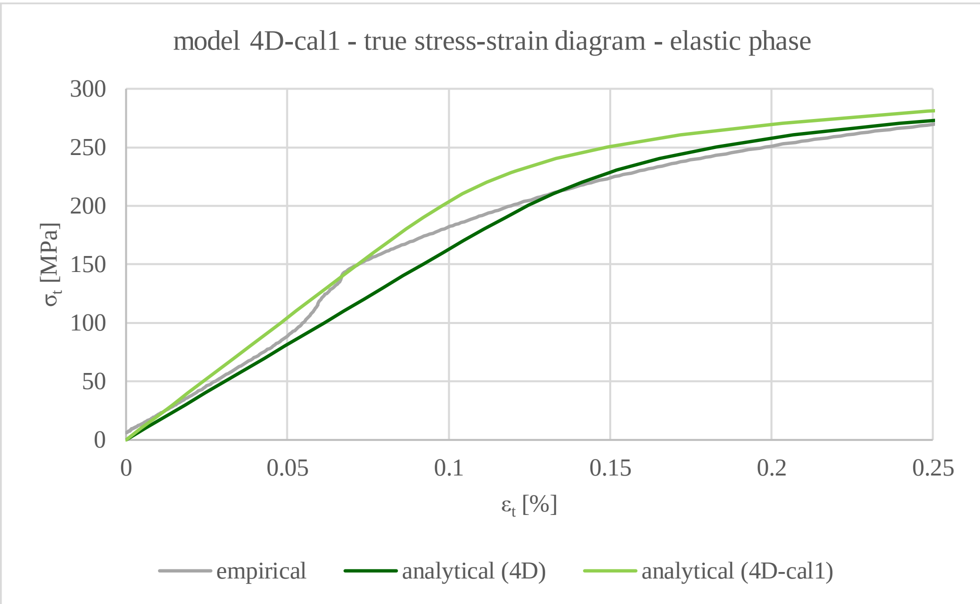

Figure 9.37 – σ-ε diagram: elastic phase – model 4D-cal1

The new calibrated model "4D-cal1" only presents changes in the elastic modulus, hence that is the only input value that changes with respect to Table 9.17. The resulting F-u diagram is plotted in Figure 9.38, focusing on the elastic phase and, in particular, in the reference interval chosen for the evaluation of axial stiffness K.

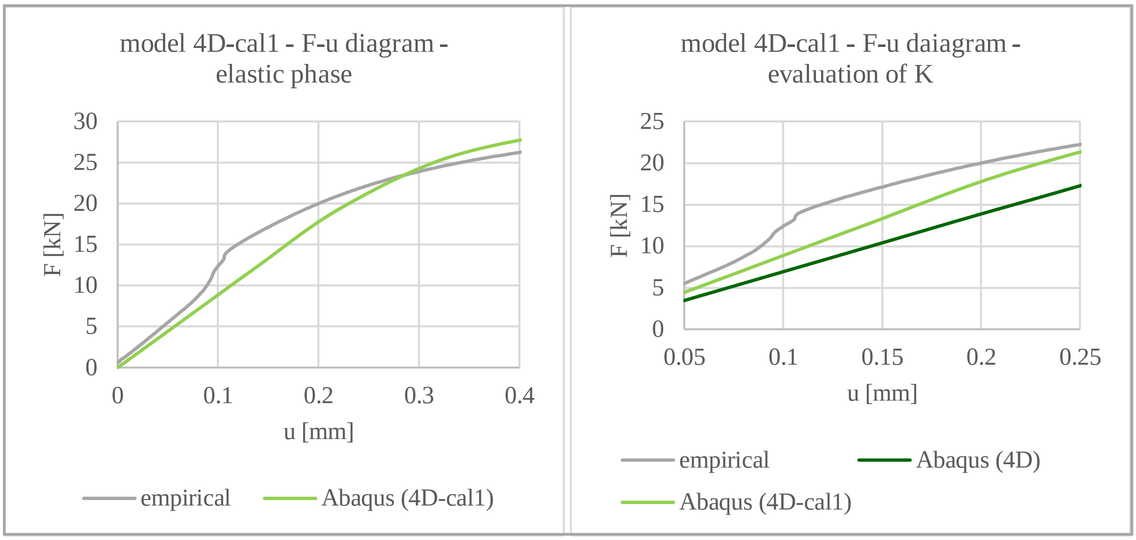

Figure 9.38 – F-u diagram: elastic phase – model 4D-cal1

Following the same approach for the evaluation of the axial stiffness used for model 4D, the resulting value is K_{cal1} = 88557,50 N/mm (Table 9.21); exploiting equation (9.24), the resulting value is $\alpha_{E,cal1}$ = 1,000. Therefore, model 4D-cal1 fairly approximates the elastic phase.

	u [mm]	**F [kN]**	**K [N/mm]**
data	0,010000	0,8851	88509,30
	0,020000	1,7704	88521,50
	0,035000	3,0989	88538,57
	0,057500	5,0924	88562,61
	0,091250	8,0843	88594,85
	0,141875	12,573	88618,15
K_{cal1}			88557,50

Table 9.21 – Evaluation of axial stiffness K – model 4D-cal1

9.4.5 *Calibration of 0.2% proof stress $\sigma_{0.2\%}$*

Following the same approach as for specimen 3A, the yielding phase is remodeled by calibrating the value of the 0.2% proof stress and maintaining that of the 0.01% proof stress. Figure 9.39 focuses on the yielding phase in the F-u diagram for model 4D-cal1.

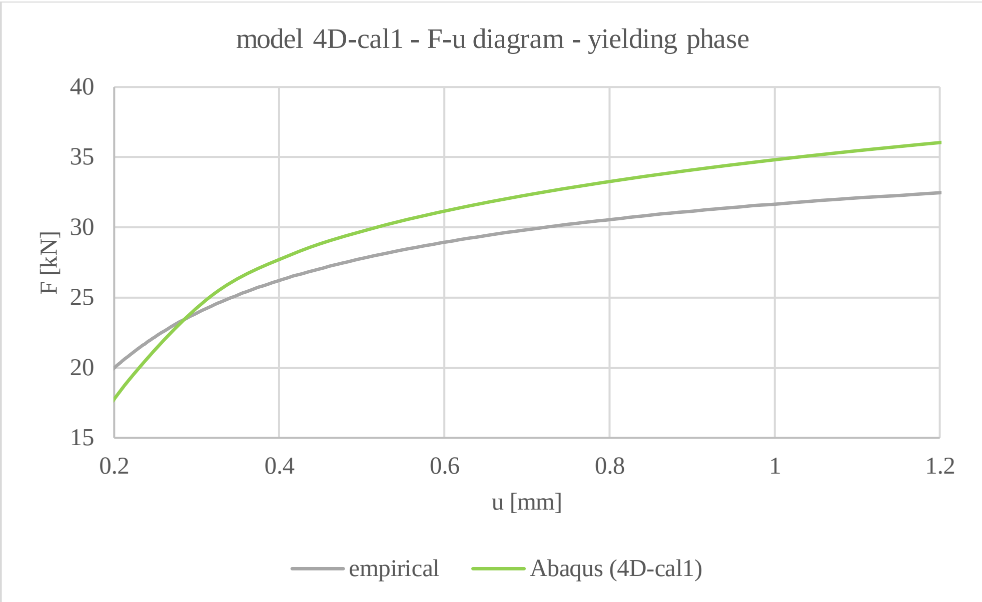

Figure 9.39 – F-u diagram: yielding phase – model 4D-cal1

The value of $\sigma_{0.2\%,cal2}$ for model 4D-cal2 is evaluated from Figure 9.40, assuming the calibrated value of the Young's modulus, namely E_{cal1} = 208 753 N/mm.

As a result, $\sigma_{0.2\%,cal2}$ = 292,25 MPa, which, if normalized with respect to the initial value $\sigma_{0.2\%,4D}$ = 293,39 MPa, sets the calibration factor at $\alpha_{0.2}$ = 0,996.

As the calibrated value is very similar to the initial one, so will be the results; hence, a new model "4D-cal3" can be introduced, assuming to further calibrate the value of $\sigma_{0.2\%,cal2}$ by means of a factor $\alpha_{0.2,cal2}$ = 0,90, resulting in $\sigma_{0.2\%,cal3}$ = 263,03 MPa.

The set of parameters corresponding to model 4D-cal3 are reported in Table 9.22, which also displays the similarities between models 4D-cal1 and 4D-cal2, especially in terms of n, highlighting why it makes sense to assume a new model right away.

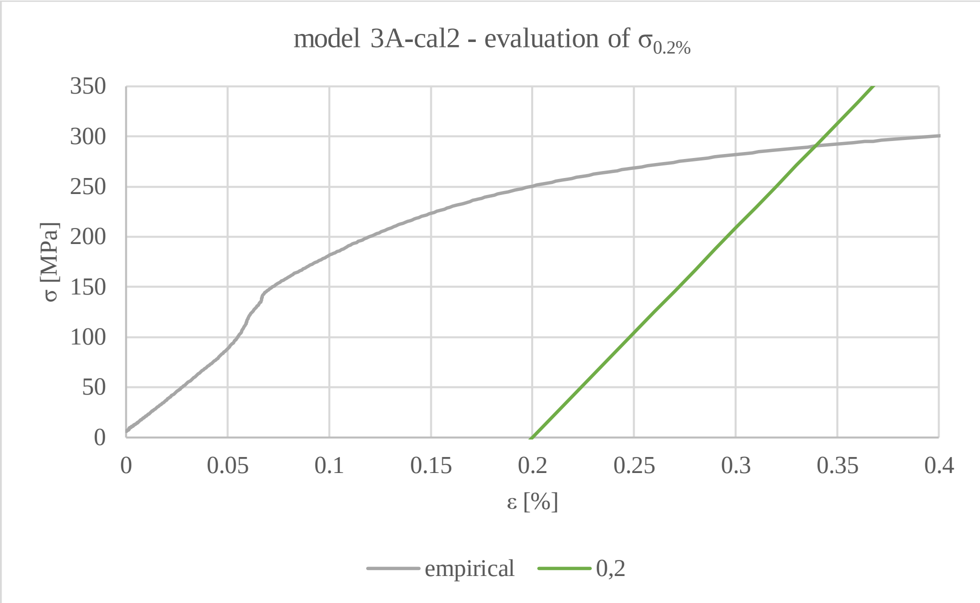

Figure 9.40 – Evaluation of 0.2% proof stress according to E_{cal1}

		values		
model	**parameter**	**4D-cal1**	**4D-cal2**	**4D-cal3**
Ramberg-Osgood	n [-]	11,92	12,11	21,09
Rasmussen	E_y [MPa]	11 620	11 410	6 060
	m [-]	2,85	2,84	2,66
Hollomon	n_1 [-]	0,26	0,26	0,26
	K_1 [MPa]	1 022	1 022	1 022

Table 9.22 – Parameters defining the stress-strain model – 4D-cal1 vs 4D-cal2 vs 4D-cal3

Table 9.23 reports the main input values describing the material's behavior for model 4D-cal3; and, in particular, the true stress-true plastic strain model of the plastic phase is plotted in Figure 9.41.

		input values			
phase	**significant steps**	**E [MPa]**	**ν [-]**	**σ_t [MPa]**	**$\varepsilon_{t,pl}$ [-]**
elastic	-	208 753	0,33	-	-
plastic	0.01%	-	-	228,468	0
	0.2%	-	-	263,886	0,0020
	failure	-	-	717,561	0,2531

Table 9.23 – Main input values in Abaqus for the characterization of material behavior – model 4D-cal3

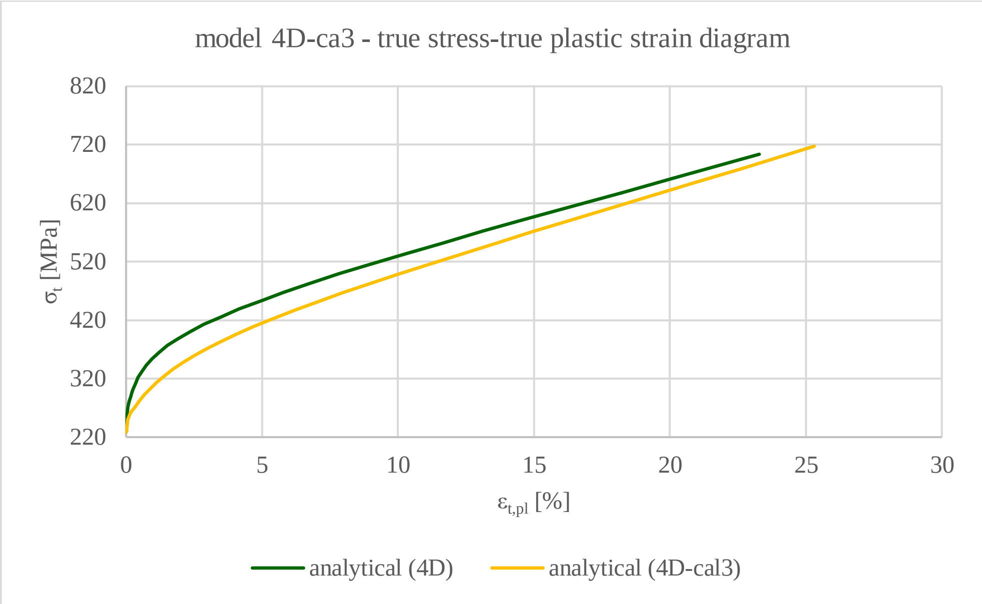

Figure 9.41– True stress-true plastic strain curve – model 4D-cal3

The output force-displacement diagram, with a focus on the yielding phase, is reported in Figure 9.42. As can be seen, while in the very first part the model behaves very similarly to the reference one, it soon quickly diverges from the target trend.

For this reason, the value of the 0.2% proof stress is further decreased of a factor 0,95, hence, for model 4D-cal4, $\sigma_{0.2\%,cal4}$ = 249,88 MPa.

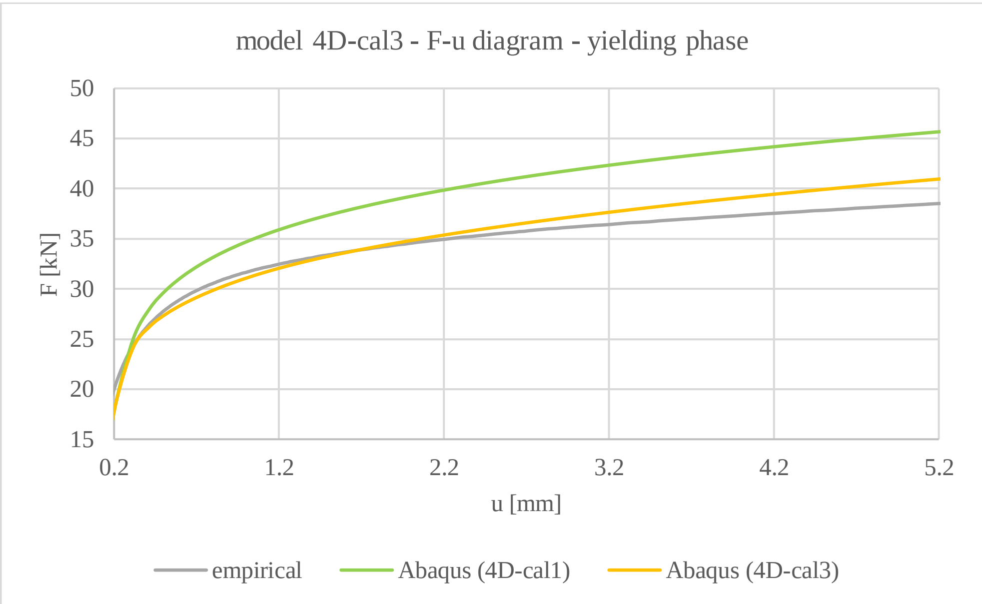

Figure 9.42 – F-u diagram: yielding phase – model 4D-cal3

The parameters defining the new stress-strain model 4D-cal4 are reported in Table 9.24, where they are compared to those of the previous model, i.e. 4D-cal3.

The resulting plastic behavior in terms of true stresses and true plastic strains is shown in Figure 9.43, and the key values, which are put inside software Abaqus to characterize the new material, are reported in Table 9.25.

		values	
model	**parameter**	**3A-cal3**	**3A-cal4**
Ramberg-Osgood	n [-]	21,09	33,01
Rasmussen	E_y [MPa]	6 060	3 720
	m [-]	2,66	2,58
Hollomon	n_1 [-]	0,26	0,26
	K_1 [MPa]	1 022	1 022

Table 9.24 – Parameters defining the stress-strain model – 4D-cal3 vs 4D-cal4

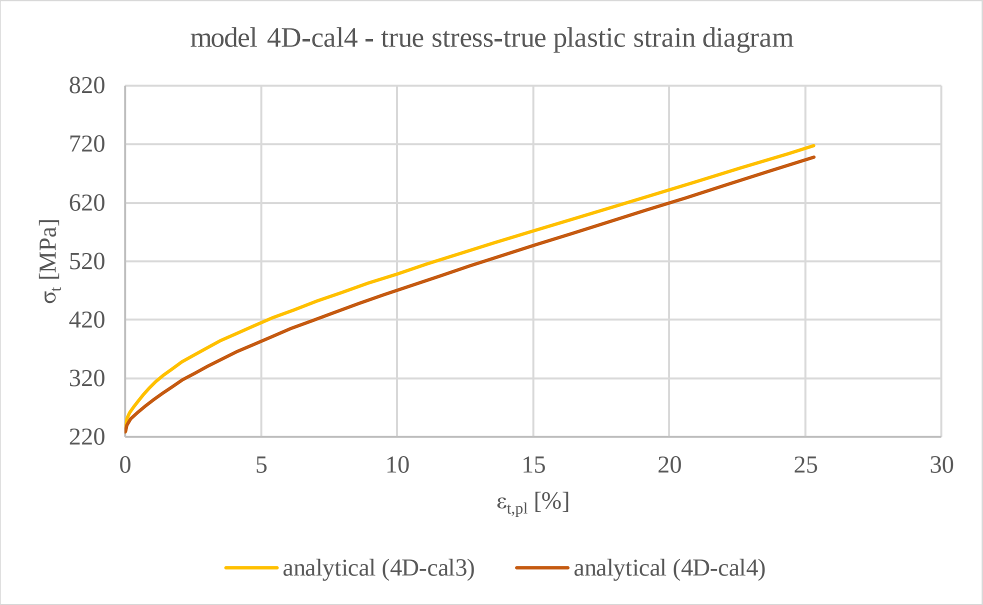

Figure 9.43 – True stress-true plastic strain curve – model 4D-cal4

		input values			
phase	**significant steps**	**E [MPa]**	**ν [-]**	**σ_t [MPa]**	**$\varepsilon_{t,pl}$ [-]**
elastic	-	208 753	0,33	-	-
plastic	0.01%	-	-	228,468	0
	0.2%	-	-	250,676	0,0020
	failure	-	-	736,325	0,2788

Table 9.25 – Main input values in Abaqus for the characterization of material behavior – model 4D-cal4

The force-displacement diagram resulting from the analysis run in software Abaqus, focused on the yielding phase, is reported in Figure 9.44. In the initial part, the force is about 2 kN lower than the empirical value; being it on the safe side, and given the fact that the diagram quickly approaches the target trend, it is a valid result.

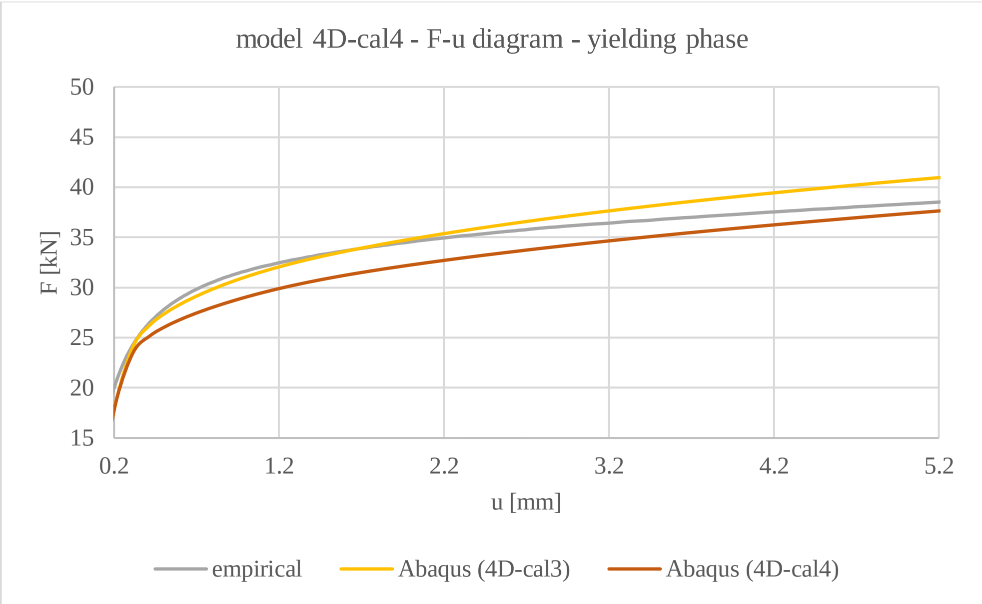

Figure 9.44 – F-u diagram: yielding phase – model 4D-cal4

9.4.6 Results' overview

Table 9.26 recapitulates the calibrating factors applied to the model for specimen 4D.

The overall response in terms of force vs displacement is shown in Figure 9.45, while Figure 9.46 focuses the attention, in particular, on the elastic and yielding phases, which were the core of the calibrations performed.

Finally, Table 9.27 lists and compares the maximum values in terms of reaction force and displacement reached during the actual test and in the simulations.

	values [MPa]		
property	**initial**	**calibrated**	**α**
Young's modulus E	162 997	208 753	1,281
0.2% proof stress $\sigma_{0.2\%}$	293,39	249,88	0,852

Table 9.26 – Calibrating factors α – specimen 4D

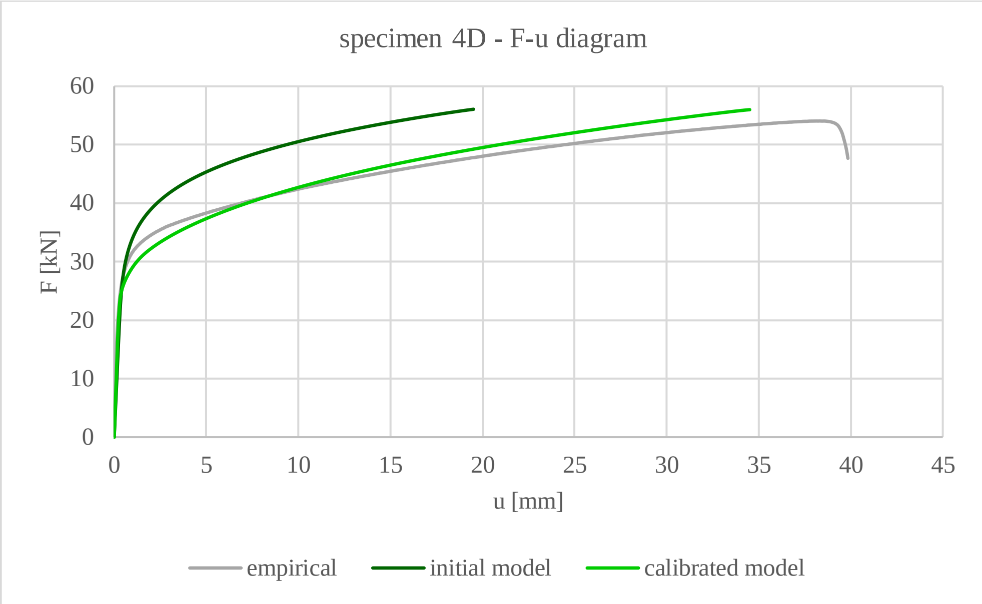

Figure 9.45 – F-u diagram – calibrated model for specimen 4D

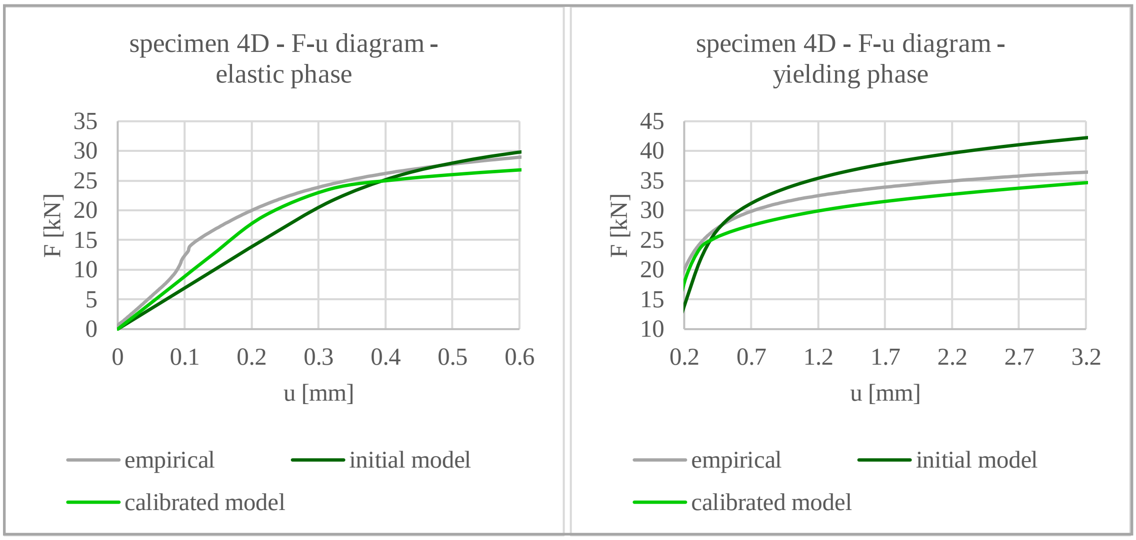

Figure 9.46 – F-u diagram: elastic and yielding phases – calibrated model for specimen 4D

	u_{max} [mm]	F_{max} [kN]
initial model	19,92	56,22
calibrated model	34,52	56,00
experimental	39,85	54,07

Table 9.27 – Maximum values for F-u – calibrated model for specimen 4D

10. Application of stress-strain models from milled specimens to rough Digital Twins

10.1 Overview

In Chapter 9, the stress-strain model applied to the respective Digital Twin was evaluated from the effective values proper of the same rough specimen. This approach aimed at the refinement of the mechanical behavior, removing to a certain extent the influence of the geometry on the values themselves. The response, though, is still affected by the geometry, in the sense that the "pure" stress-strain relationship is applied to a rough configuration.

Since, as just stated, the influence of the roughness is already accounted for in the Digital Twin's geometry, a different approach could be applying a stress-strain model evaluated from milled specimens, which can already be considered as the actual constitutive behavior of the WAAM-produced material, to the Digital Twin.

In particular, both for the longitudinal and the transversal direction, 5 milled specimens have been analyzed in order to produce an averaged "milled" stress-strain model; said specimens are the same considered in section 5.2 for the evaluation of the characteristic values of key mechanical properties.

10.2 Longitudinal direction

10.2.1 Stress-strain model

Following the same approach outlined in section 9.2, the stress-strain behavior can be modeled according to three different methods over three different phases. Specifically:

- Ramberg-Osgood's model characterizes the elastic phase, and in particular the trend between $\sigma_{0.01\%}$ and $\sigma_{0.2\%}$;
- Rasmussen's model defines the plastic behavior up until necking;
- Hollomon's model best describes the hardening caused by diffused necking.

The models and their characterizing parameters are summarized in Table 9.1, which is reported here below.

model	**phase**	**formulation**	**parameters**
Ramberg-Osgood	elastic	$\varepsilon = \frac{\sigma}{E} + 0.002\left(\frac{\sigma}{\sigma_{0.2\%}}\right)^n$	$n = \frac{\ln 20}{\ln\left(\frac{\sigma_{0.2\%}}{\sigma_{0.01\%}}\right)}$
Rasmussen	plastic (pre-necking)	$\varepsilon = 0.002 + \frac{\sigma_{0.2\%}}{E} + \frac{\sigma - \sigma_{0.2\%}}{E_y} + \varepsilon_u\left(\frac{\sigma - \sigma_{0.2\%}}{\sigma_u - \sigma_{0.2\%}}\right)^m$	$E_y = \frac{E}{1 + 0.002n\frac{E}{\sigma_{0.2\%}}}$ $m = 1 + 3.5\frac{\sigma_{0.2\%}}{\sigma_u}$
Hollomon	post-necking	$\sigma_t = K_1\varepsilon_t^{n_1}$	$n_1 = \frac{N\sum x_i y_i - \sum x_i \sum y_i}{N\sum x_i^2 - (\sum x_i)^2}$ $K_1 = \sigma_u\left(\frac{n_1}{e}\right)^{-n_1}$

Table 10.1 lists the main mechanical properties for 5 milled L specimens. Said properties, as for specimens 3A and 4D in chapter 9, have been extracted from Digital Image Correlation analyses, and, regarding Young's modulus E, by means of Ordinary Least Square Regression.
Their mean values characterize the material defining "model L".

Parameters n, E_y, m, n_1 and K_1 are then evaluated, as indicated in Table 9.1, for each one of the milled longitudinal specimens. Table 10.2 lists said values, their mean m (which define model L), standard deviation s and coefficient of variation V.

The stress-strain diagram describing model L is plotted in Figure 10.1, where it is compared to the effective constitutive relationships of the milled longitudinal specimens it was derived from, as well as that of specimen 3A.

property	unit	specimens				
		1 bis L	2 L	3 L	4 L	5 bis L
Young's modulus E	MPa	135 540	130 490	147 310	137 940	141 420
0.01% proof stress $\sigma_{0.01\%}$	MPa	211,02	252,50	310,82	229,18	260,65
0.2% proof stress $\sigma_{0.2\%}$	MPa	342,91	353,50	356,87	325,67	322,71
ultimate stress σ_u	MPa	549,10	549,07	580,28	592,34	551,56
yielding strain ε_y	%	0,505	0,447	0,455	0,481	0,458
ultimate strain ε_u	%	24,24	20,33	29,72	30,78	27,57
strain at failure ε_f	%	25,54	22,06	34,07	34,50	29,83

Table 10.1 – Mechanical properties of milled L specimens

	Ramberg-Osgood	Rasmussen		Hollomon	
	n [-]	E_y [MPa]	m [-]	n_1 [-]	K_1 [MPa]
1 bis L	6,17	23 060	3,19	0,23	969
2 L	8,90	17 231	3,25	0,21	940
3 L	21,68	7 794	3,15	0,24	1 039
4 L	8,53	16 776	2,92	0,27	1 105
5 bis L	14,03	10 638	3,05	0,24	988
m	11,86	15 100	3,11	0,24	1 008
s	5,54	5 367	0,115	0,018	58,17
V	0,467	0,355	0,037	0,077	0,058

Table 10.2 – Parameters defining the averaged stress-strain model for L milled specimens

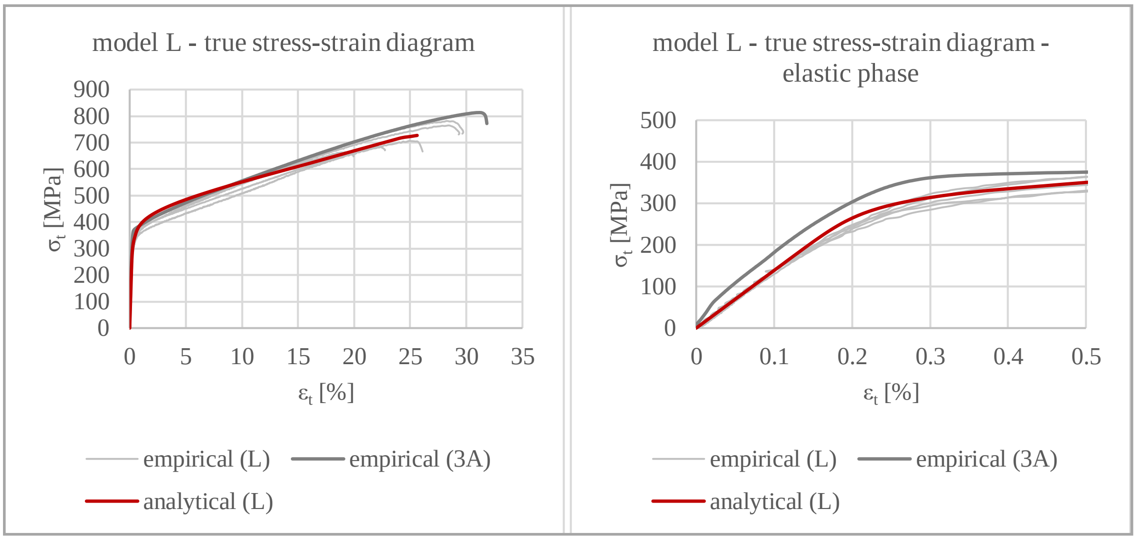

Figure 10.1 – Comparison between empirical and analytical true stress-strain curves of model L

10.2.2 Definition of the Finite Model in software Abaqus

The geometry, mesh and boundary conditions are the same as those defined in section 9.3.2, since the physical model remains unaffected by the new model, which only concerns the material's behavior.

Table 10.3 reports the main values set within the software for the characterization of the material. Furthermore, Figure 10.2 shows the entire plastic behavior in terms of true stress and true plastic strain, from $\sigma_{0.01\%}$ until failure, compared to model 3A (calibrated), which can be considered as a reference trend to aim to.

This graph shows that the overall plastic behavior has a similar trend to the reference one; the main discrepancies are found in an underestimated strength in the yielding phase, an overvalued one right after, and quite lower ductility and maximum strength.

		input values			
phase	**significant steps**	**E [MPa]**	**ν [-]**	**σ_t [MPa]**	**$\varepsilon_{t,pl}$ [-]**
elastic	-	138 450	0,44	-	-
plastic	0.01%	-	-	253,310	0
	0.2%	-	-	341,849	0,0020
	necking	-	-	715,667	0,2348
	failure	-	-	726,961	0,2509

Table 10.3 – Main input values in Abaqus for the characterization of material behavior – model L

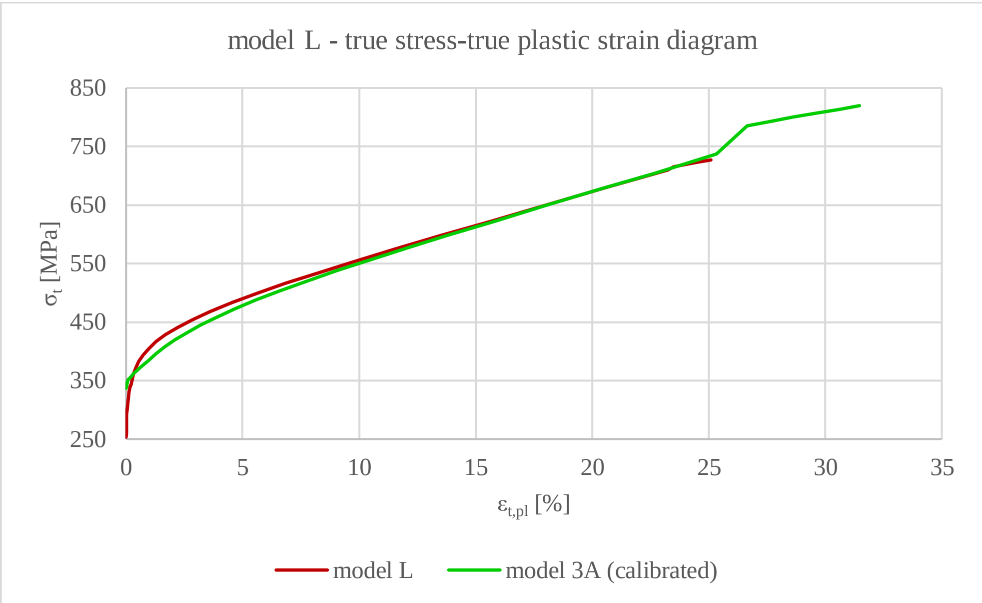

Figure 10.2 – True stress-true plastic strain curve – model L

10.2.3 Results of FEA

Figure 10.3 reports the response resulting from the simulation run in software Abaqus, in terms of reaction force vs displacement. This plot is visually compared to that of specimen 3A, and, in order to generalize, to those of a set of longitudinal rough specimens. The F-u diagram of specimen 3A can qualitatively be considered a fair average of the response of the rough specimens tested.

The considerations made on the true stress-true plastic strain plot in section 10.2.2 find some correspondence in terms of F-u: as expected, at yielding, the behavior is initially underestimated, and surpasses the target one later on; the maximum value of the force is lower than the empirical one, and so is the respective displacement, as reported numerically in Table 10.4.

The evaluation of the plastic phase will remain only qualitative in this study, while the elastic phase is more thoroughly analyzed in section 10.2.4.

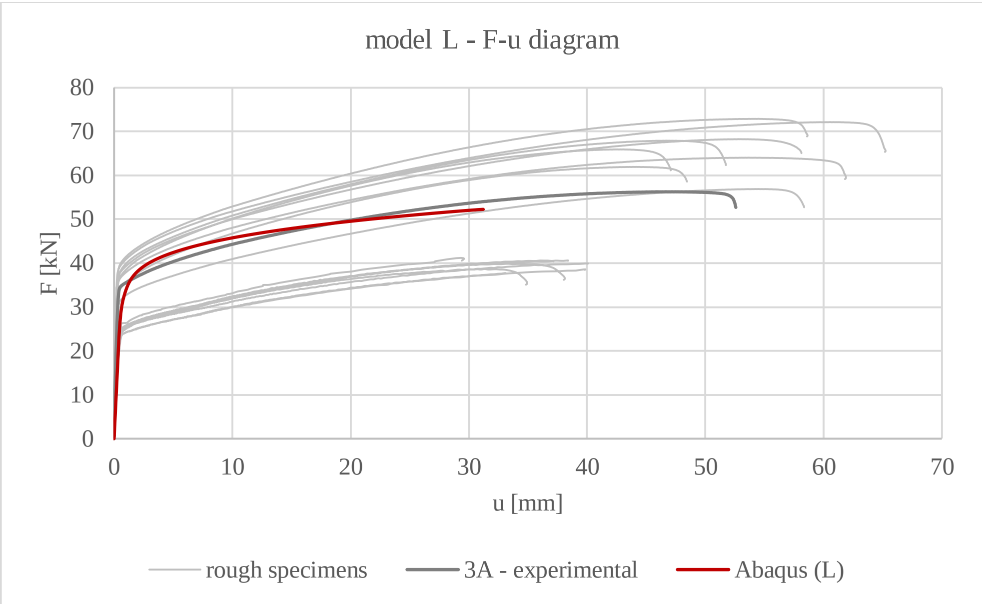

Figure 10.3 – F-u diagram – model L

	u_{max} [mm]	F_{max} [kN]
rough specimens (average)	46,27	52,87
3A - experimental	52,58	56,25
model L	31,22	52,24

Table 10.4 – Maximum values for F-u – model L

10.2.4 Analysis of the elastic phase

Focusing on the elastic phase, Figure 10.4 plots the F-u diagram resulting from the simulation of model L up until u = 0,6 mm, compared to the reference response (3A-experimental) and a set of responses of rough longitudinal specimens. In order to better evaluate the axial stiffness, a further close-up is offered for the interval in between u = 0,05 mm and u = 0,25 mm, only in contrast with specimen 3A.

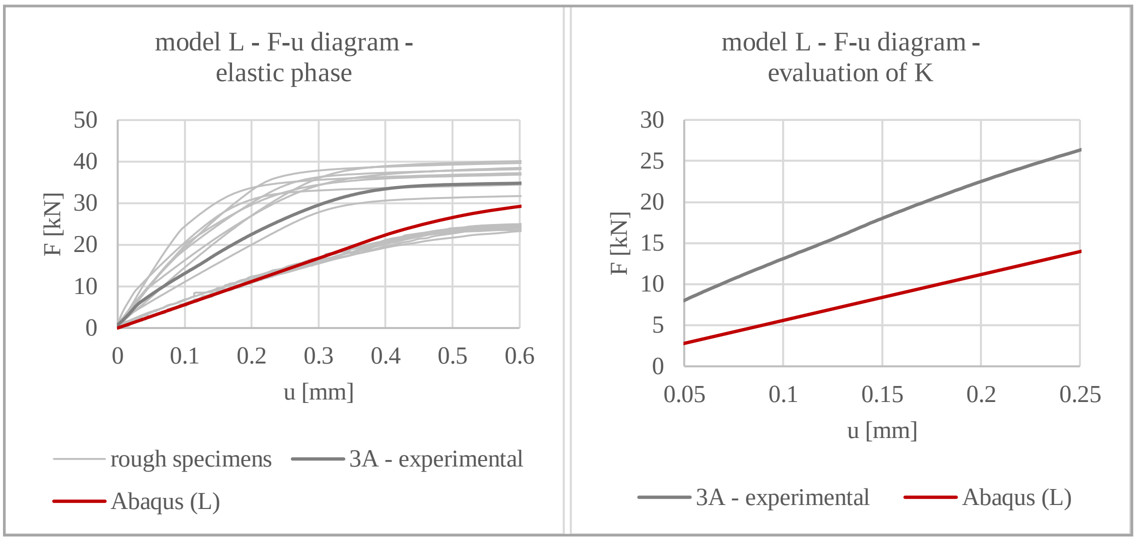

Figure 10.4 – F-u diagram: elastic phase – model L

It is clear how the actual axial stiffness K_{ref} of specimen 3A is quite larger than the one obtained from the model. In particular, recalling Table 9.6, the value of K_{ref} is 91530,35 N/mm.

The axial stiffness characterizing the response of model L is evaluated on average over a set of (u,F) values, in between u = 0,010 mm and u = 0,218 mm, computing each value of K according to equation (9.4), i.e. as:

$$K = \frac{F}{u} \tag{10.1}$$

Therefore, model L is characterized by an axial stiffness K_L = 55893,99 N/mm, as indicated in Table 10.5. The calibrating factor for the axial stiffness, which will be applied to the Young's modulus of model L-cal, is computed according to expression (9.23), resulting in $\alpha_{E,L}$ = 1,638; hence, the calibrated value of E applied to model L-cal is E_{cal} = 226 869 MPa.

Figure 10.5 reports the corresponding stress-strain plot.

	u [mm]	F [kN]	K [N/mm]
data	0,010000	0,5590	55898,80
	0,020000	1,1180	55899,50
	0,035000	1,9565	55899,43
	0,057500	3,2142	55898,78
	0,091250	5,1005	55896,11
	0,141875	7,9294	55889,83
	0,217813	12,170	55875,45
K_L			55893,99

Table 10.5 – Evaluation of axial stiffness K – model L

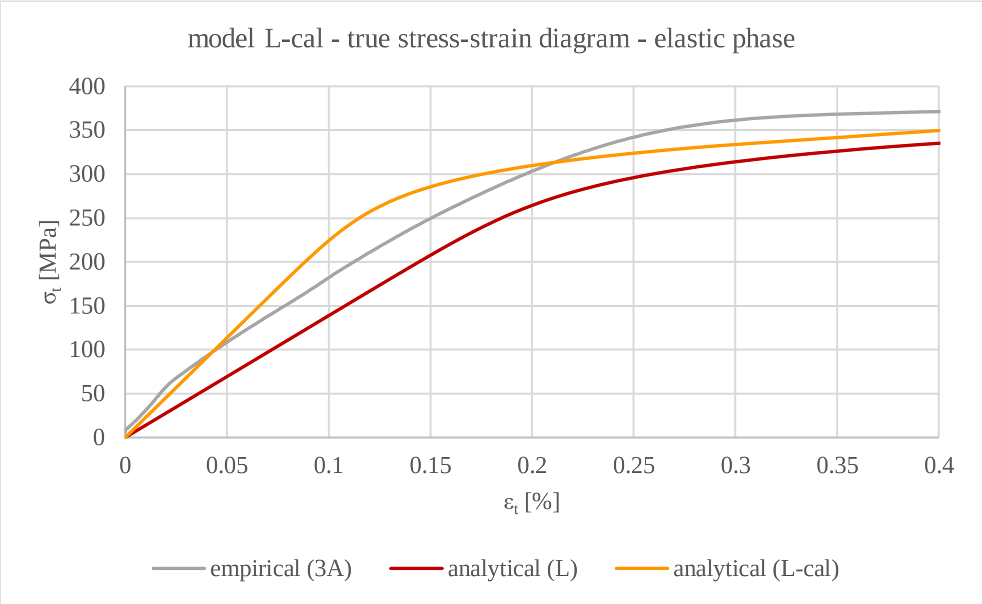

Figure 10.5 – σ-ε diagram: elastic phase – model L-cal

Changing the input value of E in software Abaqus from model L, while maintaining the same plastic phase, model L-cal is defined within the simulation. After running the static analysis, the outputs in terms of reaction force vs displacement, for the elastic phase, as reported in Figure 10.6, with emphasis on the chosen reference interval for the evaluation of K.

In order to check whether the calibrated axial stiffness correctly models the target one, it is again computed on average, for displacements in the reference interval 0,010-0,218 mm, as reported in Table 10.6. The resulting value is $K_{L,cal}$ = 91519,19 N/mm; normalizing the reference value K_{ref} with respect to $K_{L,cal}$, $\alpha_{E,L\text{-}cal}$ = 1,000, hence the calibration is reasonable.

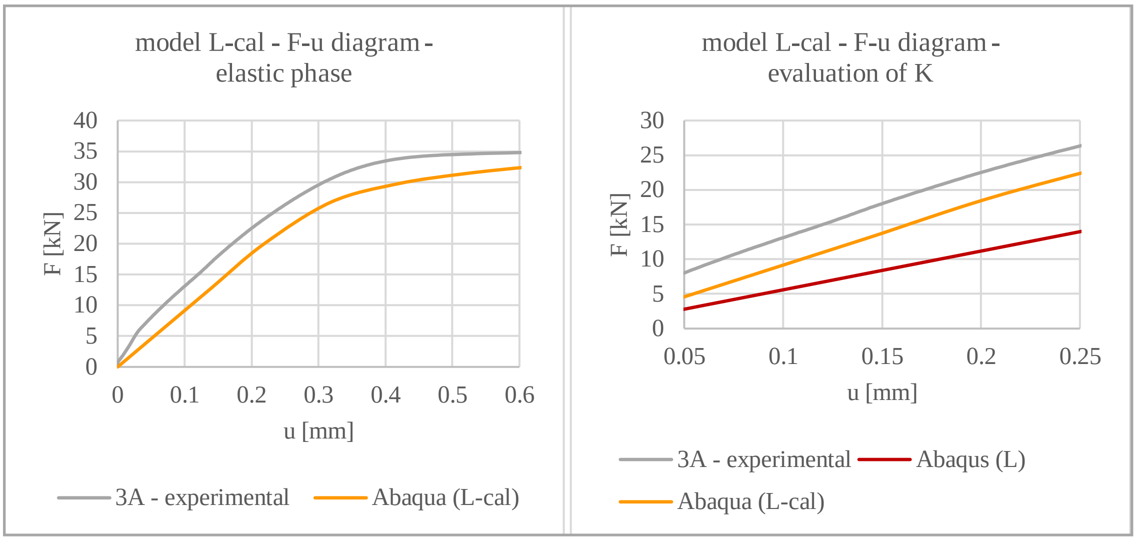

Figure 10.6 – F-u diagram: elastic phase – model L-cal

	u [mm]	**F [kN]**	**K [N/mm]**
data	0,010000	0,9154	91538,30
	0,020000	1,8308	91539,00
	0,035000	3,2039	91539,43
	0,057500	5,2634	91538,09
	0,091250	8,3524	91533,48
	0,141875	12,984	91517,18
	0,217813	19,914	91428,89
$K_{L,cal}$			91519,19

Table 10.6 – Evaluation of axial stiffness K – model L-cal

10.3 Transversal direction

10.3.1 Stress-strain model

The stress-strain behavior is, again, described by Ramberg-Osgood's, Rasmussen's and Hollomon's models, for the elastic, plastic (pre-necking) and post-necking behavior respectively. Each of these models is characterized by parameters, as indicated in Table 9.1.

The main mechanical properties of 5 milled transversal specimens are reports in Table 10.7, which correspond to those analyzed in section 5.2. "model T" is characterized by the corresponding mean values.

The parameters describing the stress-strain model are evaluated for each machined T specimen, and they are reported in Table 10.8, together with their mean values, descriptive of model T, their standard deviations and coefficients of variation.

The resulting stress-strain behavior is plotted in Figure 10.7, together with that of the milled specimens it was derived from, and the constitutive relationship of specimen 4D.

		specimens				
property	**unit**	**1 T**	**2 bis T**	**3 T**	**4 T**	**4 bis T**
Young's modulus E	MPa	116 700	116 450	109 640	112 270	111 990
0.01% proof stress $\sigma_{0.01\%}$	MPa	240,17	318,25	258,68	224,16	212,68
0.2% proof stress $\sigma_{0.2\%}$	MPa	367,22	362,14	372,49	358,66	329,65
ultimate stress σ_u	MPa	517,42	558,41	592,57	600,64	582,54
yielding strain ε_y	%	0,948	0,479	0,563	0,528	0,511
ultimate strain ε_u	%	18,51	30,05	22,63	21,44	25,77
strain at failure ε_f	%	21,11	33,18	25,94	22,12	28,56

Table 10.7 – Mechanical properties of milled T specimens

	Ramberg-Osgood	Rasmussen		Hollomon	
	n [-]	**E_y [MPa]**	**m [-]**	**n_1 [-]**	**K_1 [MPa]**
1 T	7,06	21 279	3,48	0,20	872
1 bis T	23,19	7 318	3,27	0,15	862
3 T	8,22	18 785	3,20	0,20	999
4 T	6,37	22 498	3,09	0,19	996
4 bis T	6,84	19 840	2,98	0,23	1 028
m	10,33	17 940	3,20	0,19	951
s	6,46	5 460	0,171	0,026	69,73
V	0,625	0,304	0,053	0,136	0,073

Table 10.8 – Parameters defining the averaged stress-strain model for T milled specimens

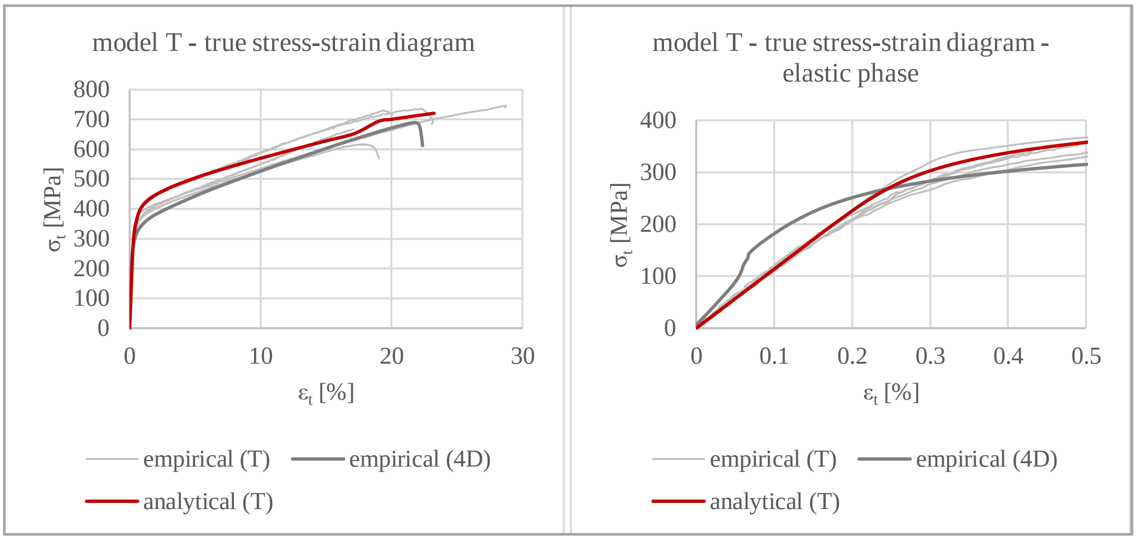

Figure 10.7 – Comparison between empirical and analytical true stress-strain curves of model T

10.3.2 Definition of the Finite Model in software Abaqus

Every characteristic concerning the model, but those referring to the definition of the behavior of the material, are not affected by the newly defined model; therefore, the geometry, the boundary conditions and the discretization defined in section 9.4.2 remain unvaried.

In Table 10.9 are reported the main input values set inside the software for the characterization of the material behavior for model T.

Figure 10.8 shows the plot corresponding to the input values for the plastic phase, in terms of true stresses vs true plastic strains, as well as that for model 4D (calibrated), which can be taken as a reference.

This graph displays a behavior for model T that is largely overestimating the target one, particularly in terms of yielding strength, namely $\sigma_{0.2\%}$.

phase	significant steps	input values			
		E [MPa]	**ν [-]**	**σ_t [MPa]**	**$\varepsilon_{t,pl}$ [-]**
elastic	-	113 410	0,33	-	-
plastic	0.01%	-	-	251,355	0
	0.2%	-	-	359,878	0,0020
	necking	-	-	693,655	0,1839
	failure	-	-	726,961	0,2509

Table 10.9 – Main input values in Abaqus for the characterization of material behavior – model T

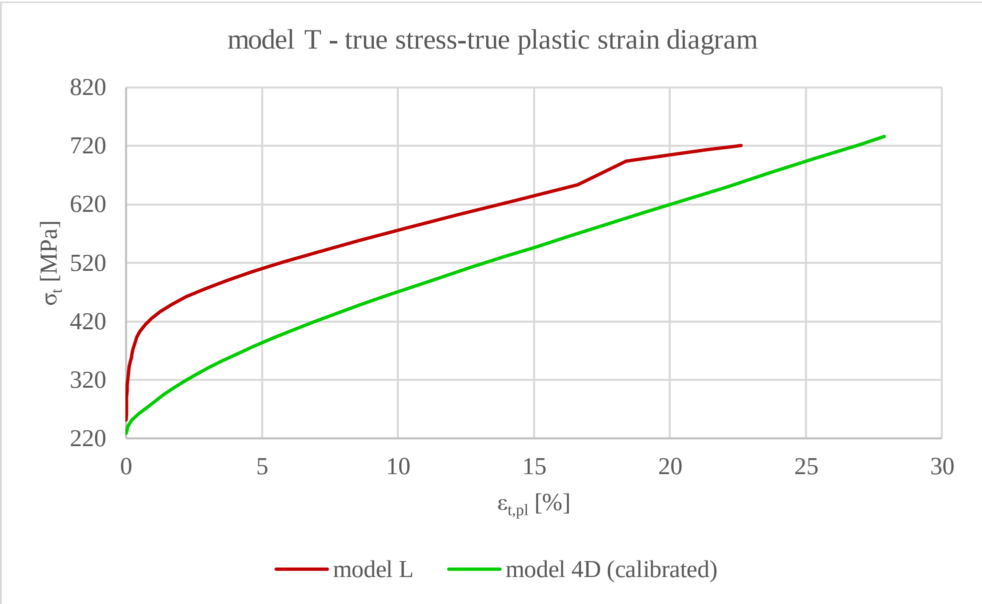

Figure 10.8 – True stress-true plastic strain curve – model T

10.3.3 Results of FEA

The considerations made, in section 10.3.2, about the plastic phase in terms of true stress-true plastic strain find association with the response in terms of reaction force vs displacement, as can be appreciated from Figure 10.9.

The assessment of the plastic behavior will only be qualitative in this study, while the elastic phase will be delved into more in depth in section 10.3.4.

In Figure 10.9 are also reported the F-u diagrams for specimen 4D and for a set of transversal rough specimens; as a first qualitative approximation, specimen 4D can be considered a fair representation of the average behavior of transversal rough specimens.

In Table 10.10, numerical results in terms of maximum reaction force, and related displacements, are reported, in comparison with the average behavior of rough specimens and that of specimen 4D, which is the reference one.

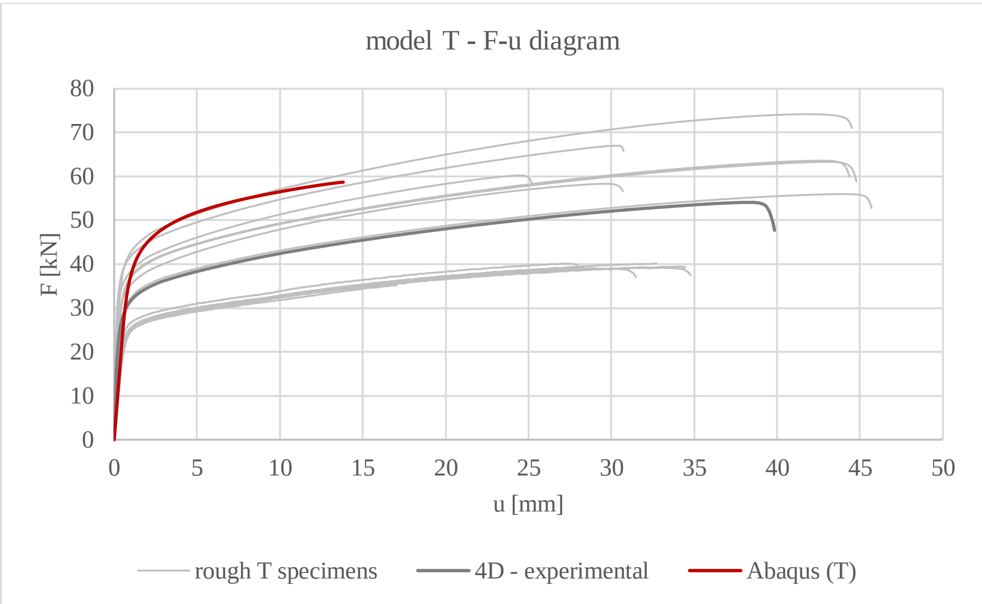

Figure 10.9 – F-u diagram – model T

	u_{max} [mm]	F_{max} [kN]
rough specimens (average)	34,07	50,47
4D - experimental	39,85	54,07
model T	13,82	58,66

Table 10.10 – Maximum values for F-u – model T

10.3.4 Analysis of the elastic phase

In Figure 10.10 is reported the F-u response in the elastic phase, for model L, reference solution 3A and a set of rough specimens, as well as a close-up on interval of displacements 0,05-0,25 mm for the evaluation of axial stiffness K.

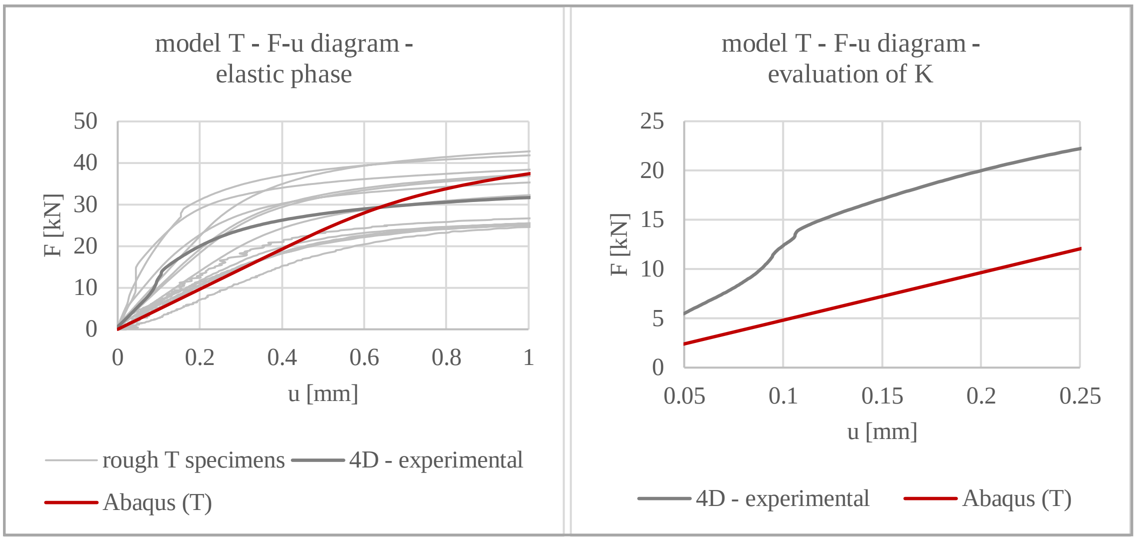

Figure 10.10 – F-u diagram: elastic phase – model T

It is evident that the reference axial stiffness is larger than the one obtained for model T, therefore it needs to be calibrated. In particular, recalling Table 9.19, K_{ref} = 88563,13 N/mm; the axial stiffness for model T assessed on average in the interval u = 0,010 to u = 0,218 mm, and its computation is reported in Table 10.12: K_T = 48122,99 N/mm.

	u [mm]	**F [kN]**	**K [N/mm]**
data	0,010000	0,4808	48084,80
	0,020000	0,9618	48091,40
	0,035000	1,6835	48100,57
	0,057500	2,7665	48113,74
	0,091250	4,3920	48131,51
	0,141875	6,8320	48154,93
	0,217813	10,495	48183,99
K_T			48122,99

Table 10.11 – Evaluation of axial stiffness K – model T

Computing the calibrating factor for the elastic phase according to expression (9.23), $\alpha_{E,T}$ = 1,840. New "model T-cal" is, therefore, defined by a new value of Young's modulus that is, exploiting (9.24), E_{cal} = 208 714 MPa. The corresponding true stress-strain diagram is plotted in Figure 10.11.

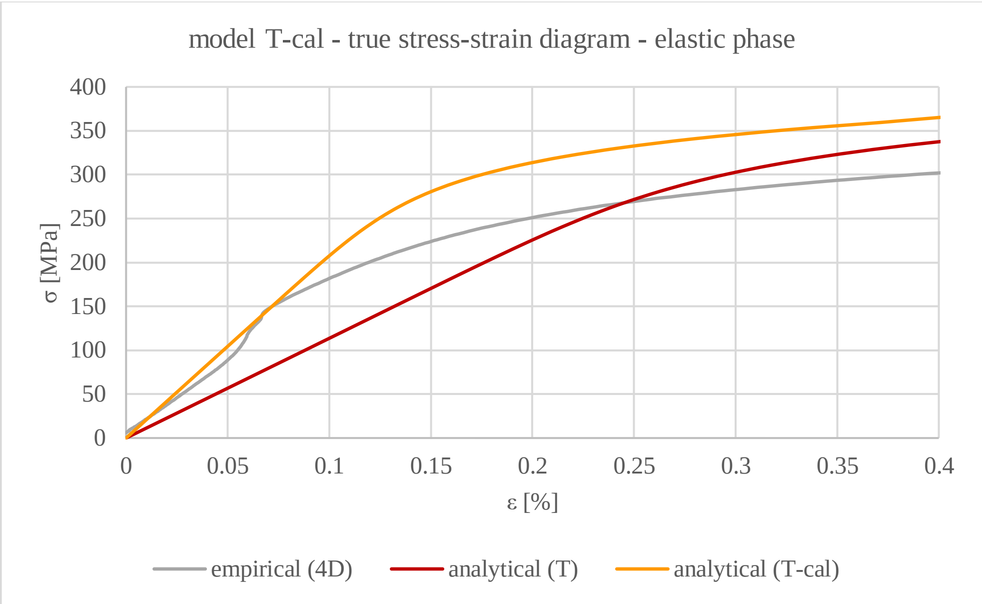

Figure 10.11 – σ-ε diagram: elastic phase – model T-cal

Model T-cal is developed in software Abaqus from the previous model (T), described in Table 10.9, only by modifying the value of E, as the plastic phase only very slightly varies due to E_y. The result of the simulation in terms of F-u response in the elastic phase is plotted in Figure 10.12, also accentuating the reference interval for the evaluation of axial stiffness K.

The validity of the calibrated model (T-cal) is, again, done by means of the reevaluation of axial stiffness K from the model, as reported in Table 10.12. The value obtained is $K_{T,cal}$ = 88524,63 N/mm; the ratio between K_{ref} and this value is $\alpha_{E,T\text{-}cal}$ = 1,000, therefore model T-cal can be considered a valid representation of the elastic behavior.

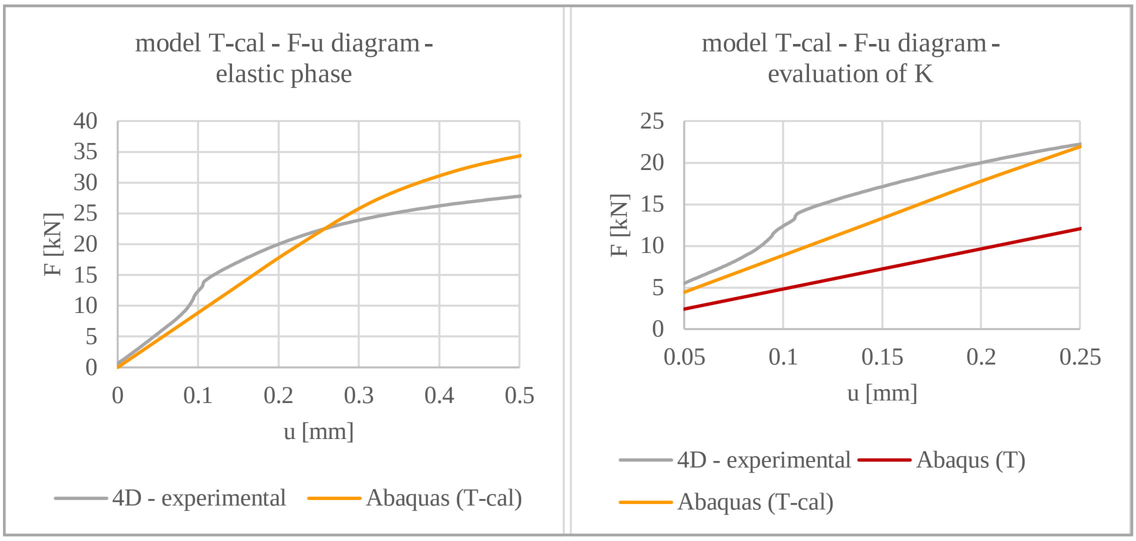

Figure 10.12 – F-u diagram: elastic phase – model T-cal

	u [mm]	**F [kN]**	**K [N/mm]**
data	0,010000	0,8849	88492,80
	0,020000	1,7701	88505,00
	0,035000	3,0983	88522,00
	0,057500	5,0914	88546,09
	0,091250	8,0828	88578,85
	0,141875	12,573	88617,44
	0,217813	19,257	88410,24
$K_{T,cal}$			88524,63

Table 10.12 – Evaluation of axial stiffness K – model T-cal

11. Application of stress-strain models from rough specimens to Digital Input Models

11.1 Overview

In Chapter 10, the stress-strain model was evaluated from milled specimens, hence not dependent on the irregular geometry, and applied to the Digital Twins of rough specimens.
Following the opposite approach, in this chapter, the stress-strain model is that obtained from the Digital Image Correlation analysis of the two reference rough specimens (3A and 4D), and it is applied to Digital Input Models (DIM), namely models whose geometry is regular (Figure 11.1).

According to this approach, the influence of the roughness is directly accounted for within the characterization of the material's behavior, while the geometry does not carry any irregularities; specifically, the thickness of each Digital Input Model will be equal to the effective one of the respective rough specimen.

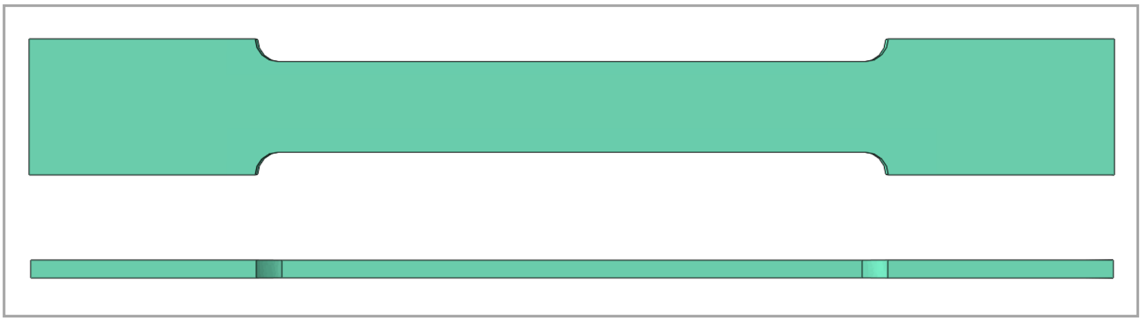

Figure 11.1 – xy and xz views of general Digital Input Model

11.2 Model 3A

11.2.1 Definition of the Finite Model in software Abaqus

Firstly, the geometry is defined as shown in Figure 11.1; specifically, the thickness of the model is set equal to the effective one of specimen 3A, namely t = 3,4 mm.
The behavior of the material corresponds to model 3A, whose parameters characterizing the model are reported in Table 9.3, and its main input values are listed in Table 9.4.

Since the geometry is significantly different than those analyzed up until now, the discretization and the application of boundary conditions must be redefined.
First, the approximate global size for seeds (nodes) is set at 2 mm. The type of element selected for this geometry is a C3D8, which is an 8-node linear brick element (Figure 11.2). This is a fair choice for such a simple geometry, especially because linear elements are related to a much lower computational cost than quadratic elements and are less sensitive to distortion.
The so-defined mesh is comprised of 5379 nodes and 3308 elements.

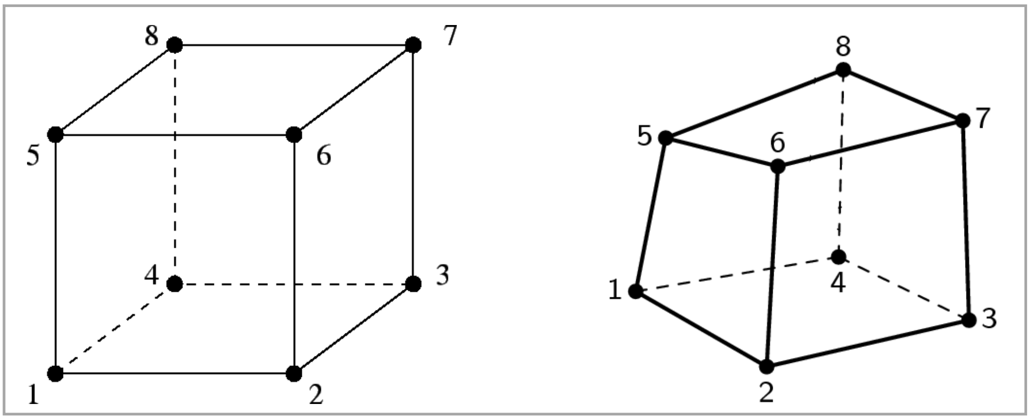

Figure 11.2 – C3D8 Finite Element – undeformed and deformed

For this regular geometry, there is not the need to define constraints, as the faces at each extremity as defined as a single feature. Therefore, as shown in Figure 11.3, the face at the left-end side is defined as an Encastre-type boundary condition at the initial step and propagated into the loading step, characterized by a Tabular Amplitude relating displacements and time as 1-to-1, while that at the right-end side is defined as a Displacement-type boundary condition, for which all displacement but that in direction x are fixed at the initial stage and set in the loading step according to the defined amplitude.

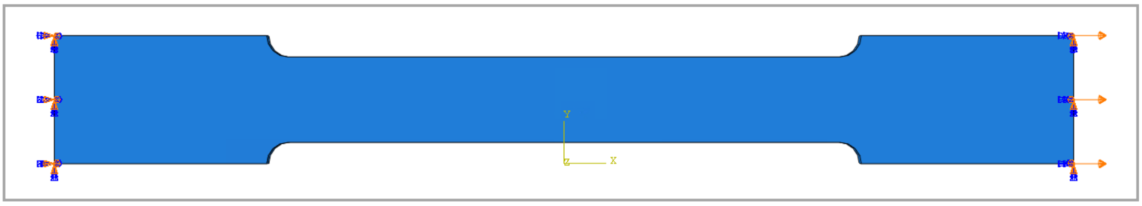

Figure 11.3 – Boundary conditions of model 3A-DIM – loading step

11.2.2 Results of FEA

The response in terms of reaction force vs displacement resulting from "model 3A-DIM" is plotted in Figure 11.4, in comparison with the response of specimen 3A as obtained experimentally.

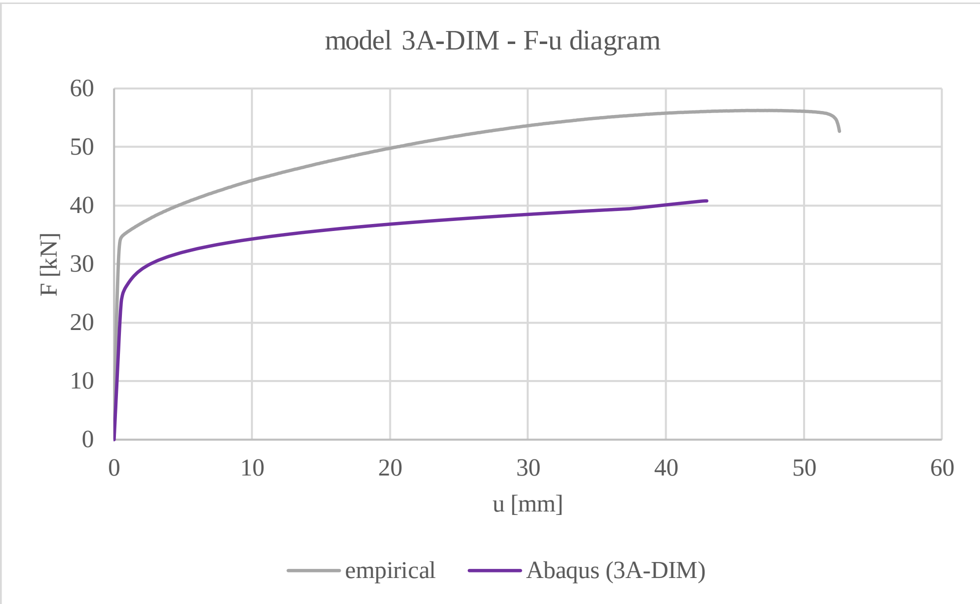

Figure 11.4 – F-u diagram – model 3A-DIM

It is very evident from this plot how the new model very poorly estimates the reaction force that the specimen actually develops, resulting in values of F in the plastic phase that are from about 10 to over 15 kN less than the reference ones, as reported in Table 11.1.

The analysis of this behavior is left to future studies, while the elastic phase will be investigated more in depth in section 11.2.3.

	u_{max} **[mm]**	F_{max} **[kN]**
experimental	52,58	56,25
model 3A-DIM	42,96	40,80

Table 11.1 – Maximum values for F-u – model 3A-DIM

11.2.3 Analysis of the elastic phase

Figure 11.5 reports the F-u response from model 3A-DIM, focusing on the elastic phase, compared to the reference one obtained experimentally for specimen 3A; it also offer a close-up on a chosen reference interval for the evaluation of axial stiffness K, namely from u = 0,05 mm till u = 0,25 mm.

It is clear that model 3A-DIM also largely underestimates the performance in the elastic phase.

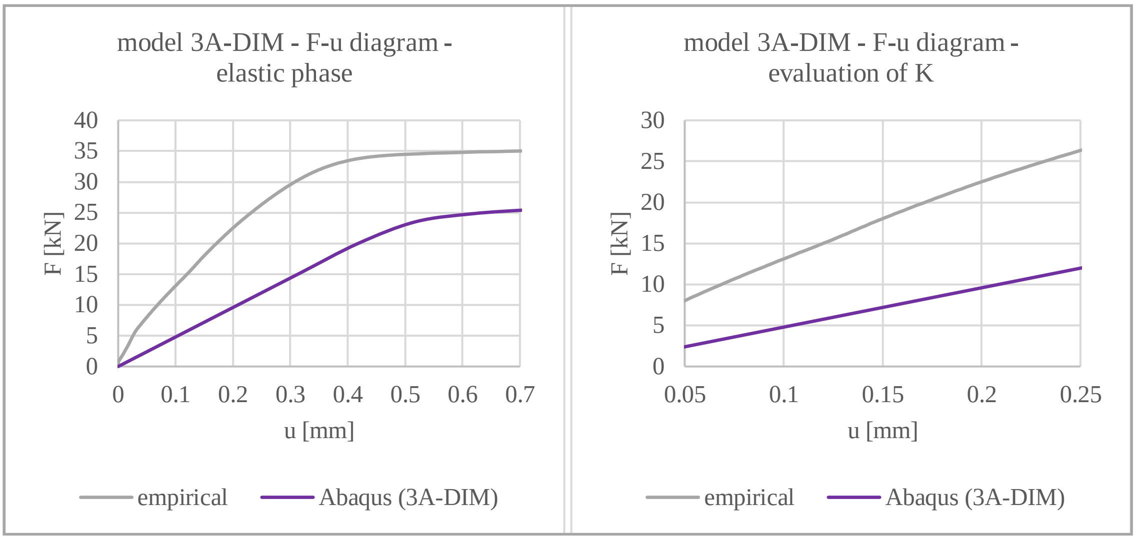

Figure 11.5 – F-u diagram: elastic phase – model 3A-DIM

Recalling Table 9.6, the estimated axial stiffness for specimen 3A from the experimental F-u plot is K_{ref} = 91530,35 N/mm. The axial stiffness characterizing model 3A-DIM is evaluated over a set of (u,F) values as the average of the resulting values of K, computed according to (10.1); the assessment is reported in Table 11.2.

The resulting value is $K_{3A\text{-}DIM}$ = 47973,23 N/mm; consequentially, $\alpha_{E,3A\text{-}DIM}$ = 1,908.

	u [mm]	F [kN]	K [N/mm]
data	0,010000	0,4799	47993,50
	0,020000	0,9598	47990,65
	0,035000	1,6795	47986,57
	0,057500	2,7589	47980,17
	0,091250	4,3773	47970,63
	0,141875	6,8038	47956,37
	0,217813	10,441	47934,70
$K_{3A\text{-}DIM}$			47973,23

Table 11.2 – Evaluation of axial stiffness K – model 3A-DIM

The elastic behavior of calibrated model "3A-DIM-cal" is, therefore, defined by Young's modulus E_{cal} = 278 892 MPa; the corresponding true stress-strain diagram is plotted in Figure 11.6.

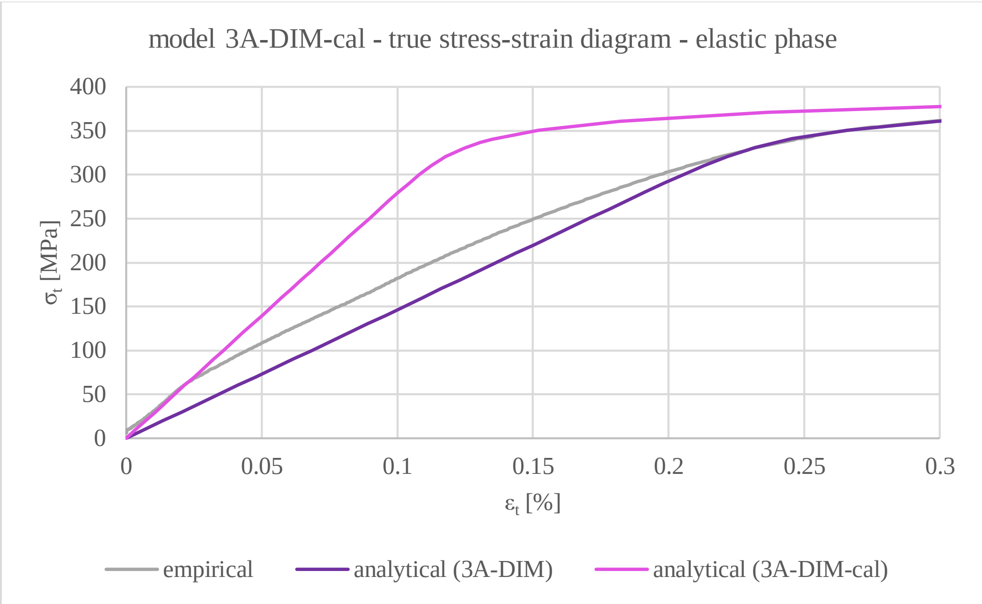

Figure 11.6 – σ-ε diagram: elastic phase – model 3A-DIM-cal

Figure 11.7 plots the elastic phase of the F-u response obtained running model 3A-DIM-cal. As reported in Table 11.3, the axial stiffness for this model is $K_{3A\text{-}DIM\text{-}cal}$ = 91542,45 N/mm; the ratio between K_{ref} and this value is $\alpha_{E,3A\text{-}DIM,cal}$ = 1,000, therefore model 3A-DIM-cal can be considered a valid representation of the elastic behavior.

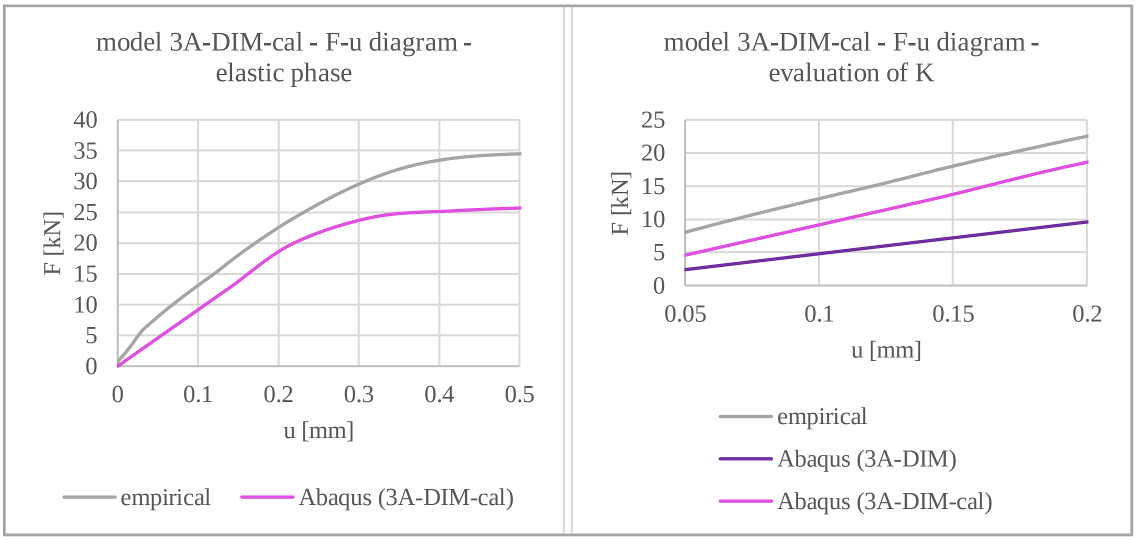

Figure 11.7 – F-u diagram: elastic phase – model 3A-DIM-cal

	u [mm]	F [kN]	K [N/mm]
data	0,010000	0,9157	91568,90
	0,020000	1,8313	91563,50
	0,035000	3,2044	91555,43
	0,057500	5,2638	91543,48
	0,091250	8,3517	91525,26
	0,141875	12,981	91498,15
$K_{3A\text{-}DIM,cal}$			91542,45

Table 11.3 – Evaluation of axial stiffness K – model 3A-DIM--cal

11.3 Model 4D

11.3.1 Definition of the Finite Model in software Abaqus

The geometry, as for the Digital Input Model for specimen 3A, is based off Figure 11.1, with a thickness of 4,29 mm, which is the value of the effective thickness of specimen 4D.
The material's behavior is that described by model 4D: the parameters defining the model are found in Table 9.16, while the main input values describing elastic and plastic phases are summarized in Table 9.17.

As for model the Digital Input Model of specimen 3A, model 4D-DIM is discretized setting an approximate global size for seeds of 2 mm and using C3D8-type elements. The resulting mesh includes 5343 nodes and 3284 elements.
Boundary conditions are defined as for model 3A-DIM, applied at the extreme faces, as more thoroughly described in section 11.2.1 and depicted in Figure 11.3.

11.3.2 Results of FEA

Figure 11.8 shows and compares the response of the specimen in terms of reaction force versus displacement, both that obtained model 4D-DIM as well as that acquired from the actual pull test performed on specimen 4D.

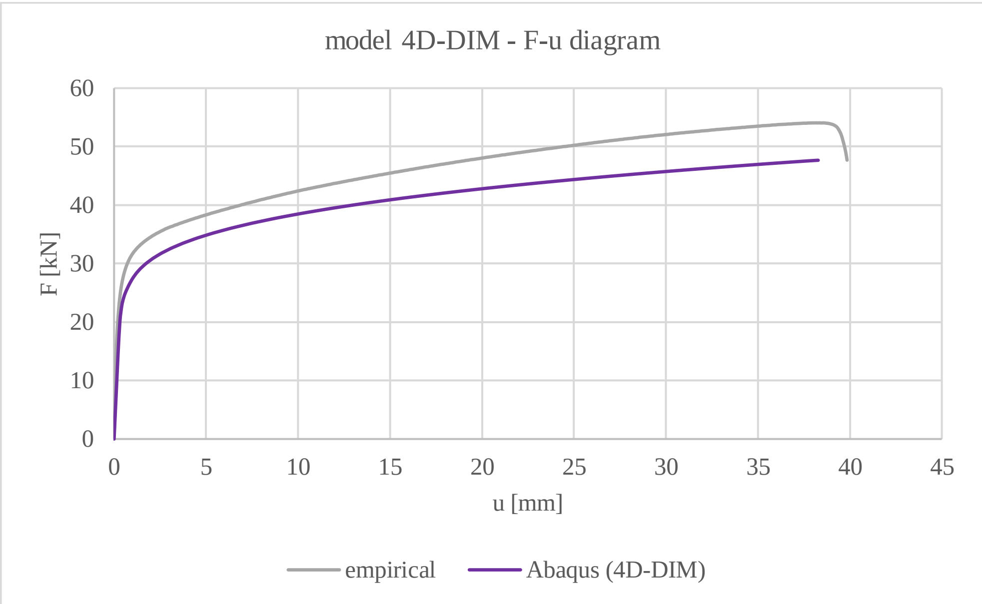

Figure 11.8 – F-u diagram – model 4D-DIM

From the plot, it is evident how the response in the plastic phase is underestimated of about 3 to 7 kN, while the level of ductility is fairly assessed, as can be seen more in detail in Table 11.4 As for model 3D-DIM, the study and evaluation of the plastic behavior is passed onto future studies on the matter, while section 11.3.3 hereafter will cover the elastic phase more in detail.

	u_{max} [mm]	**F_{max} [kN]**
experimental	39,85	54,07
model 4D-DIM	38,28	47,69

Table 11.4 – Maximum values for F-u – model 4D-DIM

11.3.3 Analysis of the elastic phase

Focusing on the elastic response obtained from the simulation of model 4D-DIM, Figure 11.9 shows the F-u plot up until u = 0,5 mm, while concentrating in the u = 0,05-0,25 mm interval for the evaluation of K.

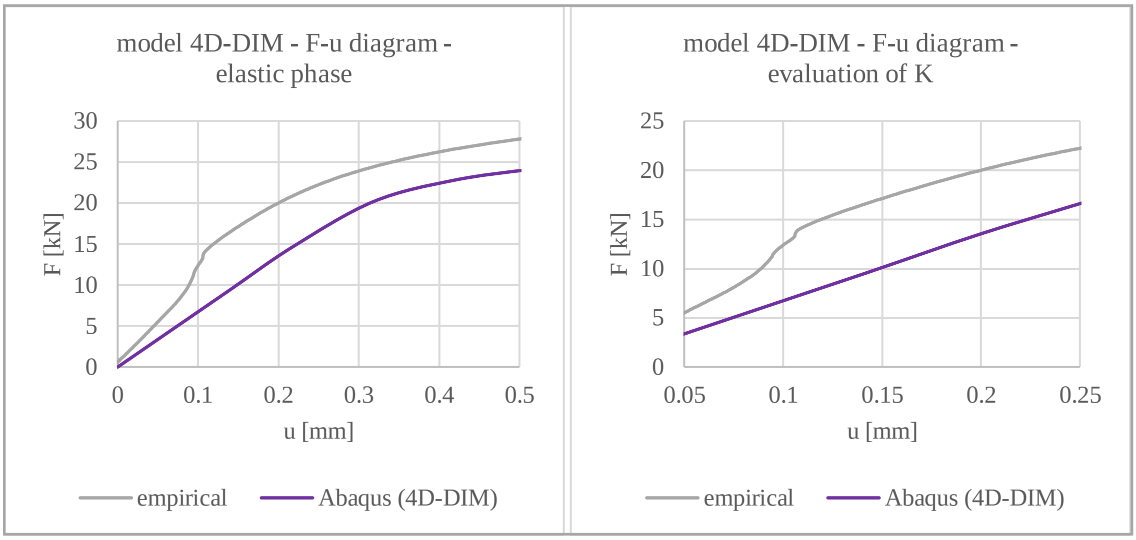

Figure 11.9 – F-u diagram: elastic phase – model 4D-DIM

The reference value for the axial stiffness is K_{ref} = 88563,13 N/mm, according to Table 9.19. The value of K for model 4D-DIM is evaluated in Table 11.5 and amounts to $K_{4D\text{-}DIM}$ = 67304,36 N/mm. This discrepancy can be translated in terms of input values in the model, namely Young's modulus E, which needs to be increased of a coefficient $\alpha_{E,4D\text{-}DIM}$ = 1,316, which corresponds to the ratio between the reference and 4D-DIM value of axial stiffness K.

	u [mm]	F [kN]	K [N/mm]
data	0,010000	0,6733	67329,40
	0,020000	1,3465	67326,00
	0,035000	2,3562	67321,14
	0,057500	3,8705	67313,74
	0,091250	6,1414	67302,58
	0,141875	9,5462	67285,92
	0,217813	14,648	67251,73
$K_{4D\text{-}DIM}$			67304,36

Table 11.5 – Evaluation of axial stiffness K – model 4D-DIM

A new model, named 4D-DIM-cal, can be introduced by setting the calibrated value of E as the input value for the definition of the elastic behavior of the material: said calibrated value, E_{cal}, is equal to 214 481 MPa. The new elastic model is plotted, in terms of stress-strain, in Figure 11.10. The input values defining the model in software Abaqus regarding the plastic phase remain almost unvaried and, while having been properly updated within the model, are not the focus of this analysis.

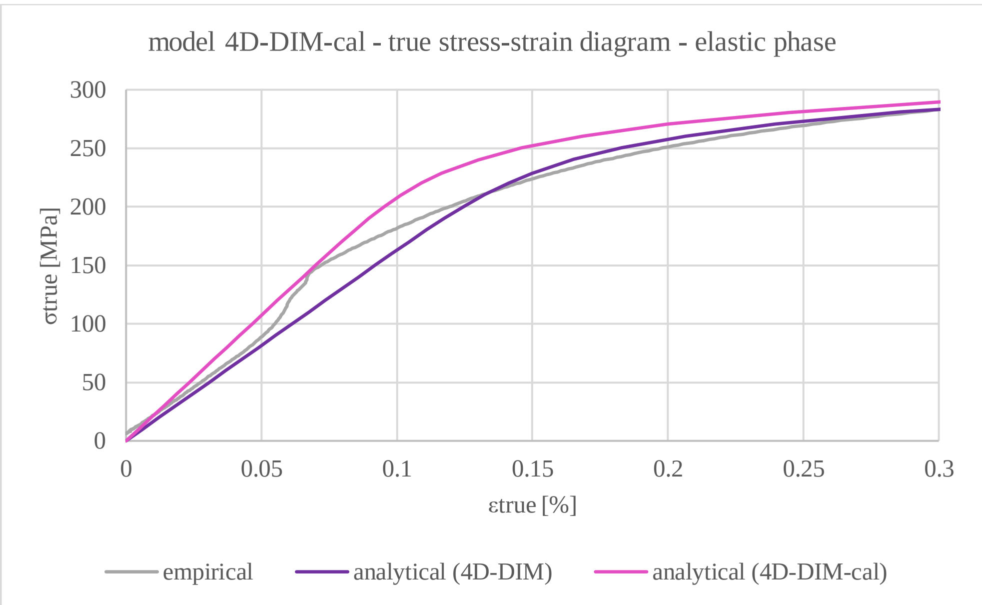

Figure 11.10 – σ-ε diagram: elastic phase – model 4d-DIM-cal

The resulting F-u diagram, up until a displacement of 0,5 mm, is plotted in Figure 11.11, partly focusing on the reference interval used for the estimation of axial stiffness K, reported in Table 11.6.

The assessed value of the axial stiffness for model 4D-DIM-cal is $K_{4D\text{-}DIM\text{-}cal}$ = 88574,54 N/mm; normalizing K_{ref} by this value, $\alpha_{E,4D\text{-}DIM,cal}$ = 1,000, therefore this model is a valid estimation of the elastic behavior.

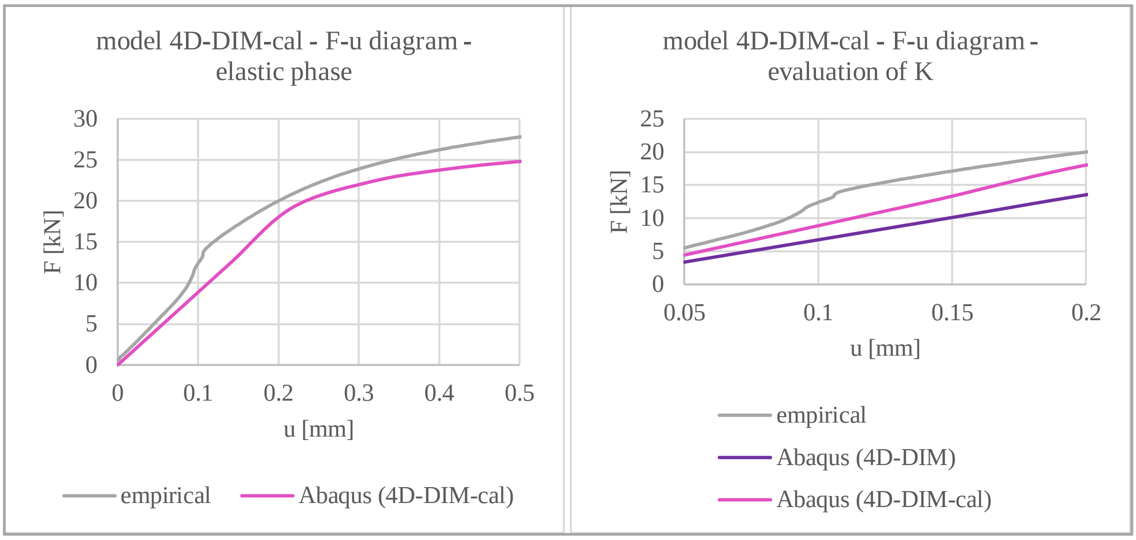

Figure 11.11 – F-u diagram: elastic phase – model 4D-DIM-cal

	u [mm]	**F [kN]**	**K [N/mm]**
data	0,010000	0,8860	88596,00
	0,020000	1,7718	88591,50
	0,035000	3,1005	88585,14
	0,057500	5,0931	88575,30
	0,091250	8,0812	88560,77
	0,141875	12,561	88538,50
$K_{3A\text{-}DIM,cal}$			88574,54

Table 11.6 – Evaluation of axial stiffness K – model 3A-DIM--cal

12. Part B – Conclusions

Part B of this study is focused on the analysis and evaluation of stress-strain models and on how geometrical irregularities influence the material's performance. This has been done for two rough specimens for which the Digital Twin was available, namely longitudinal specimen 3A and transversal specimen 4D.

Three different approaches have been followed:

- Materials WAAM-3A and WAAM-4D, defined by stress-strain models obtained from the effective constitutive behavior of the respective specimen, applied to the corresponding Digital Twin (DT); the roughness is accounted for both in the geometry and the material's behavior;
- Materials WAAM-L and WAAM-4D, defined combining stress-strain relationships from a set of milled specimens with the same orientation, applied to the respective Digital Twin; the influence of geometrical imperfections is only carried by the geometry;
- Materials WAAM-3A and WAAM-4D applied to Digital Input Models (DIM) characterized by the effective thickness of the corresponding specimen; the geometry is regular, hence the effects of the roughness are conveyed in the stress-strain models.

Figure 12.1 and Figure 12.2 offer an overview of the F-u responses from these three approaches compared to the empirical response, for specimen 3A and 4D respectively.

The main similarity found between the two graphs is an underestimation of the overall response when applying the rough stress-strain model to the Digital Input Model, more accentuated for longitudinal specimen 3A than for transversal one 4D.
On the other hand, for specimen 3A there is not much difference between the application of the milled stress-strain model and that of the rough one; this discrepancy is far more prominent for specimen 4D, and, in particular, they both largely overestimate the performance in terms of strength, while reaching very low values of displacement.

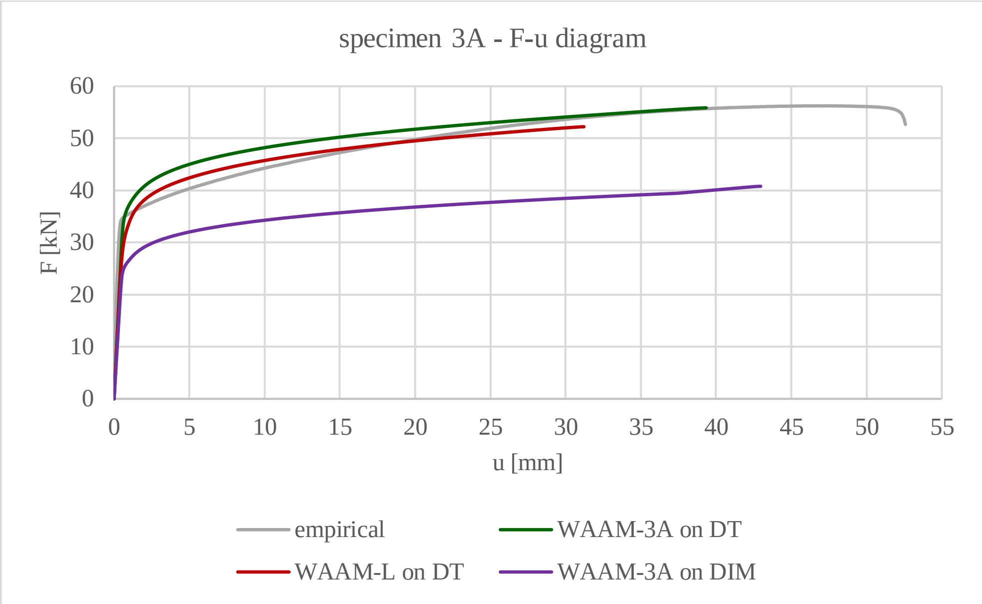

Figure 12.1 – F-u diagram – comparison of approaches for specimen 3A

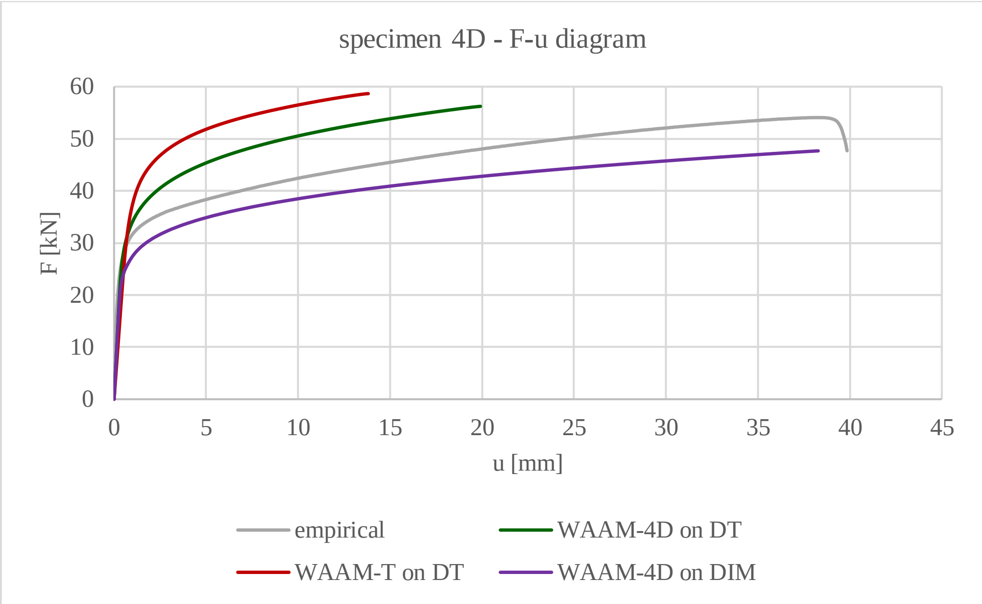

Figure 12.2 – F-u diagram – comparison of approaches for specimen 4D

Figure 12.3 and Figure 12.4 shift the focus on the elastic phase alone, which is the behavior analyzed more in depth in this study.

The most interesting outcome is that for all models, for both specimens, the axial stiffness is significantly underestimated with respect to the actual one evaluated experimentally.

In particular, for specimen 3A, the value of K from the models is about 52-64% the target value; for specimen 4D, while both models with material WAAM-4D are 76-78% the reference value, the axial stiffness from model L corresponds to only 54% of K_{ref}.

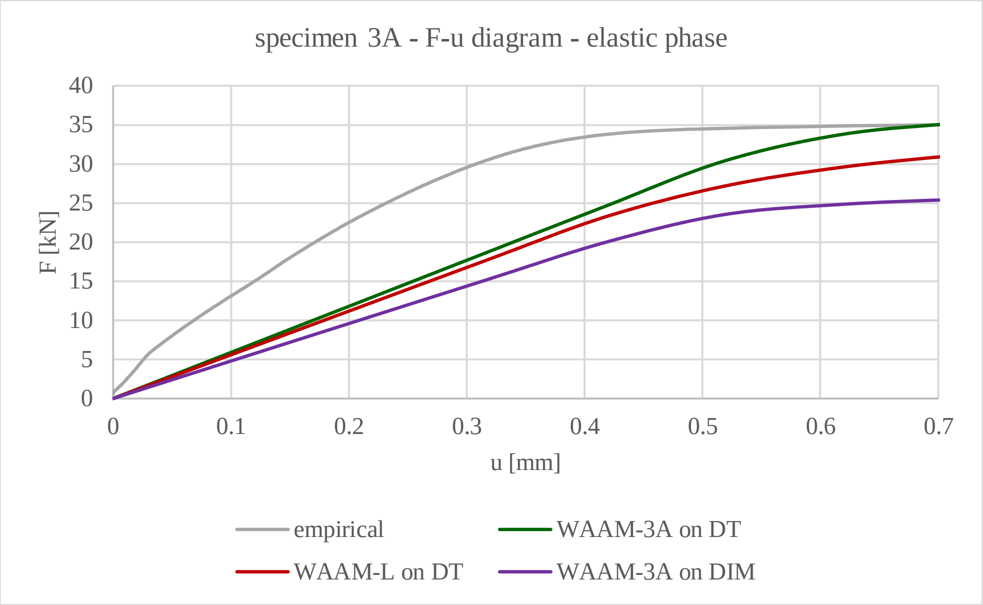

Figure 12.3 – F-u diagram: elastic phase – comparison of approaches for specimen 3A

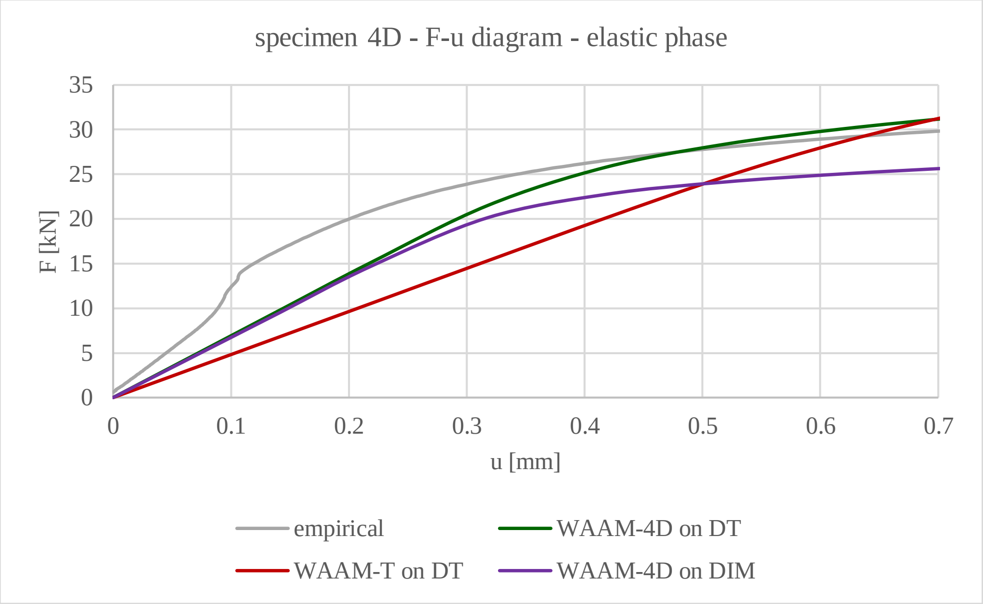

Figure 12.4 – F-u diagram: elastic phase – comparison of approaches for specimen 4D

13. Summary of work and findings

The study presented in this dissertation is focused on the analysis of the behavior of Wire-and-Arc Manufactured stainless-steel, form a design point-of-view, in order to offer some initial guidelines for the application of this material to the construction industry.
The main challenges related to this type of material are: its intrinsic geometrical imperfections, as the produced elements present a rough surface, due to the printing process itself, as well as its anisotropy, namely the dependency of mechanical properties on the relative orientation between the load application and the printing direction.

The report has been divided into two parts: Part A and Part B.

Part A focuses on a first, more general level of design, namely it revolves around the definition of characteristic values of geometrical and mechanical properties, and the calibration of existing partial safety factors, useful for a preliminary design.
These evaluations are done by means of the procedures outlined in Annex D of EN1990:2002, “Design assisted by testing”; it allows for the determination of design and characteristic values both of single properties and of the resistance function.
From the statistical interpretation of mechanical properties, as also underlined in previous studies developed on the matter, results underline that the transversal direction (loading applied orthogonally with respect to the printing direction) is characterized by the smallest values, both in terms of strains as well as stresses, while the diagonal direction (inclined of 45°) returns the best overall performance, even though longitudinal specimens (for which loading and printing directions are parallel) present a slightly higher ductility.
In the definition of the resistance function, a number of assumptions are made, in particular in order to focus all uncertainties on the geometrical irregularities. Thanks to this approach, partial safety factors can be directly related to the influence of the repeatability of roughness among a statistical population. Specifically, when the variability related to the geometrical features decreases, so does the value of the partial safety factor, as the design resistance reaches higher values.
For this reason, the main objective, in future studies as well as in the development of WAAM techniques within the construction industry, is for manufacturers to be able to guarantee a certain level of variability for the roughness and, consequentially, for researchers to link different levels of said scatteredness to specific values for the partial safety factors.

Part B aims at a deeper level of understanding of the material, in order to allow to carry out Finite Element Analyses on Digital Input Models that return realistic responses of the element and the material.
In detail, three different approaches are undertaken in order to understand the effects of geometrical imperfections on the material's behavior and performance.
The first approach involves the application of a model for the material assessed starting from the effective stress-strain relationship obtained from a rough specimen to the geometry of the rough specimen itself. This is the less accurate approach, as geometrical imperfections are accounted for both within the material's behavior and the geometry.
For this reason, the other two approaches either attribute said effects to the geometry or the material behavior. In particular, the second approach maintains the rough geometry, while the stress-strain model is assessed from a set of milled specimens; on the contrary, in the third approach, the rough material behavior is applied to a regular geometry, characterized by the effective dimensions of the respective rough specimen.
The outcomes of these analyses have been examined especially in terms of elastic behavior: for every approach, the resulting axial stiffness is far smaller than the actual one obtained from physical tests and, therefore, needs to be properly calibrated.
Regarding the plastic phase, there is not a general trend, but the fact that the milled material applied to the rough specimen returns a quite underestimated response. Any further evaluations on the overall response are left to future studies.

Bibliography

[1] European Committee for Standardization, EN 1990 - Eurocode 0: Basis of Structural Design, 2002.

[2] European Committee for Standardization, EN 1993-1-1 - Eurocode 3: Design of Steel Structures - Part 1-1: General Rules for Buildings, 2005.

[3] V. Laghi, M. Palermo, G. Gasperini, M. Veljkovic and T. Trombetti, "Assessment of design mechanical parameters and partial safety factors for Wire-and-Arc Additive Manufactured stainless steel," *Engineering Structures,* 2019.

[4] C. Buchanan and L. Gardner, "Metal 3D printing in construction: A review of methods, research, apllications, opportunities and challenges," *Engineering Structures,* 2019.

[5] P. Kyvelou, H. Slack, D. D. Mountanou, M. A. Wadee, T. B. Britton, C. Buchanan and L. Gardner, "Mechanical and microstructural testing of Wire-and-Arc Additively Manufactured sheet material," *Materials and Design,* 2020.

[6] V. Laghi, M. Palermo, L. Tonelli, G. Gasperini, L. Ceschini and T. Trombetti, "Tensile properties and microstructural features of 304L austenitic stainless steel produced by Wire-and-Arc Additive Manufacturing," *The International Journal of Advanced Manufacturing Technology,* 2020.

[7] "ramlab.com," [Online]. Available: https://www.ramlab.com/.

[8] H. Strauss and U. Knaack, "AM Envelope - Potentials of Additive Manufacturing for facade constructions," in *VI International Congress on Architectural Envelopes*, Donostia - San Sebastian, Spain, 2012.

[9] "mx3d.com," [Online]. Available: https://mx3d.com/.

[10] S. Pratheesh Kumar, S. Elangovan, R. Mohanraj and J. R. Ramakrishna, "Review on the evolution and tehnology of State-of-the-Art metal additive manufacturing processes," *Materials Today: Proceedings*, 2021.

[11] A. Hayward, F. Weare and A. C. Oakhill, Steel Detailers' Manual, 2011.

[12] K. V. Wong and A. Hernandez, "A review of additive manufacturing," *International Scholarly Research Network,* 2012.

[13] I. S. Kim, K. J. Son, Y. S. Yang and P. K. Yaragada, "Sensitivity analysis for process parameters in GMA welding processes using a factorialdesign method," *International Journal of Machine Tools and Manufacture,* 2003.

[14] V. Laghi, M. Palermo, G. Gasperini, V. A. Girelli and T. Trombetti, "On the influence of the geometrical irregularities in the response of Wire-and-Arc Additive Manufactured planar elements," *Journal of Constructional Steel Research,* 2020.

[15] V. Laghi, M. Palermo, G. Gasperini, V. A. Girelli and T. Trombetti, "Experimental results for structural design of Wire-and-Arc Additive Manufactured stainless steel members," *Journal of Constructional Steel Research,* 2019.

[16] H. Gulvanessian, J. A. Calgaro and M. Holicky, Designers' Guide to EN 1990 - Eurocode: Basis of Structural Design, 2002.

[17] T. Tankova, L. S. Da Silva, L. Marques, C. Rebelo and A. Taras, "Towards a standardized procedure for the safety assessment of stability design rules," *Journal of Constructional Steel Research,* 2014.

[18] ISO/TC 164/SC 1, "ISO 6892-1 - Metallic materials - Tensile testing - Part 1: Method of test at room temperature," 2009.

[19] European Committee for Standardization, EN 1993-1-4 - Eurocode 3: Design of Steel Structures - Part 1-4: General Rules - Supplementary rules for stainless steel, 2006.

[20] W. Ramberg and W. R. Osgood, "Description of stress-strain curves by three parameters," 1943.

[21] S. Tu, X. Ren, J. He and Z. Zhang, "Stress–strain curves of metallic materials and post-necking strain hardening characterization: A review," *Fatigue & Fracture of Engineering Materials and Structures,* 2019.

[22] W. F. Hosford and R. M. Caddell, Metal Forming - Mechanics and Metallurgy, 2011.

[23] ISO/TC 164/SC 2, "EN ISO 10275 - Metallic Materials - Sheet and strip - Determination of tensile strength hardening exponent," 2007.

[24] J. A. Schey, Instructor's solutions manual: to accompany introduction to manufacturing processes, 2000.

[25] D. Ding, Z. Pan, D. Cuiuri and H. Li, "Wire-feed additive manufacturing of metal components: technology, developments and future interests," *The International Journal of Advanced Manufacturing Technology,* 2015.

[26] European Committee for Standardization, EN 1993-1-8 - Eurocode 3: Design of Steel Structures - Part 1-8: Design of Joints, 2005.

[27] J. P. Jaspart and K. Weynand, Design of Joints in Steel and Composite Structures, 2016.

[28] L. Simoes da Silva, "Towards a consistent design approach for steel joints under generalized loads," *Journal of Construction Steel Research,* 2008.

[29] S. Navarro, "Validation of the Calculation Models and Design Tools for Steel Beam-Column Joints by Experiments and FEA," 2017.

[30] D. Roylance, "Finite Element Analysis," 2001.

[31] J. H. Hollomon, "Tensile Deformation," *Transactions of the Metallurgical Society of AIME,* 1945.

[32] V. A. Silvestru, I. Ariza, J. Vienne, L. Michel, A. M. Aguilar Sanchez, U. Angst, R. Rust, F. Gramazio, M. Kohler and A. Taras, "Performance under tensile loading of point-by-point wire and arc additively manufactured steel bars for structural components," *Materials & Design,* 2021.

[33] N. McCormick and J. Lord, "Digital Image Correlation," *Materials Today,* 2010.